

BROWNIAN DYNAMICS STUDY OF THE SELF-ASSEMBLY OF LIGATED GOLD
NANOPARTICLES AND OTHER COLLOIDAL SYSTEMS

by

SIDDIQUE J. KHAN

M.S., PIEAS, Islamabad, 2004

AN ABSTRACT OF A DISSERTATION

submitted in partial fulfillment of the
requirements for the degree

DOCTOR OF PHILOSOPHY

Department of Physics
College of Arts and Sciences

KANSAS STATE UNIVERSITY
Manhattan, Kansas
2012

Abstract

We carry out Brownian Dynamics Simulations to study the self-assembly of ligated gold nanoparticles for various ligand chain lengths. First, we develop a phenomenological model for an effective nanoparticle-nanoparticle pair potential by treating the ligands as flexible polymer chains. Besides van der Waals interactions, we incorporate both the free energy of mixing and elastic contributions from compression of the ligands in our effective pair potentials. The separation of the nanoparticles at the potential minimum compares well with experimental results of gold nanoparticle superlattice constants for various ligand lengths. Next, we use the calculated pair potentials as input to Brownian dynamics simulations for studying the formation of nanoparticle assembly in three dimensions. For dodecanethiol ligated nanoparticles in toluene, our model gives a relatively shallower well depth and the clusters formed after a temperature quench are compact in morphology. Simulation results for the kinetics of cluster growth in this case are compared with phase separations in binary mixtures. For decanethiol ligated nanoparticles, the model well depth is found to be deeper, and simulations show hybrid, fractal-like morphology for the clusters. Cluster morphology in this case shows a compact structure at short length scales and a fractal structure at large length scales. Growth kinetics for this deeper potential depth is compared with the diffusion-limited cluster-cluster aggregation (DLCA) model. We also did simulation studies of nanoparticle supercluster (NPSC) nucleation from a temperature quenched system. Induction periods are observed with times that yield a reasonable supercluster interfacial tension via classical nucleation theory (CNT). However, only the largest pre-nucleating clusters are dense and the cluster size can occasionally range greater than the critical size in the pre-nucleation regime until a cluster with low enough energy occurs, then nucleation ensues.

Late in the nucleation process the clusters display a crystalline structure that is a random mix of fcc and hcp lattices and indistinguishable from a randomized icosahedra structure.

Next, we present results from detailed three-dimensional Brownian dynamics simulations of the self-assembly process in quenched short-range attractive colloids. Clusters obtained in the simulations range from dense faceted crystals to fractal aggregates which show ramified morphology on large length scales but close-packed crystalline morphology on short length scales. For low volume fractions of the colloids, the morphology and crystal structure of a nucleating cluster are studied at various times after the quench. As the volume fraction of the colloids is increased, growth of clusters is controlled by cluster diffusion and cluster-cluster interactions. For shallower quenches and low volume fractions, clusters are compact and the growth-law exponent agrees well with BinderStauffer predictions and with recent experimental results. As the volume fraction is increased, clusters do not completely coalesce when they meet each other and the kinetics crosses over to diffusion-limited cluster-cluster aggregation (DLCA) limit. For deeper quenches, clusters are fractals even at low volume fractions and the growth kinetics asymptotically reaches the irreversible DLCA case.

BROWNIAN DYNAMICS STUDY OF THE SELF-ASSEMBLY
OF LIGATED GOLD NANOPARTICLES AND OTHER
COLLOIDAL SYSTEMS

by

SIDDIQUE J. KHAN

M.S., PIEAS, Islamabad, 2004

A DISSERTATION

submitted in partial fulfillment of the
requirements for the degree

DOCTOR OF PHILOSOPHY

Department of Physics
College of Arts and Sciences

KANSAS STATE UNIVERSITY
Manhattan, Kansas
2012

Approved by:

Major Professor
Amit Chakrabarti

Copyright

Siddique J. Khan

2012

Abstract

We carry out Brownian Dynamics Simulations to study the self-assembly of ligated gold nanoparticles for various ligand chain lengths. First, we develop a phenomenological model for an effective nanoparticle-nanoparticle pair potential by treating the ligands as flexible polymer chains. Besides van der Waals interactions, we incorporate both the free energy of mixing and elastic contributions from compression of the ligands in our effective pair potentials. The separation of the nanoparticles at the potential minimum compares well with experimental results of gold nanoparticle superlattice constants for various ligand lengths. Next, we use the calculated pair potentials as input to Brownian dynamics simulations for studying the formation of nanoparticle assembly in three dimensions. For dodecanethiol ligated nanoparticles in toluene, our model gives a relatively shallower well depth and the clusters formed after a temperature quench are compact in morphology. Simulation results for the kinetics of cluster growth in this case are compared with phase separations in binary mixtures. For decanethiol ligated nanoparticles, the model well depth is found to be deeper, and simulations show hybrid, fractal-like morphology for the clusters. Cluster morphology in this case shows a compact structure at short length scales and a fractal structure at large length scales. Growth kinetics for this deeper potential depth is compared with the diffusion-limited cluster-cluster aggregation (DLCA) model. We also did simulation studies of nanoparticle supercluster (NPSC) nucleation from a temperature quenched system. Induction periods are observed with times that yield a reasonable supercluster interfacial tension via classical nucleation theory (CNT). However, only the largest pre-nucleating clusters are dense and the cluster size can occasionally range greater than the critical size in the pre-nucleation regime until a cluster with low enough energy occurs, then nucleation ensues.

Late in the nucleation process the clusters display a crystalline structure that is a random mix of fcc and hcp lattices and indistinguishable from a randomized icosahedra structure.

Next, we present results from detailed three-dimensional Brownian dynamics simulations of the self-assembly process in quenched short-range attractive colloids. Clusters obtained in the simulations range from dense faceted crystals to fractal aggregates which show ramified morphology on large length scales but close-packed crystalline morphology on short length scales. For low volume fractions of the colloids, the morphology and crystal structure of a nucleating cluster are studied at various times after the quench. As the volume fraction of the colloids is increased, growth of clusters is controlled by cluster diffusion and cluster-cluster interactions. For shallower quenches and low volume fractions, clusters are compact and the growth-law exponent agrees well with BinderStauffer predictions and with recent experimental results. As the volume fraction is increased, clusters do not completely coalesce when they meet each other and the kinetics crosses over to diffusion-limited cluster-cluster aggregation (DLCA) limit. For deeper quenches, clusters are fractals even at low volume fractions and the growth kinetics asymptotically reaches the irreversible DLCA case.

Table of Contents

Table of Contents	viii
List of Figures	x
List of Tables	xii
Acknowledgements	xiii
Dedication	xiv
1 Introduction	1
2 Phenomenological Modeling of the Ligated Gold Nanoparticles	9
2.1 Components of the Effective NP-NP Interaction Potential	11
2.1.1 van der Waals Interaction between Two Gold Nanoparticles.	11
2.1.2 Free energy of mixing.	11
2.1.3 Elastic Contribution from Ligand Compression.	13
2.2 Evaluation of the Effective NP-NP Interaction Potential	13
2.3 NP-NP Interaction Based on Denting Conformation Model.	16
2.4 NP-NP Interaction Model Without Free Energy of Mixing.	18
2.5 Conclusion.	19
3 Brownian Dynamics Simulation Method	20
3.1 Brownian Motion	21
3.2 Verlet Algorithm For Molecular Dynamics	23
3.3 Brownian Dynamics Algorithm	24
3.4 Simulation Parameters	27
4 Self-Assembly of Dodecanethiol C_{12} and Decanethiol C_{10} Ligated Gold Nanoparticles from solution	29
4.1 Nucleation of the Nanoparticle Superclusters	30
4.1.1 Classical Nucleation Theory	31
4.2 Dynamical and Morphological analysis of Prenucleating SCs	38
4.2.1 Cluster Dynamics	38
4.2.2 Morphology and Shape of the Nucleating NPSCs	40
4.3 Induction Time Analysis using Fisher's Droplet Model	43
4.4 Aggregation at Higher Volume Fractions	46
4.4.1 Structure Factor	47

4.4.2	Growth Kinetics in C_{12} Ligated System	48
4.4.3	Growth Kinetics in C_{10} Ligated System	52
4.5	Conclusion.	57
5	Crystalline Structure of the nucleating cluster in Dodecanethiol Ligated Nanoparticles	58
5.1	Radial Distribution Function	59
5.2	Bond-orientational order Parameter	62
5.3	Crystalline Structure of Dodecanethiol and Decanethiol Ligated System NPSCs	63
5.3.1	Possibility of icosahedral (ich) structure	66
5.3.2	Evaluation of Crystalline Fraction	71
5.4	Conclusion.	74
6	Self-Assembly in a model of short-range attractive colloids	76
6.1	Interaction Model Potential and Simulation Parameters	79
6.2	Nucleation and Crystalline Structures for short-ranged shallow quenches . .	80
6.3	Symmetric Structures of Small Size Clusters and Their Distribution	88
6.4	Morphology and growth kinetics for shallow quenches	94
6.5	Morphology and growth kinetics for deep quenches	103
6.6	Conclusion.	105
7	Conclusions	107
	Bibliography	117
A	Free Energy of Mixing in the Interpenetration Regime	118
B	Free Energy of Mixing in Interpenetration and Compression Regime	121
C	Parameters of Brownian Dynamics Algorithm	123

List of Figures

2.1	Schematic drawing of the interpenetration of ligand layers from two different nanoparticles.	12
2.2	Schematic drawing of the interpenetration and compression of ligand layers from two different nanoparticles.	12
2.3	Total interaction potential with its various components between two dodecanethiol ligated gold nanoparticles.	15
2.4	Effective interaction potential between two gold nanoparticles with decanethiol, dodecanethiol, and hexadecanethiol ligands.	16
2.5	Effective interaction potential between two gold nanoparticles with using denting model.	17
2.6	Effective interaction potential between two gold nanoparticles without Free Energy of mixing.	19
4.1	Single Cluster Growth	31
4.2	Classical Nucleation Theory Plot	32
4.3	Variation of monomers plot	34
4.4	Variation in Coordination Number at different volume fractions	36
4.5	Supersaturation vs Induction Time	37
4.6	Dynamics of the biggest NPSC in C12 system	39
4.7	Distribution of change in size	40
4.8	Morphology of the biggest NPSC	41
4.9	structure of prenucleating NPSC	42
4.10	Pre vs Post Energy Comparison plot	43
4.11	Fisher's Droplet Model plot	45
4.12	Snapshots for C12 systems at $f = 0.005$ at $f = 0.02$	49
4.13	Rg variation with time for C12 system at $f = 0.005$	50
4.14	Rg variation with time for C12 system at $f = 0.02$	51
4.15	Structure Factor for C12 system at $f = 0.02$	52
4.16	Snapshot for C10 system	53
4.17	Structure Factor for the case of $C_{10}System$	54
4.18	Rg and Nc variation with time for $C_{10}System$	55
4.19	R_g and Nc variation with time for deeper $C_{10}System$	56
5.1	Radial Distribution plot	60
5.2	Neighbor Separation plot	61
5.3	Pure Crystalline Structure plot	65
5.4	random Crystalline Structure plot	66

5.5	random ich vs nucleating cluster plot	67
5.6	Ground state energy comparison of the nucleating NPSC	69
5.7	q4-q6 scatter plot for the nucleating NPSC in comparison with fcc, hcp and ich random structures	70
5.8	Snapshot of nucleating cluster in C12 system	73
5.9	Fractional composition of the crystalline structure as a function of time	74
6.1	Largest Cluster variations of the system for a $U_m = 4kT$ quench with $f = 0.002$ and $\zeta = 0.05$	82
6.2	Largest Cluster R_g and A_{13} variations of the system for $\zeta = 0.05$ and $\zeta = 0.3$	83
6.3	Energy comparison between prenucleating and nucleating clusters for $r_c =$ $1.05d$ and $r_c = 1.3d$	84
6.4	Degree of Crystallinity comparison between prenucleating and nucleating clusters for $r_c = 1.05d$ and $r_c = 1.3d$	85
6.5	Example of the comparison of the crystalline structures	86
6.6	Distribution of q_6 at $U_m = 4kT$ quench with $f = 0.002$ and $\zeta = 0.05$	88
6.7	Distribution of σ at $U_m = 4kT$ quench with $f = 0.002$ and $\zeta = 0.05$	90
6.8	Distribution of MOI at $U_m = 4kT$ quench with $f = 0.002$ and $\zeta = 0.05$	91
6.9	Distribution of W_6 at $U_m = 4kT$ quench with $f = 0.002$ and $\zeta = 0.05$	92
6.10	Distribution of W_6 at $U_m = 4kT$ quench with $f = 0.002$ and $\zeta = 0.05$	93
6.11	Snapshots of the system for a $U_m = 4kT$ quench with $f = 0.005$ and $\zeta = 0.1$	94
6.12	Structure factor of the system for a $U_m = 4kT$ quench with $f = 0.005$ and $\zeta = 0.03$	95
6.13	R_g variation with time for $\zeta = 0.03$ and $\zeta = 0.1$	96
6.14	Snapshot at 4kT for $f = 0.01$ and $f = 0.02$	99
6.15	Structure factor at 4kT for $f = 0.01$ and $f = 0.02$	100
6.16	Number of clusters at 4kT for $f = 0.01$ and $f = 0.02$	101
6.17	Radius of gyration at 4kT for $f = 0.01$ and $f = 0.02$	101
6.18	Snapshot at 10kT for $\zeta = 0.1$	103
6.19	R_g and N_c at 10kT for $\zeta = 0.1$	104

List of Tables

2.1	Parameters Used in the Calculations for Dodecanethiol Ligands in Toluene .	14
2.2	Hildebrand Solubility Parameters	14
4.1	Comparison of the critical size n' between CNT and Fisher Model	45
5.1	Bond Orientational Order Parameter values for different crystalline structures	64
5.2	A table of the random variations in the lattice sites at different shells in the hcp, bcc, fcc and ich crystal lattices	65
6.1	A comparison of our simulation clusters with maximum number of contacts for a given size ground state cluster with a short range interaction system and long-range interaction such as LJ system are also given.	89

Acknowledgments

During the course of five year education at K-state and during my prior formal education, I have been blessed with great teachers of inspiring personalities. I would like to take this opportunity to thank all of them in these years.

First of all, the person on top of my list to acknowledge is my advisor, Professor Amit Chakrabarti, for giving me opportunity to work with him, for providing a comfortable and friendly work environment, for being patient with me and my occasional slow progress, for understanding and cooperation in difficult times, for his encouragement and guidance and especially for giving me confidence to understand and solve problems independently during my progress towards the PhD.

I would also like to recognize useful discussions with Professor Chris. M. Sorensen during our occasional meetings. These meetings not only helped me to present my work in a better way but also his enthusiastic comments and remarks about my work always made me more excited and more involved in it. I would also like to acknowledge other members of the committee, Professor Bruce Law, Professor Kenneth J. Klabunde and Professor Liang-Wu Cai for their time and help. My list will remain incomplete without acknowledging Prof. Larry Weaver for having useful discussions.

I also owe a lot of thanks to all my family members, especially to my mother, and my friends, especially Abdul Hannan and Waqas M. Khan, for their love and prays. Last but not least, I would like to thank my wife Fatima for her love, care, encouragement, support and sacrifices during the work of this dissertation.

Dedication

Since his teachings and guidance have been a source of inspiration throughout my life, I dedicate this work to my father S. K. Jawaid.

Chapter 1

Introduction

Gold Nanoparticles (NP) are small spheres of gold colloid ranging in size from few nanometers to few hundred nanometers. Due to the large number of surface atom contributions, nanoparticles show different electronic, optical, and mechanical properties from those of their corresponding bulk materials and these properties are also effected by the size, shape and surface chemistry of the particles [1]. The optical properties of the nanoparticles depend upon the size of these particles. For example, the red color in stained glass windows is due to the colloidal gold nanoparticles, first prepared, comprehensively studied and published by Faraday in 1857 to account for the properties of these particles [2], and can be changed to violet or blue by changing the size of the particles [3]. The electronic properties of nanoparticles are also found to differ from those of their corresponding bulk form due to their small sizes [4]. Mie was the first person to give theoretical explanation for the color of the colloidal gold. According to this theory, based on the solution of Maxwell's equation, different colors appear due to the extinction (combination of absorption and scattering) spectra of the spherical particles [5]. Because of the size dependent properties, unique structures (i.e. monolayers and thin films) and their propensity to form 3-D superlattice structures, these nanoparticles have gained considerable attention in the recent literature [6]. Also, they have wide range of biological and medical applications. For example, nanocomposites composed of Au and biopolymer are employed as a novel biosensor. They can also be used for applications such as quantum dot displays, transistors, organic thin films, chemical and

pressure sensors, adhesion and friction modifiers, protective layers, and highly efficient catalysts with larger surface to volume ratio [7]. In medicine, gold nanoparticles can be used as drug carriers, tumor detectors and photothermal agents.

In some types, the surface of the nanoparticles are usually ligated with different kinds of organic compounds which help them to show stability against irreversible aggregation. These ligated gold nanoparticles, behaving as gold colloid solution, often show reversible temperature and solvent dependent solubility [8] and one of the challenges during the synthesis of these nanoparticles (NPs) is to prepare a monodisperse system of these colloids. Monodispersity of these particles not only helps us to study the properties of the individual building blocks present in the nanoparticle system but also these highly uniform particles can aggregate to form 2-D or 3-D superlattices. Lin *et al* [9] applied a digestive ripening technique to the polydisperse colloidal gold ligated with different thiols in toluene to achieve a monodisperse system of these particles. In such cases, when the particle size is highly uniform, these dispersed nanoparticles in the solutions can self-assemble to form aggregates of the nanoparticles. For example, Lin *et al* have synthesized nanocrystal superlattices (NCS) in a gold colloid solution through ligating the nanoparticle surface with dodecanethiol [10] and they have shown that by changing the temperature, one can control the superlattice formation. This reversible behavior shows a strong analogy with the molecular solutions and it is important to understand these variations in the behavior of the nanoparticle solutions.

In order to control the superlattice formation and to understand the stability of the NP colloidal dispersions, it is very important to have a detailed understanding of the interaction between the nanoparticles. For the case of non-aqueous solutions, in recent years, the NP colloidal systems are stabilized by using a variety of synthetic polymers and biopolymers and the mechanism is termed as the *steric stabilization*. As mentioned above, a protective surface coating or "capping" is used during the synthesis process to achieve a disperse state and this stabilization due to ligands or polymeric shells is becoming more and more common. A detailed theory or modeling of such systems is lacking in literature. Theoretical

modeling of NP-NP interactions can broadly be classified into two groups. In the first group, a coarse-grained approach is taken, and the interaction potential is often written in terms of effective van der Waals (vdW) interactions between the cores alone [11], [12]. Korgel *et al* considered ligated nanoparticles as "soft spheres" and estimated the steric repulsion between two nanoparticles by using the deGennes expression for two dense layers of strongly adsorbed chains in a good solvent [13]. This steric repulsion is compensated by the attractive vdW part of the overall inter particle interaction potential. In some work, the free energy of mixing between the tethered chains is also considered [14]. In the second group of theoretical modeling, a semi macroscopic approach is taken, and NP-NP interactions are calculated directly by numerical simulations [15], [16]. In such simulations, one typically considers two nanoparticles at a fixed distance in the presence of flexible chains that can adsorb onto the nanoparticles with some adsorption energy. The interaction between polymer segments is modeled by the Lennard-Jones potential, and the effective force between two nanoparticles is computed by using a virial relation. For the theoretical study of the interaction between the ligated NPs in solution, our approach is phenomenological. In addition to the vdW interactions between the nanoparticle cores, we treat the ligands as flexible polymer chains and do consider a free energy of mixing approach. Furthermore, we consider elastic contributions from compression of the ligands to the effective nanoparticle-nanoparticle pair potential.

Since the nanoparticle colloidal systems can be understood and manipulated as large, nearly stoichiometric molecular solutions, it is then reasonable to ask what is the nature of nucleation and growth [17], [18] of the insoluble phase? Does the classical nucleation theory (CNT) [19], [20], [21] apply to NP solution nucleation or is the pathway more complex? Does the two-step model proposed for protein crystallization [22], [23], [24] (where a stable cluster forms as a dense liquid as the first step and then the particles in the cluster reorganize into an ordered structure) apply to NPs? What is the shape of the fluctuating pre-nucleating SCs of NPs (we use the term supercluster to imply a cluster of nanoparticles, which are

often referred to as nanoclusters)? Are these spherical as assumed in classical nucleation theory or have other shapes as implied by recent colloid work [25], [26]? Such questions are not only of inherent intellectual interest but are also very useful, for with an understanding of this science, we will be able to control the self-assembly of NPs into either superlattices, ramified aggregates, gels or films on surfaces. Nucleation in nanomaterials is of particular interest since for these systems the "atoms" are nanoparticles (NPs) that are easily seen by table-top laboratory methods such as light scattering. By using our phenomenological model of the nanoparticle interaction, we studied the nucleation mechanism for the dodecanethiol ligated nanoparticle system in our simulation. Once the simulation system is quenched from a stable to a metastable regime, nucleation phenomena divide into two halves: those that happen before a critical nucleus occurs and those that happen after the critical nucleus forms. Before the critical nucleus forms, we desire to know the size, structure and number of pre-nucleation clusters that appear and disappear in the system. After the critical nucleus forms, we desire to know the kinetics of the ensuing cluster growth, number density and structure and compared our simulation results with the well known Classical Nucleation Theory (CNT) [27] and modified nucleation theory, known in literature as Fisher's Droplet Model [28].

According to our phenomenological model for the Np-Np interaction, the depth of the potential well is deeper for the case of decanethiol (C10) ligated system as compared to that of the dodecanethiol (C12) ligated system. The change in well depth not only change the critical size of the nucleating cluster but also affects the morphology of the aggregates. Due to the difference in depth of the potential well for the two cases, the morphology of the clusters is compact for the C12 ligated system. On the other hand, for the case of decanethiol ligated system, a hybrid morphology of the clusters is observed (i.e. compact structure at short length scale and more fractal-like structure at large length scale). Such hybrid morphology has been seen in both simulation and experiments. Range of interaction also plays an important role in the formation and structure of the colloidal aggregates and

hence on the phase diagram. If the range of interaction is larger than the size of the particles, the growth of the clusters resembles to those of the atomic clusters. On the other hand, for the case of short-ranged attractive systems, solid ordered phase starts to develop in the surrounding fluid phase [24] whereas for the intermediate range (i.e. comparable to the size of the particle), the solid phase coexists with the dilute and dense liquid phases. For the detailed analysis of the effects of range on assembly of the particles, we studied the nucleation and growth process in a simple colloidal model.

Even though the colloidal systems have long history and have been observed and used since the early civilizations, their scientific and systematic study has been developed recently. The quantities such as surface tension, electrostatic interactions, van der Waals interactions, steric interactions and other factors such as the presence of the polymers adsorbed at the surface of the colloids are generally responsible for the stability of the colloidal particles (By stability, we mean here that the particles have no tendency to aggregate) [29]. Different models have been proposed for different colloidal systems. For the case of colloidal dispersions in polar solvents or aqueous media, where electric charge is present on the surface of the particles (The evidence of the presence of these charges comes from the phenomenon known as *electrophoresis*), the stability is explained by a comprehensive theory known as Derjaguin-Landau-Verwey-Overbeck (DLVO) theory [30]. The theory describes a competition between the attractive van der Waals (vdW) forces and the electrostatic repulsive forces due to the surface charges. The van der Waals interactions are fairly independent of the electrostatic fixed charges and of electrolytic strength. Mainly, it depends upon the molecular density of the colloids. The electrostatic forces between the colloids originate either from the dissociation of surface groups (e.g. Carboxylic group $COOH \rightleftharpoons COO^- + H^+$) or due to the adsorption or binding in of ions from solution. The final charge is balanced by an equal and oppositely charged region of counter ions. Some of the counter ions are bound to the surface within the so-called '*Stern layer*' while the others form an *electric double layer* due to the thermal motion of the counter ions. According to Debye-Huckel Theory, the

electric double layer depends on the ionic strength I . As the ionic strength increases, the ionic double layer decreases rapidly. The effective length of the double layer is measured by a parameter known as *Debye Screening Length* k . The overlap of the double layers of two identical particles leads to the repulsion between the particles. Hence depending on the particle size, molarity of the salt and the surface potential, the DLVO potential can take various forms for details see ref. [29]. The electrostatic repulsive forces are very sensitive to the salt concentrations and if the double layer is larger than the particle radius, only one minima occurs in the overall potential curve and the particles coagulate irreversibly. Secondary minima starts appearing in the curve if the length of the double layer is comparable or smaller than the size of the particle and leads to the formation of reversible aggregates.

Another simplest possible interaction model for certain colloidal systems, composed of identical spheres, is known as the *hard-sphere interaction* model. Theoretically speaking, this model is based on the fact that a collection of identical particles, at lower packing fractions, are in a liquid state and as the packing fraction exceeds a certain value, a transition to an ordered solid phase takes place [31]. The only interaction between the particles, in this case, is the hard-sphere repulsion. For the case of protein solution systems, a short-range interaction model, introduced to study the protein crystallization [24], is used. This interaction model is a generalized extension to the Lennard-Jones potential.

In the case of non-adsorbing polymers added to the system in addition to the dispersed colloids in solution, an attractive force arise due to the osmotic pressure of these polymers. It is called the depletion interaction. The polymers added to the system are intermediate in size between the colloids and the size of the solvent molecules. These interactions are useful when rheological properties of the colloids are needed to control [32]. A decorative paint is a good example. Depletion interaction can also be used to cause the particles to phase separate. This interaction was first suggested by Asakura and Oosawa and later formulated by Vrij [33] based on the idea of a '*depletion layer*' close to the surface of a particle [34]. Within this layer, the concentration of the non-adsorbing polymers is less

than average leading to an osmotic pressure on the colloids from the surrounding polymers. The range of interaction is controlled by the size of the polymers whereas the interaction strength is controlled by the concentration of polymers. Using this model, one can easily change the strength and range of interaction and hence the effects of range and strength on the assembly of the colloids can be studied by using this model. We have studied nucleation mechanism and morphology of the aggregates using the AO model potential for different ranges. Furthermore, we studied the formation of small clusters in the bulk and the effect of their geometry on the nucleation process.

In this dissertation, our main focus will be to explore the Np-Np interactions in details and study the formation of nanoparticle assembly. Also, we will look at the morphology of these clusters by using Brownian Dynamics Simulations. In addition, we will look at the kinetics and morphology of cluster growth in the depletion model of short-range attractive colloids. The remaining chapters are outlined as follows.

In chapter 2, we present the phenomenological model to describe the interaction between two ligated gold nanoparticles in solution in details. The interaction potential is calculated for different ligands attached to the surface of the nanoparticles. Chapter 3 is devoted to the simulation technique used to study the assembly of these nanoparticles and other colloidal systems. Throughout this study, a *molecular dynamics algorithm* with a stochastic heat bath is used for the simulation purpose. We use the model potential described in chapter 2 and depletion interaction potential as input to our simulation. In Chapter 4, we will be focused on the theoretical study of the NP nucleation from their solution into a precipitated SC phase. Here, we will explore the nucleation process in our simulation and compare it with the Classical Nucleation Theory (CNT). Chapter 5 will focused on the identification of the crystalline structure of the nucleating clusters in details. Chapter 6 and 7 will be committed to study the morphology and growth of the aggregates by using the phenomenological model of the NPs interaction potential and depletion interaction potential respectively. In chapter 8, we use depletion model to study the factors responsible for the nucleation mechanism in

the short-ranged and long-ranged interaction of the colloids. Furthermore, we looked at the structure and distribution of small size clusters in the bulk.

Chapter 2

Phenomenological Modeling of the Ligated Gold Nanoparticles

In this chapter, our focus will be on the study of interaction between two monodisperse ligated gold nanoparticles required for their *self-assembly*. Generally, *self-assembly* has been defined as the impulsive organization of molecules/nanoparticles into well-defined three-dimensional geometry under a suitable circumstances [35]. In the case of ligated gold nanoparticle (NP) system, ligands are attached to the surface of the gold colloids. Theoretical modeling of NP-NP interactions can broadly be classified into two groups. In the first group, a coarse-grained approach is taken, and the interaction potential is often written in terms of effective van der Waals interactions between the cores alone [11], [12]. In some other works, the free energy of mixing between the tethered chains is also considered [14]. Such a coarse-grained approach to include the free energy of mixing ligands with solvent can be criticized for two reasons. First, the free energy of mixing is typically calculated for polymers end-grafted to flat surfaces and then converted to spherical particles via the Derjaguin approximation. However, the curvature effects of the nanoparticles are quite strong, and the Derjaguin approximation is expected to break down. Moreover, such a calculation typically considers the tethered chains as flexible polymer chains, which might not be a good approximation for the short alkane chains ligated onto nanoparticles.

In the second group of theoretical modeling, a semi macroscopic approach is taken, and

NP-NP interactions are calculated directly by numerical simulations [15], [16]. In such simulations, one typically considers two nanoparticles at a fixed distance in the presence of flexible chains that can adsorb onto the nanoparticles with some adsorption energy. The interaction between polymer segments is modeled by the Lennard-Jones potential, and the effective force between two nanoparticles is computed by using a virial relation. A recent study [16] finds that the effect of curvature of the nanoparticles is highly pronounced when the diameter of the nanoparticle (d) is about 5 times the bond length (σ) between the adjacent segments in a polymer chain. These types of calculations, however, are also limited by various factors. For example, the modeling of the ligand-ligand and ligand-nanoparticle interactions is phenomenological Lennard-Jones type. In addition, computational time limitations often restrict the choice of the size of the nanoparticles in such simulations. A typical gold nanoparticle has a diameter of about 5 nm whereas the carbon-carbon bond length in an alkane chain is about 0.15 nm. Thus, the ratio of the diameter of the nanoparticle (d) and the bond length (σ) between the adjacent segments in a ligand is about 33, which is much larger than the values (typically 5 or 10) used in simulations. In addition, these calculations are extremely time-consuming, and often a direct comparison to experimental results is not possible.

Our approach in this chapter is phenomenological. We treat the ligands as flexible polymer chains and do consider a free energy of mixing approach. In addition, we also consider elastic contributions from compression of the ligands to the effective nanoparticle-nanoparticle pair potential. As discussed earlier, this method has its limitations. However, such a calculation is important for various reasons. First, the separation of the nanoparticles at the potential minimum can be directly compared to experimental results of gold nanoparticle superlattice constants for various ligand lengths. Second, the calculated pair potentials can be used as input to Brownian dynamics simulations to study the formation of nanoparticle assembly. Finally, this type of phenomenological calculation can set a benchmark against which more accurate calculations can be compared.

2.1 Components of the Effective NP-NP Interaction Potential

In our phenomenological model, we consider a solution of gold nanoparticles of diameter $d=5$ nm ligated with various alkanethiol ligands in toluene. Ligands are considered to be flexible chains, and free energy of mixing and elastic contributions due to ligand compressions are considered in addition to van der Waals interactions.

2.1.1 van der Waals Interaction between Two Gold Nanoparticles.

The expression for the van der Waals interaction potential between two spherical particles was first derived by H.C. Hamaker [36] in 1937 in the pairwise summing approximation and can be written as

$$V_1(x) = -\frac{A}{12} \left[\frac{1}{x^2 - 1} + \frac{1}{x^2} + 2 \ln\left(1 - \frac{1}{x^2}\right) \right] ; x = r/d \quad (2.1)$$

Here, A is the Hamaker constant and x is the rescaled center-center distance between the two particles (i.e., $x = r/d$ where r is the bare center-center distance and d is the diameter of the gold core). In the presence of ligands on the nanoparticles, the effective Hamaker constant between two nanoparticles will have contributions from the bare gold-gold Hamaker constant, the ligand-ligand Hamaker constant (treated as a continuum layer), and the solvent-solvent Hamaker constants. However, the Hamaker constants of the solvent and the ligands are similar to each other and are much smaller than the Hamaker constant for gold. Thus, the effective Hamaker constant between two ligated nanoparticles can be estimated as the gold-gold Hamaker constant through the ligand medium and is taken as $A = 75.5kT$ in our calculations (with $T = 300$ K) as used in a previous study [37].

2.1.2 Free energy of mixing.

We estimate the free energy of mixing of the ligands when ligand layers from two different nanoparticles start overlapping. This estimate is based on the segment density distribution

function of the ligands as they start to overlap. Depending upon the value of the segment density distribution function, two different regimes of interaction are defined. In the first regime, which is called interpenetration regime, the segment density is defined by the length of the ligands (based on the fact that the ligands are fully extended when present in good solvents) . In the second regime, the chains undergo both interpenetration and compression and the segment density is defined by the separation between the nanoparticles [38]. These two regimes are shown schematically in figures 2.1 and 2.2, respectively.

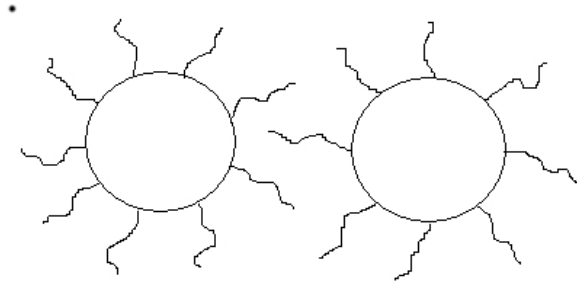


Figure 2.1: *Schematic drawing of the interpenetration of ligand layers from two different nanoparticles.*

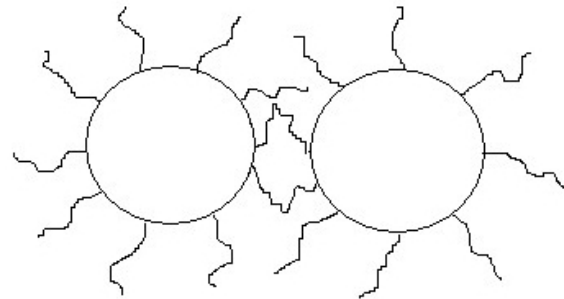


Figure 2.2: *Schematic drawing of the interpenetration and compression of ligand layers from two different nanoparticles.*

If the length of the ligands is denoted by L , then the regions of interactions in both regimes can be defined by the rescaled length of the ligands \tilde{L} where $\tilde{L} = L/d$. We calculate the free energy of mixing in our rescaled units (details given in appendix A) and its expression in regime I is given by;

$$\frac{V_2(x)}{kT} = \frac{\pi d^3 \phi_{av}^2}{2V_m} \left(\frac{1}{2} - \chi\right) \left[x - (1 + 2\tilde{L})\right]^2 ; 1 + \tilde{L} < x < 1 + 2\tilde{L} \quad (2.2)$$

where V_m is the volume of a solvent (toluene) molecule and ϕ_{av} is the average volume fraction of the ligand segments in the tethered layer, which are assumed to have a step profile with a uniform segment density in the layer and a sharp drop to zero segment density outside of the layer.

Similarly in regime II, the free energy of mixing can be written as

$$\frac{V_3(x)}{kT} = \frac{\pi d^3 \phi_{av}^2}{V_m} \left(\frac{1}{2} - \chi\right) \tilde{L}^2 \left[3 \ln\left(\frac{\tilde{L}}{x-1}\right) + 2\left(\frac{x-1}{\tilde{L}}\right) - \frac{3}{2}\right]^2 ; x < 1 + \tilde{L} \quad (2.3)$$

Note that when $x=1+\tilde{L}$, $V_2(x) = V_3(x)$, as expected.

2.1.3 Elastic Contribution from Ligand Compression.

The elastic contribution to the potential due to ligand compression is also known in the literature [39]. On close approach between two nanoparticles, the volume available for the tethered chains to fit is much less than when the two nanoparticles are infinitely separated. This gives rise to a loss of configurational entropy of the tethered chains and leads to an elastic repulsion between two nanoparticles. In terms of the rescaled variables used in this article, this can be written as (details given in appendix B)

$$\frac{V_4(x)}{kT} = \pi d^2 \nu \left[(x-1) \left(\ln\left(\frac{x-1}{\tilde{L}}\right) - 1 \right) + \tilde{L} \right] ; x < 1 + \tilde{L} \quad (2.4)$$

where ν is the number of ligands per unit area of the nanoparticle.

2.2 Evaluation of the Effective NP-NP Interaction Potential

We compute the effective pair potential between two nanoparticles in toluene with decanethiol, dodecanethiol, and hexadecanethiol ligands, respectively. The parameters used

Table 2.1: *Parameters Used in the Calculations for Dodecanethiol Ligands in Toluene*

parameters	values	references
diameter of gold nanoparticle (d)	5nm	
dodecanethiol ligated Hamaker constant	1.95eV or 75.5kT	[11]
size of the solvent molecule (toluene)	$V_m = 1.78 \times 10^{-28}(m^3)$	[40]
Flory χ parameter	$=(V_m/RT)(\delta_s - \delta_m)^2 + \beta_1$; where $\beta_1=0.34$ while δ_m and δ_s are the Hildebrand solubility parameters with the values listed in Table 2.2	[14]
surface area of gold covered by a thiol group $A_{thiol-gold}$	$21.5 A^2$	[41]

Table 2.2: *Hildebrand Solubility Parameters*

solubility parameters	δ values $\times 10^4 \sqrt{Pa}$	references
decane ($C_{10}H_{22}$)	1.58	[42]
dodecane ($C_{12}H_{26}$)	1.60	[42]
hexadecane ($C_{16}H_{34}$)	1.63	[42]
dodecanethiol ($C_{12}H_{26}S$)	1.65	[43]
decaneethiol ($C_{10}H_{22}S$)	1.74	[43]
hexadecanethiol ($C_{16}H_{34}S$)	1.69	[43]
toluene	1.82	[42]

in the calculations for dodecanethiol in toluene are listed [42], [43] in Tables 2.1 and 2.2. The parameters for the other two cases are similar [40], [44]. The value of ν , the number of ligands per unit area of the nanoparticle, is calculated from the estimated surface area of gold covered by a thiol group, [41] $A_{thiol,gold}$ as $\nu = 1/(21.5(10^{-10}m)^2) = 4.65 \times 10^{18}m^{-2}$, and the number of ligands per nanoparticle is $N \approx A_{surface,gold}/A_{thiol,gold} \approx 365$. Assuming that dodecanethiol has a molecular volume found from its molar weight and density of $\sim 3.98 \times 10^{-28}m^3$, we can find an estimate for ϕ_{av} . The ligand shell extends from $r = d/2(= 2.5nm)$ up to $r = d_0/2 + L(\sim 4.3nm)$. This shell has a volume of $V_{shell} \approx 2.68 \times 10^{-25}m^3$. Then

$$NV_{dodecane}/V_{shell} \approx 365(3.98 \times 10^{-28})/(2.68 \times 10^{-25}) \approx 0.54.$$

In the model calculation, we have assumed that the contributions to the free energy of mixing for ligand-ligand interpenetration originates only from the alkane-chain part of the ligands whereas the thiol group is firmly attached to the gold surface and does not play any role in this interaction. This is why we have used the solubility parameter values of unthiolated alkane chains (i.e., for $C_{10}H_{22}$) instead of those for thiolated chains ($C_{10}H_{22}S$) in Table 2.2. If we instead use the solubility parameters for the thiolated chains, the effective NP-NP potentials become too shallow and the NPs would not assemble as superlattices.

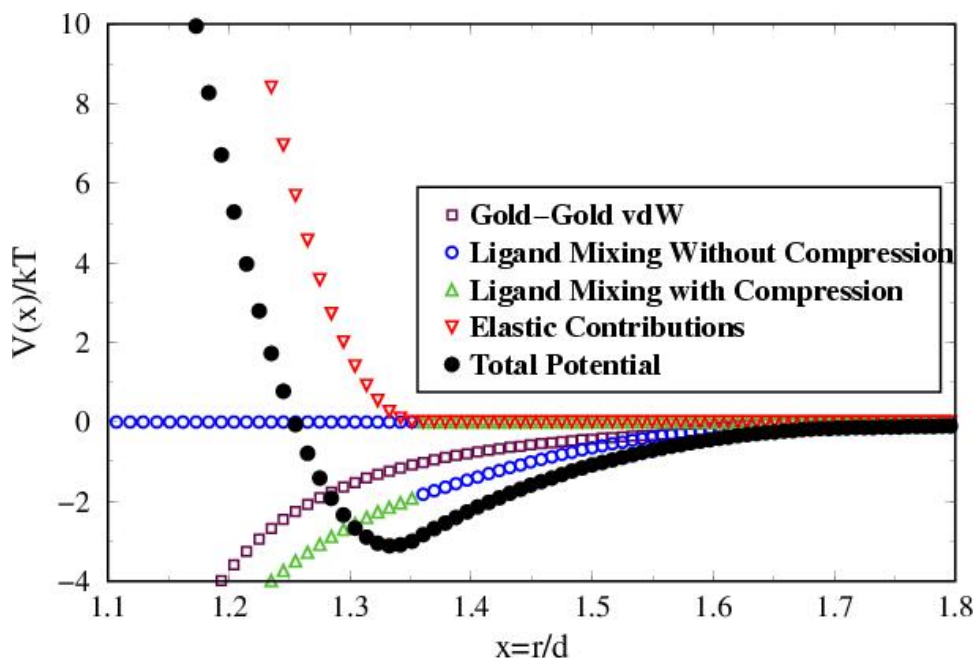


Figure 2.3: Total interaction potential with its various components between two dodecanethiol ligated gold nanoparticles.

The overall effective interaction potential between two nanoparticles is the combination of all the components mentioned in section 2.1. In Figure 2.3, we show various contributions to the effective potential for the dodecanethiol ligands. The location of the minimum of the potential compares extremely well to the superlattice constant calculated in experiments [45]. Next, we calculate the effective interaction potential for three different ligand

lengths. Figure 2.4 shows the total effective interaction potential for three different ligands.

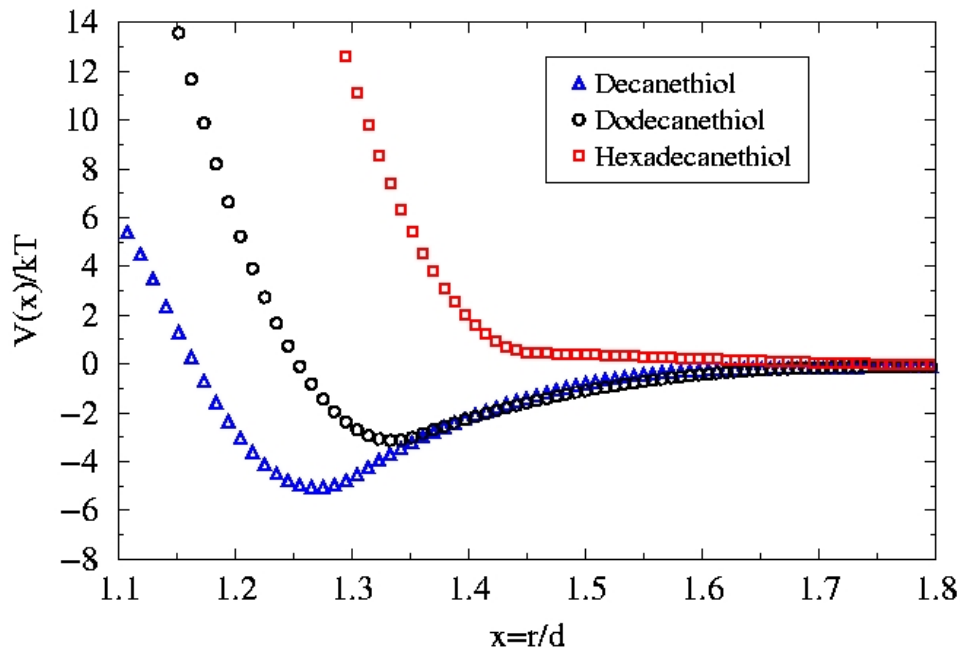


Figure 2.4: *Effective interaction potential between two gold nanoparticles with decanethiol, dodecanethiol, and hexadecanethiol ligands. The potential curves are effective potentials with contributions from van der Waals, ligand mixing with and without compression, and elastic compression terms.*

For dodecanethiol and hexadecanethiol, the location of the minimum of the effective pair potential agrees well with the superlattice constant seen in experiments. In addition, it is known experimentally that the solubility of gold NP in toluene improves with increasing ligand length. This is consistent with the trend seen in Figure 2.4 because the depth of the potential becomes shallower as the ligand length is increased.

2.3 NP-NP Interaction Based on Denting Conformation Model.

Considering the constant segment density function of the polymers, an alternative model was proposed by Baghei [38]. According to this model, instead of undergoing interpenetration

and compression mechanism, the polymer chains collapse during the interaction between two nanoparticles. This corresponding compression of chains is termed as "denting" mechanism. We have also considered this as possible situation and calculated the denting potential for our system. In the denting model, the ligand free energy of mixing potentials $V_2(x)$ and $V_3(x)$ is replaced by a denting potential given in our rescaled units as;

$$\frac{V_{dent}}{kT} = 4 \frac{\pi d^3 \phi_{av}^2}{V_m} \left(\frac{1}{2} - \chi \right) \tilde{L}^2 \left[3 \ln \left(\frac{2\tilde{L}}{x-1} \right) + \left(\frac{x-1}{2\tilde{L}} \right) - 1 \right]; 1 < x < 1 + 2\tilde{L} \quad (2.5)$$

Using the denting model, the interaction potential is calculated for decanethiol, dodecanethiol and hexadecanethiol ligated nanoparticles in toluene. Figure 2.5 shows the effective potential curves for the denting potential in comparison to our phenomenological model.

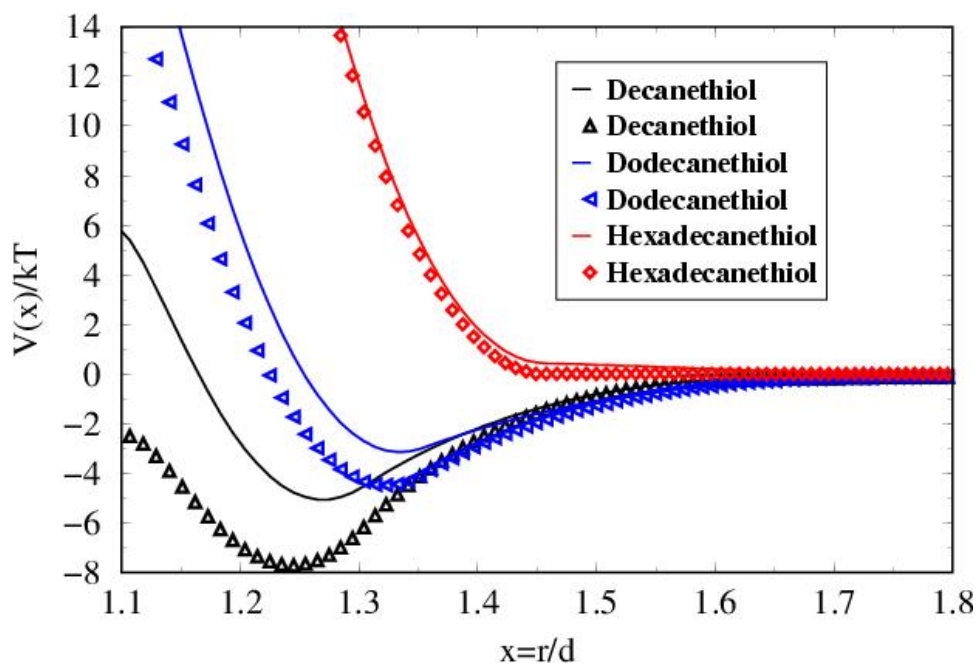


Figure 2.5: *Effective interaction potential between two gold nanoparticles with decanethiol, dodecanethiol, and hexadecanethiol ligands. The solid lines are effective potentials with contributions from van der Waals, ligand mixing with and without compression, and elastic compression terms. Symbols are for the effective potentials where the ligand mixing parts of the effective potential have been replaced by the denting potential. (See the text.).*

The symbols in the figure show the effective potential curves for the denting potential whereas the solid lines show the respective curves for our phenomenological model. From

figure 2.5 one observes that the potential wells are deeper for the denting potential for all of the ligand lengths considered in this study. The variation in the potential depth for hexadecanethiol and dodecanethiol ligands are not substantial. However, for the decanethiol ligands, the potential well becomes totally negative without any energy barrier to the primary van der Waals minimum. This is not a realistic description of the NP-NP interaction because decanethiol ligated gold nanoparticles do form superlattices [45]. We thus conclude that the denting potential is not a good alternative to the phenomenological model considered in section 2.2.

2.4 NP-NP Interaction Model Without Free Energy of Mixing.

Furthermore, we also studied the interaction between the nanoparticles based on the model where we have considered only the van der Waals interaction potential ($V_1(x)$) and the elastic contribution from ligand compression ($V_4(x)$) from section 2.1, neglecting contributions from the free energy of mixing of the ligands. The potential curves based on this model for the case of decanethiol, dodecanethiol and hexadecanethiol systems are shown in figure 2.6

From the figure 2.6, we can observe that even though there is a formation of potential minima, the quench depth for the respective systems is much shallower as compared to the case when we include the free energy of mixing to the overall interaction (sections 2.2 and 2.3). To test the validity of this model, we have carried out several simulation runs for different volume fractions ranging from 0.002 to 0.03 using this model but we have not observed any cluster formation even in the highest volume fraction case in any of the above mentioned systems. Although direct experimental studies of high monomer concentration in solution are not found in the literature, superlattices do form in nanoparticle solutions (on a TEM grid for example) where the solvent is allowed to evaporate, resulting in a dense system. The lack of cluster formation for any of the above mentioned ligand system indicates the lack of reliability of this model.

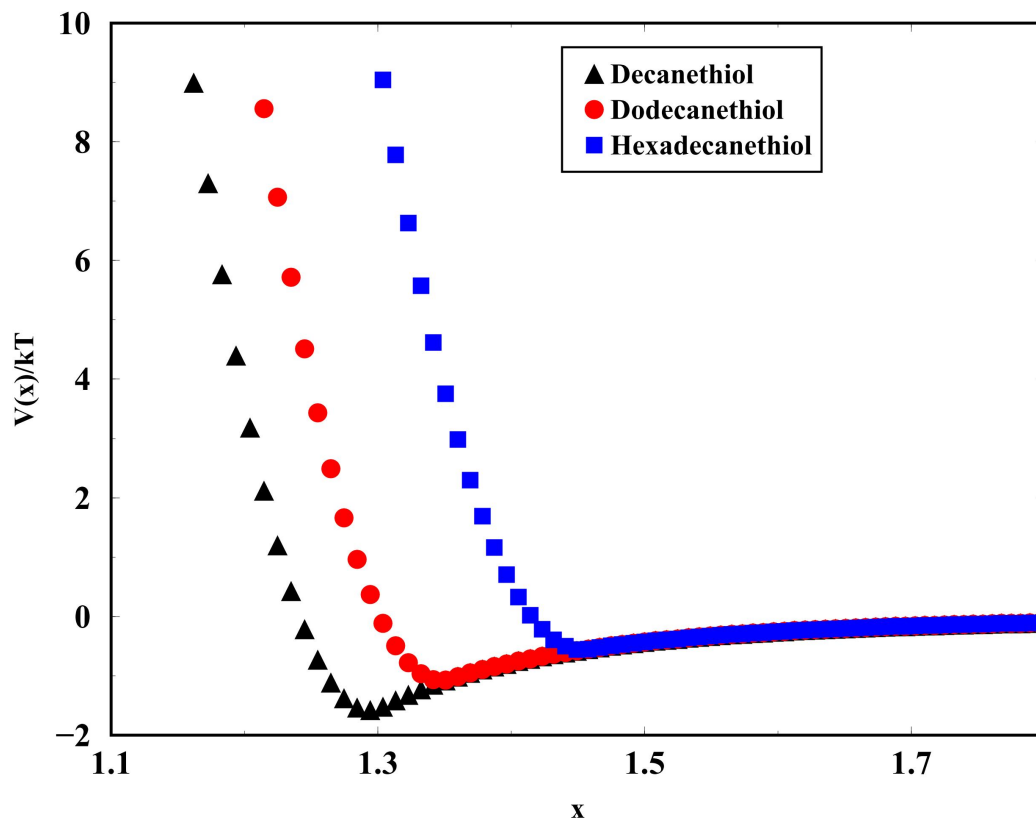


Figure 2.6: *Effective interaction potential between two gold nanoparticles without considering the free energy of mixing calculations for three different systems.*

2.5 Conclusion.

Based on our model calculations and analysis of experimental data, we conclude that just the van der Waals interaction among nanoparticles is not sufficient to describe NP-NP interactions and that the free energy of mixing term for the ligands plays an important role, particularly in dense systems. Furthermore, our phenomenological model which includes the interpenetration and compression of the ligands explains the experimental data better when compared to the denting model of ligand interaction.

Chapter 3

Brownian Dynamics Simulation Method

This chapter is devoted to the simulation technique we used to study the *self-assembly* of our nanoparticles/colloidal systems. The simulation of the molecular-scale to μm range particles can be divided into three major sections. First step is the construction of a model for the relevant problem then the calculations of molecular trajectories are performed in the second step while the third step is the analysis step where the calculated trajectories are analyzed to obtain the property values of the system particles. Depending upon the technique to calculate the particle positions, different molecular simulation methods can be distinguished. In the case of molecular dynamics method, different differential equations of motion are solved using numerical techniques to obtain the positions of the particles and all the positions are connected in time (i.e., the trajectories of the individual molecules can be extracted as in a motion picture). In the case of other most commonly used technique, known as the *Monte Carlo* Simulation Method, the molecular positions are not connected in time but are generated such that each new configuration of the particles stochastically depends only on their previous configurations. Such a process, in which the result of a random event in a sequence depends only on the outcome of the instantaneously previous event, is known as a Markov process. Apart from these two main branches of molecular simulations, there are other techniques in which the positions are computed by using a

hybrid method that involves some stochastic characteristics such as in Monte Carlo, and some deterministic properties, as in molecular dynamics. In this chapter, our focus will be on the continuum-dynamical method, known as Brownian Dynamics (BD) Method, which is based on the Langevin Equation [46] of motion. This method is an efficient way used for the study of many-particle systems, such as liquids, colloidal systems and macromolecules. For the case of solutions which are generally composed of larger colloidal particles and smaller solvent molecules such as the brownian particles, the motion of the colloidal particles are effected by the motion of the solvent molecules. As we have mentioned above that these effects can be described by a combination of the random forces and a frictional term in the equation of motion of the colloidal particles. In this method, some of the forces, such as effect of the solvent molecules on the solute particles, are not computed explicitly but are substituted by stochastic quantities as a replacement of the the fluctuating local environment experienced by the molecules.

3.1 Brownian Motion

Robert Brown was the first person to observe the *Brownian motion* in 1827 while studying the random motion of the pollen grains in a fluid. Theoretically speaking, first comprehensive theory of *Brownian motion* was proposed by Einstein in 1905 even though he was not conscious of the discovery of the phenomenon. According to Einstein's theory, the motion of such particles is diffusive in nature and the mean displacement of the particles is related to the diffusion coefficient D as;

$$\langle r^2 \rangle = 6Dt \tag{3.1}$$

where $\langle r^2 \rangle$ is the mean square displacement of an ensemble of the particles and D is the *diffusion coefficient*. The motion of colloidal particles in a fluid medium gives rise to a frictional (or drag) force, which is proportional to velocity, at least if the particles are

smooth and the velocity is not too great, such that the overall equation of motion of the particle is given by

$$M \frac{dv}{dt} = -\Gamma v \quad (3.2)$$

where Γ is the *frictional coefficient* and v is the velocity of the particle. Γ is inversely related to the *mobility* of the particles. The *frictional coefficient* can be related to *diffusion coefficient* by the relation

$$D\Gamma = kT \quad (3.3)$$

where $k_B T$ represents the approximate translational kinetic energy per particle, k_B being the Boltzmann constant. Here Γ for a spherical particle is given by Stokes law;

$$\Gamma = 6\pi\eta R \quad (3.4)$$

where R is the hydrodynamic radius of the particle (i.e. the effective radius presented by the particle to the liquid flowing locally around it) and η . The equation 3.3 is commonly known as the *Einstein relation*. It was later postulated by Langevin that, in the absence of any external force, the equation of motion of the particle is determined by the randomly varying instantaneous force acting upon it [46]. The motion resulting from this force is opposed by the resistance arising from the viscous force, which is proportional to the velocity of the particle. Hence the overall motion of a brownian particle is controlled by two important forces : one being the viscous drag force acting on the particles as they diffuse through the fluid and the second one being the rapidly fluctuating random force $F(t)$ acting on the particles (which average out to zero over long intervals of time) because of the collisions with the solvent molecules, such that we may write

$$M\dot{v} = -\Gamma v + F(t) ; \bar{F}(t) = 0 \quad (3.5)$$

So, the ensemble averaged equation is given by

$$M\langle \dot{v} \rangle = -\Gamma \langle v \rangle \quad (3.6)$$

Solving above equation, one gets

$$\langle v(t) \rangle = v(0) \exp(-t/\tau) \quad (3.7)$$

where τ is the *relaxation time*. Considering the limiting cases, it can be observed that in the limit when time $t \ll \tau$, the solution of the equation is comparable to the linear equation of motion as described by the Newton's second law (i.e. $r = vt$) whereas for the case when $t \gg \tau$, one can recover the Einstein's diffusion equation (i.e Eq. 3.1).

3.2 Verlet Algorithm For Molecular Dynamics

In 1967, Verlet introduced an algorithm, based on the finite-difference technique, to efficiently manage data in a molecular dynamics simulation using *neighbor-lists* [47]. Mathematically speaking, this simple method is a combination of two Taylor expansions, combined as follows. First write the Taylor series for position from time t forward to $t + \Delta t$:

$$x(t + \Delta t) = x(t) + \frac{dx(t)}{dt} \Delta t + \frac{1}{2} \frac{d^2x(t)}{dt^2} \Delta t^2 + \frac{1}{3!} \frac{d^3x(t)}{dt^3} \Delta t^3 + O(\Delta t^4) \quad (3.8)$$

Also, in the backward direction from t ,

$$x(t - \Delta t) = x(t) - \frac{dx(t)}{dt} \Delta t + \frac{1}{2} \frac{d^2x(t)}{dt^2} \Delta t^2 - \frac{1}{3!} \frac{d^3x(t)}{dt^3} \Delta t^3 + O(\Delta t^4) \quad (3.9)$$

Adding both eqs. 3.8 and 3.9 and eliminating the odd terms, the resultant equation is given by

$$x(t + \Delta t) = 2x(t) - x(t - \Delta t) + \frac{1}{2} \frac{d^2x(t)}{dt^2} \Delta t^2 + O(\Delta t^4) \quad (3.10)$$

This is the Verlet's algorithm for positions with a local truncated error of $(\Delta t)^4$ and hence has the accuracy up to third order, even though it does not contain any third-order derivatives. One important feature of this algorithm is that it is a two-step method because it estimates the next position $x(t + \Delta t)$ from the current position $x(t)$ and the previous position $x(t - \Delta t)$. It should be noted that the equation 3.10 for positions does not involve any function of the velocities while the acceleration in the equation is obtained from the intermolecular forces.

3.3 Brownian Dynamics Algorithm

In Brownian Dynamics, generally, the equation of motion of the particles (i.e solute particles) in a system is approximated by including the systematic force between the solute particles into the Langevin Equation:

$$m_i \dot{v}_i(t) = -m_i \Gamma_i v_i(t) + F_i(\{x(t)\}) + R_i(t) \quad (3.11)$$

where F_i is the explicit mutual force between the colloidal particles and is derived from the interparticle interaction potential $V(\{x(t)\})$ (see sections 2.1 and 6.1) between the colloids which depend on the coordinates of the particles and R_i is the random force due to the bombardment of the solvent molecules on the solute particles. Although the origin of both the forces is same, the random force R_i is assumed to be a stationary, *Markovian* and *gaussian* process with each random distribution has normalized with a mean zero:

$$\langle R_i(t) R_j(\hat{t}) \rangle = 2m \Gamma k_B T_{ref} \delta_{ij} \delta(t - \hat{t}), \quad (3.12)$$

where T_{ref} is the reference temperature and is given by $(3Nk_B)^{-1} \sum_{i=1}^{3N} m_i \langle v_i^2 \rangle$.

$$W(R_i) = [2\pi \langle R_i^2 \rangle]^{-1/2} \exp -R_i^2 / (2\langle R_i^2 \rangle), \text{ where } \langle R_i \rangle = 0 \quad (3.13)$$

where $W(R_i)$ is the gaussian probability of the stochastic force [48]. Also, the random force is assumed to have no correlation with prior velocities or the random force and the correlation in time is very short.

$$\langle v_i(t) R_j(\hat{t}) \rangle = 0, t - \hat{t} \geq 0 \quad (3.14)$$

$$\langle F_i(t) R_j(\hat{t}) \rangle = 0, t - \hat{t} \geq 0 \quad (3.15)$$

In the above mentioned equations, the notation $\langle \dots \rangle$ represents an average over an equilibrium ensemble and k_B is the *Boltzmann's* constant. The above mentioned assumptions for the random force $R_i(t)$ are reasonable for a Brownian particle because of the fact that

these particles have much larger mass than the colliding molecules and hence its motion is a result of large number of successive collisions. Also, the time between successive collisions is much shorter than the time scale of the Brownian motion. The velocity relaxation time is given by Γ^{-1} and if Δt is BD time step then in order to generate the stationary markovian gaussian process, the following condition must be satisfied

$$\Delta t \ll \Gamma^{-1} \quad (3.16)$$

Next, we follow the algorithm described by van Gunsteren and Berendsen [49] which is identical to the Verlet's algorithm mentioned in section 3.2. Solving equation 3.11, we get:

$$v(t) = v(t_n) \exp[-\Gamma(t - t_n)] + \exp[-\Gamma(t - t_n)] \frac{1}{m} \int_{t_n}^t \exp[\Gamma(\acute{t} - t_n)] \{F(\acute{t}) + R(\acute{t})\} d\acute{t} \quad (3.17)$$

where $v(t_n)$ is the velocity at the initial time $t = t_n$ and the indices of the particles and their cartesian components have been omitted. The integral over the systematic force $F_i(t)$ can be obtained by expanding $F\acute{t}$ in a power series upto 2nd order:

$$F\acute{t} = F(t_n) + \dot{F}(t_n)(\acute{t} - t_n) + O[(\acute{t} - t_n)^2] \quad (3.18)$$

Since, Verlet algorithm (section 3.2) is very accurate up to 3rd order in position, we only need to go up to first order inclusive in eq. 3.18. The derivative of the systematic force with respect to time at $t = t_n$ is denoted as $\dot{F}(t_n)$. The integration in 3.17 can be written as;

$$\begin{aligned} v(t_n + \Delta t) &= v(t_n) \exp[-\Gamma \Delta t] \\ &+ (m\Gamma)^{-1} F(t_n) [1 - \exp[-\Gamma \Delta t]] \\ &+ (m\Gamma^2)^{-1} \dot{F}(t_n) [\Gamma \Delta t - [1 - \exp[-\Gamma \Delta t]]] \\ &+ m^{-1} \exp[-\Gamma \Delta t] \int_{t_n}^{t_n + \Delta t} \exp[\Gamma(t - t_n)] R(t) dt \\ &+ O[(\Delta t)^3] \end{aligned} \quad (3.19)$$

Furthermore, to obtain the position of the particles, we integrate the velocity over a time

step $\Delta t = t_{n+1} - t_n$ by using the partial integration for the term involving $R(t)$,

$$\begin{aligned}
x(t_n + \Delta t) &= x(t_n) + \int_{t_n}^{t_n + \Delta t} \\
&= x(t_n) \\
&\quad + v(t_n)\Delta t(\Gamma\Delta t)^{-1}[1 - \exp[-\Gamma\Delta t]] \\
&\quad + (m)^{-1}F(t_n)(\Delta t)^2(\Gamma\Delta t)^{-2}[\Gamma\Delta t - [1 - \exp[-\Gamma\Delta t]]] \\
&\quad + (m)^{-1}\dot{F}(t_n)(\Delta t)^3(\Gamma\Delta t)^{-3}\left[\frac{1}{2}(\Gamma\Delta t)^2 - [\Gamma\Delta t - [1 - \exp[-\Gamma\Delta t]]]\right] \\
&\quad + (m\Gamma)^{-1} \int_{t_n}^{t_n + \Delta t} [1 - \exp[-\Gamma(t_n + \Delta t - t)]]R(t)dt \\
&\quad + O[(\Delta t)^4]
\end{aligned} \tag{3.20}$$

From equations 3.19 and 3.20, we define two random variables:

$$\mathcal{X}(\Delta t) \equiv m^{-1} \exp[-\Gamma\Delta t] \int_{t_n}^{t_n + \Delta t} \exp[\Gamma(t - t_n)]R(t)dt \tag{3.21}$$

and

$$\mathcal{Y}(\Delta t) \equiv (m\Gamma)^{-1} \int_{t_n}^{t_n + \Delta t} [1 - \exp[-\Gamma(t_n + \Delta t - t)]]R(t)dt \tag{3.22}$$

where $\mathcal{X}(\Delta t)$ and $\mathcal{Y}(\Delta t)$ have the same properties as those of $R(t)$. In the simulations, both $\mathcal{X}(\Delta t)$ and $\mathcal{Y}(\Delta t)$ are correlated as they are applied in the same time interval. So, they obey *bivariate gaussian distribution*:

$$W(\mathcal{X}(\Delta t), \mathcal{Y}(\Delta t)) = \frac{1}{\sqrt{4\pi^2\sigma_1^2\sigma_2^2(1 - r_{12}^2)}} \exp \left[-\frac{(\sigma_1\mathcal{X}(\Delta t) - \sigma_2\mathcal{Y}(\Delta t))^2}{2\sigma_1^2\sigma_2^2(1 - r_{12}^2)} \right] \tag{3.23}$$

The parameters σ_1 , σ_2 and r_{12} of this distribution can be determined by evaluating quantities $\langle \mathcal{X}^2(\Delta t) \rangle$, $\langle \mathcal{Y}^2(\Delta t) \rangle$ and $\langle \mathcal{X}(\Delta t)\mathcal{Y}(\Delta t) \rangle$ using the definition of $\mathcal{X}(\Delta t)$ and $\mathcal{Y}(\Delta t)$ mentioned in eqs. 3.21 and 3.22 and the correlation property mentioned in eq. 3.12. The detailed description of these parameters is given in Appendix C. Also, it can be seen in the Appendix C that for the limit, $\Gamma \rightarrow 0$, *Verlet Algorithm* can be retrieved.

3.4 Simulation Parameters

In our BD simulations, we consider three-dimensional systems and in most of the cases, the size of the box is $L = 128d$ in units of monomer diameter d . All other length scales are measured in units of d as well. Furthermore, we choose $\Gamma = 0.5$ and time step $\Delta t = 0.005$ in reduced time units of $d\sqrt{(m/kT)}$ with $m = 1$. In each time step, we are required to determine the interaction potential of the particles and their appropriate summation. Ideally, in order to calculate the force acting on a particle, one should calculate the interaction potential between all the particles in the system but since the potential (and corresponding forces) decays rapidly with the increase in the separation between the particles and interaction is restricted to *next-neighbors*, a certain threshold, beyond which all the interactions are neglected, is defined and forces are calculated up to that threshold. The threshold parameter is termed as cut off distance (r_{cut}) and it characterizes the range of the interaction potential. Hence, all the contributions to the forces on particle i that stem from particle j with $r_{ij} \gg r_{cut}$ are neglected. The value of r_{cut} is chosen large enough that the effects on the total energy of the system are negligible.

Next, we learn to find a way for the efficient description of the *neighbors* of a particle in the system. The technique we used for this purpose is termed as *Linked Cell Method* [50] in literature. The main concept of the *linked cell method* is to divide the physical simulation box of length L into uniform smaller boxes of equal sizes (called as cells *Lbox*) such that the length of the cell should be bigger than the potential cut-off value and the interactions are limited to the particles within the cell and the adjacent cells. Hence, the *neighbor* search is limited to the adjacent cells instead of searching in the whole simulation box and smaller the size of the cell is, faster are the force calculations. In order to keep track of the positions and to store all the dynamical variables of the particles in each cell, a *link list* [51] is generated. All the dynamical variables of each particle in the cell are stored in this *list*. In our simulation system, we have chosen the cell size to be $L_{box} = 4d$. In 3D, each cell in the interior of the box is attached to its 26 adjacent cells whereas the cells at the boundary

or edges of the box are linked to the adjacent cells by using *periodic boundary conditions* where the grid of the cells is extended periodically.

Chapter 4

Self-Assembly of Dodecanethiol C_{12} and Decanethiol C_{10} Ligated Gold Nanoparticles from solution

Nucleation of one phase of matter to another is of great and enduring interest. Applications range from materials processing, including both atomic and molecular based materials and the new nanomaterials, to particle formation in the atmosphere with consequences for the global environment. Nucleation in nanomaterials is of particular interest since for these systems the "atoms" are nanoparticles (NPs) that are easily seen by table-top laboratory methods such as light scattering. NP solution nucleation provides an experimentally accessible system that will reflect on the age-old problem of atomic and molecular system nucleation. Although a few experiments exist in the literature on NP nucleation, [52], [53], theoretical work is rare. Often colloids of surface ligated NPs act as solutions with the NPs displaying reversible temperature and solvent dependent solubility [8], [54], [55], [56]. and nucleation phenomenon [57], [58]. These NPs, also called nanoclusters of atoms, often have non-bulk properties due to finite size effects and/or a large fraction of surface matter. The novel, size-dependent properties combined with the uniformity suggest that NPs can be understood and manipulated as large, nearly stoichiometric molecules. Because of this, NPs and their assemblies have great promise as a basis for a wide variety of new materials with unprecedented properties and hence have seen considerable attention in the recent litera-

ture. Nanoparticles are usually surface ligated with any of a variety of organic compounds and these ligands cause colloids of the NPs to be stable against irreversible aggregation. In many cases when the NPs are highly uniform, the precipitating solid is a two- or three-dimensional superlattice of the NPs [59], [60] [9]. This behavior shows a strong similarity to the molecular solutions and such analogies make one more intriguing about the factors involved in the phase behavior of these NPs [17], [18]? How nucleation and crystal growth take place in NP solution and can one apply classical nucleation theory (CNT) [19], [20], [21] to NP solution or the pathway is more complex? Does the crystallization mechanism match with the protein systems where it behaves as two-step process [22], [23], [24]? How the pre-nucleating superclusters dynamically evolve into a stable structure? Are these spherical as assumed in classical nucleation theory or have other shapes as implied by recent colloid work [25], [26]? Such interesting questions are useful to control the self-assembly of these NPs. Before the critical nucleus forms, we desire to know the size, structure and number of pre-nucleation nanoparticle superclusters (NPSCs) that appear and disappear in the system. After the critical nucleus forms, we desire to know the kinetics of the ensuing cluster growth, number density and structure. In this chapter, we present a comprehensive theoretical study of shape and growth kinetics of NPSCs in the pre-nucleation and nucleation regimes. We will use our phenomenological model [61] for the effective interaction potential between two ligated gold nanoparticles. The computed NP-NP effective pair potential is used here in a Brownian Dynamics simulation for studying kinetics of nucleation and growth and the morphology of the SCs.

4.1 Nucleation of the Nanoparticle Superclusters

Nucleation is a stochastic process which takes place due to the formation of a nucleus of new phase (solid phase in our case) in an old phase (gas phase in our case). In this chapter, we study the nucleation process in the dodecanethiol ligated nanoparticle system described in chapter 2. For that matter, we tune our system volume fraction f in a way that the

transition from a disperse phase to the solid phase may lead to the formation of one or few isolated SCs in the system. An example of a single cluster growing in the system is shown in figure 4.1. In the following section, the nucleation process is studied by using Classical Nucleation Theory (CNT).

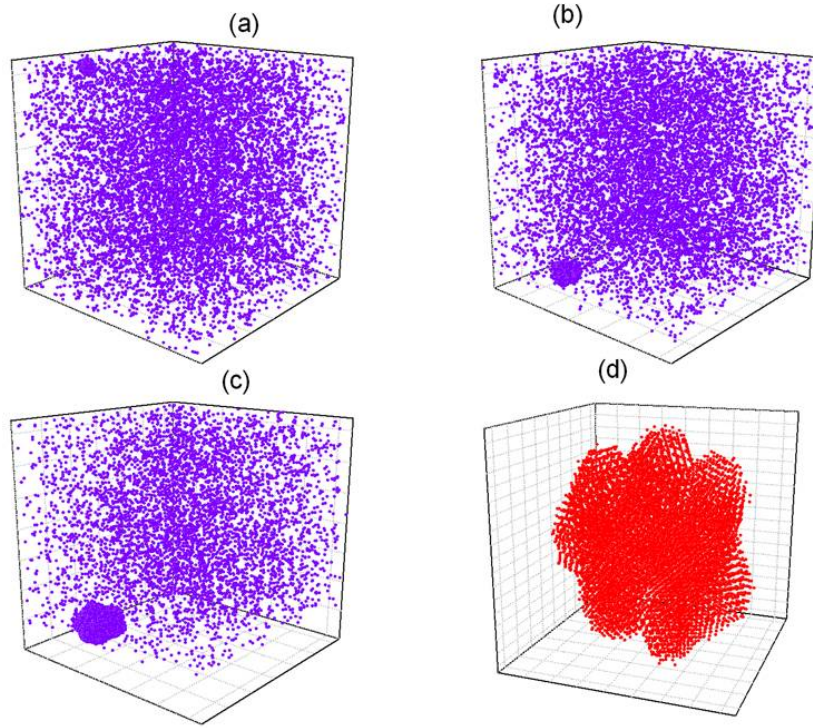


Figure 4.1: *Time evolution of a single cluster growing a) at $t = 3000$, b) at time $t = 5000$ and c) at time $t = 10000$. d) magnified nucleating cluster of the system at $t = 40,000$.*

4.1.1 Classical Nucleation Theory

According to the classical nucleation theory, as a new phase is formed in an old phase, two competing forces contribute to the formation of a droplet [27]. One of the contributions comes from the fact that there is a gain in bulk energy of the new phase as the size of the nucleus grows and is commonly known as the bulk free energy. But, as the cluster of the new phase appears, some work has to be done to create an interface between the two

phases and is known as the surface free energy. So, the overall free-energy required to form a homogeneous cluster of radius R results from these two competing energies and is given as;

$$\Delta G(R) = \frac{-4\pi R^3 \Delta\mu}{3\nu_0} + 4\pi\gamma R^2 \quad (4.1)$$

where $\Delta\mu$ is the change in chemical potential between the two phases, γ is the interface energy separating the two phases (also known as interface tension) and ν_0 is the volume of each monomer in the cluster. The minimum separation of the particles in the nucleating NPSC coincides with the minima of total interaction potential between the nanoparticles, which is $1.33d$ (where d is the diameter of the particle) for the case of C12. Thus, we considered the effective volume of the nucleating cluster as $\nu'_0 = \frac{\pi d'^3}{6}$ where $d' = 1.33d$.

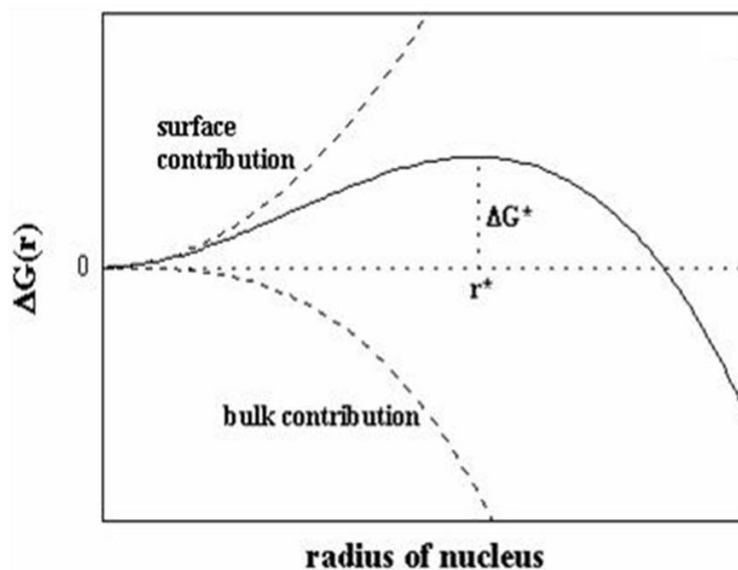


Figure 4.2: Schematic drawing of the overall free energy of the droplet as a function of the size of the cluster along with the competing terms .

A balance between these two competing terms will give rise to the critical size of the stable nucleating NPSC. A schematic representation of these competing terms and the overall free energy is shown in the figure 4.2. To estimate the critical size of the nucleating cluster, we can solve equation 4.1 as a function of the size of the nucleating cluster. The

critical size cluster is found to be

$$n^* = \frac{32\pi\gamma^3v_0^2}{3(\Delta\mu^3)} \quad (4.2)$$

The critical size of the nucleating NPSC n^* can be estimated if we can find a way to figure out the values for unknown parameters (i.e. γ and $\Delta\mu$) in our simulation.

Evaluation of $\Delta\mu$

Mathematically, the change in chemical potential (also known as *supersaturation*) is written as

$$\Delta\mu \equiv \mu_{old} - \mu_{new} \quad (4.3)$$

Physically speaking, the *supersaturation* is the gain in free energy per particle during the phase transition from an old phase (e.g. gas or liquid) to a new phase (e.g. solid). We can compare our system with the condensation of a vapor system. In this case, the change in chemical potential from an old phase to a new phase depends upon the pressure p of the vapors. So, the chemical potential in the old phase is given by

$$\mu_{old}(p) = \mu_e + kT \ln(p/p_e) \quad (4.4)$$

and in the new phase, chemical potential is given by

$$\mu_{new}(p) = \mu_e + \nu_e(p - p_e) \quad (4.5)$$

where $p_e(T)$ is the phase-equilibrium pressure and $\mu_e = \mu_{old}(p_e) = \mu_{new}(p_e)$ is the chemical potential of the vapors. Using equations 4.4 and 4.5 into 4.3, we can write the change in chemical potential as [19]

$$\Delta\mu = kT \ln(p/p_e) - \nu_0(p - p_e) \quad (4.6)$$

Since, usually $\nu_0 p_e \ll kT$, so we can approximate the above equation 4.6 as

$$\Delta\mu = kT \ln(p/p_e) \quad (4.7)$$

Also, in our simulations, since we work at low volume fractions (i.e. dilute system), we can approximate the pressure as the volume fraction f of our system such that the equation 4.7 can be written as

$$\Delta\mu = kT \ln(f/f_e(T)) = kT \ln(S) \quad (4.8)$$

where S is defined as the *Supersaturation* of the system.

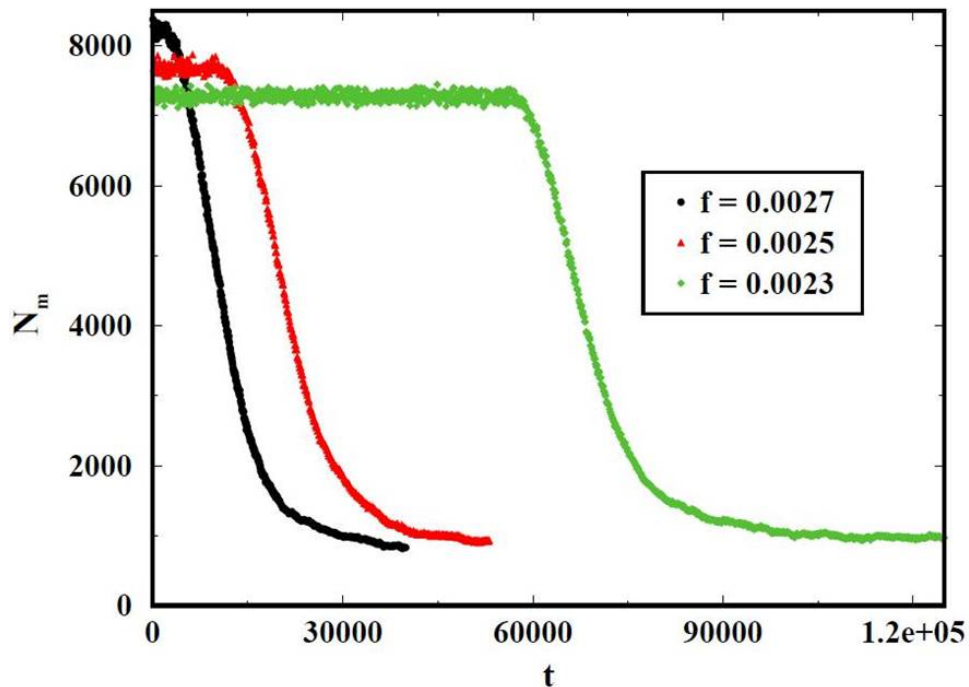


Figure 4.3: Variation of the number of unaggregated monomers left in the system N_m as a function of time. The curves show the variation of the monomers left in the system at three different volume fractions of $f=0.0027$ (black symbols), 0.0025 (red symbols) and 0.0023 (green symbols) respectively. The equilibrium volume fraction of unaggregated monomers is estimated as $f_e = 0.0002$.

Transition from a dispersed phase to a state in which the solid phase starts to develop is observed in the simulations when the monomer volume fraction f is larger than a critical value f_e . To estimate the equilibrium volume fraction $f_e(T)$, we look at the number of monomers left in the system as the solid phase grows in the system.

A plot of the variation in the number of monomers left in the system N_m is shown

in figure 4.3 for three different volume fractions. Since, we are quenching at the same temperature, from figure 4.3, it can be seen that even though the initial value of N_m is different for all three different volume fractions f , all values of N_m ultimately settle to one value of 0.0002. A constant value of monomers at this volume fraction indicates that two phases are at equilibrium at this volume fraction (i.e equilibrium volume fraction, f_e). The constant values of monomers at initial times (i.e. higher constant values) in the figure 4.3 are indicative of the fact that there is no solid phase appear in the system during that time and also that if quenched at different volume fractions, solid phase may appear at different times, although not necessarily in the same order.

So, by using this estimated value of f_e , we can determine different values of change in chemical potential (or *supersaturation*) by quenching our nanoparticle system at different volume fractions, f .

Evaluation of the interface tension γ

According to classical nucleation theory (CNT), the nucleation rate or the nucleation frequency J is related to the activation barrier energy $\Delta G(R)^*$ as

$$J = J_0 \exp\left(\frac{-\Delta G(R)^*}{kT}\right) \quad (4.9)$$

Furthermore, the induction time t_{ind} can be used as a measure of the nucleation frequency, where the induction time t_{ind} can be defined as the time elapsed between the creation of supersaturation and formation of nuclei of critical size, such that one can describe it by the relation [21]

$$t_{ind} \propto J^{-1} = C \exp\left(\frac{\Delta G(R)^*}{kT}\right) \quad (4.10)$$

or we can write

$$t_{ind} = C \exp\left(\frac{16\pi v_0'^2 \gamma^3}{3(kT \ln S)^2}\right) \quad (4.11)$$

To determine the value of induction time in our simulations, we studied the variation of the mean coordination number (i.e., the mean number of neighbors) $C_n(t)$, for particles with at least one neighbor.

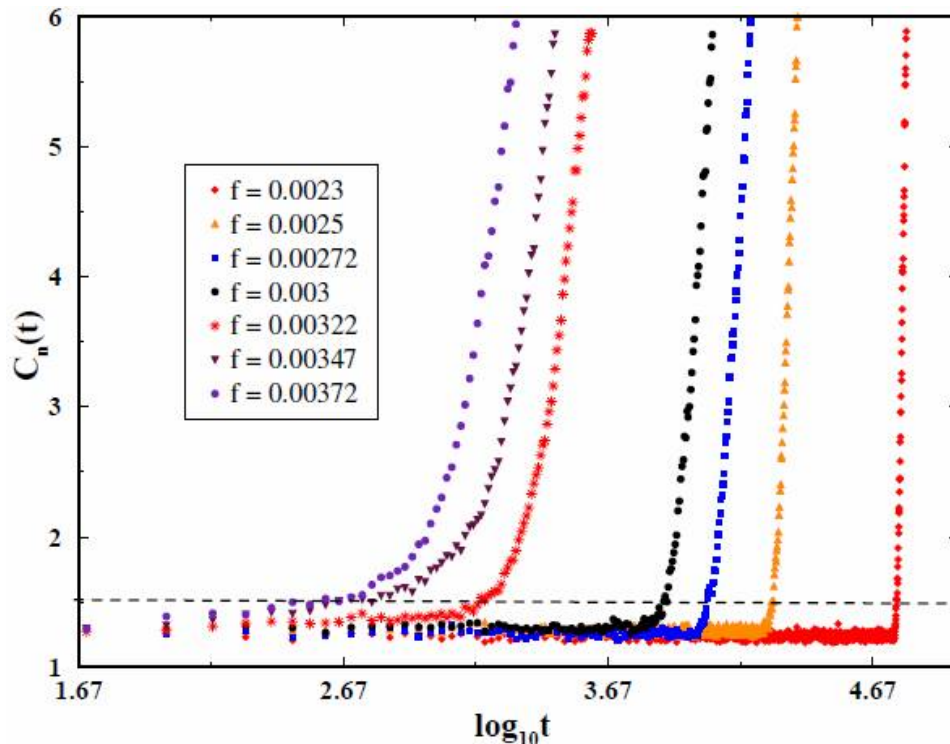


Figure 4.4: A plot of the mean coordination number $C_n(t)$ as a function of time after quenching our system at different volume fractions. The dashed line at $C_n(t) = 1.5$ is our criterion to indicates nucleation with which induction time can be determined.

Figure 4.4 shows the variation of the mean coordination number as a function of time for the system in one simulation run for various values of supersaturation. As shown in figure 4.4, $C_n(t)$ remains constant at a small value over a certain period of time and then there is a sudden rise in $C_n(t)$ indicating the formation of a critical nucleus. Choosing a particular value of $C_n(t)$ helps to determine the induction time. During our analysis, it was observed that choosing any reasonable value of $C_n(t)$ will not make any difference to the calculation of surface tension and critical size so we have chosen to take $C_n(t) = 1.5$ as the threshold for nucleation to determine induction time. The veracity of equation 4.11

for our simulation is seen in figure 4.5 where $\ln(1/S^2)$ is plotted versus t_{ind} . Figure 4.5

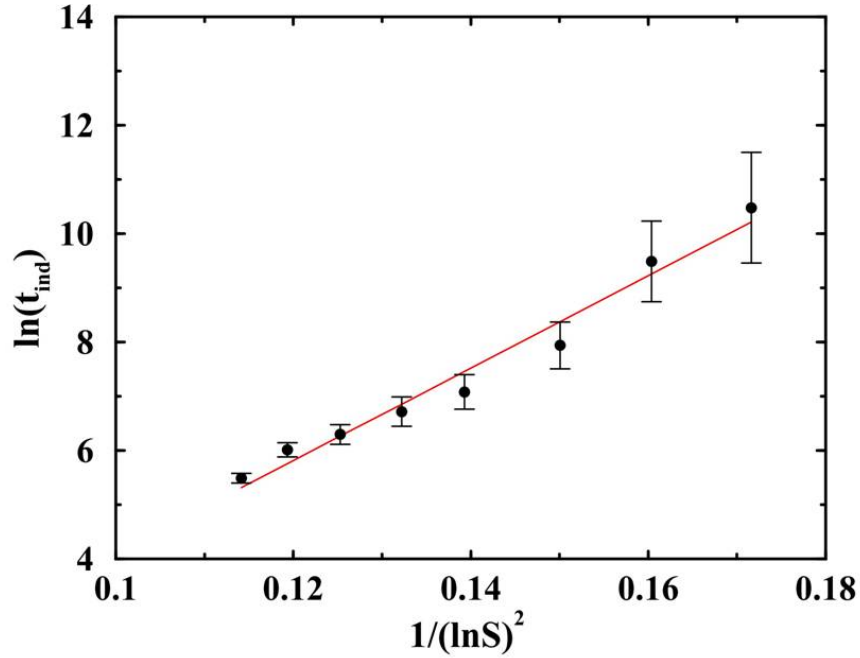


Figure 4.5: Plot of the variation in induction time versus supersaturation S (See eq. 4.11). Induction time is averaged over 10 to 20 different initial configurations for each S value. The error bars show the standard error.

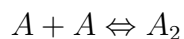
shows the plot of the induction time (t_{ind}) as a function of the *supersaturation*. For each *supersaturation* value, the induction time is calculated for 10-20 different runs. Although the error bars show a large variations in the value of induction time over different runs, still the averaged values of induction time can be seen as showing a linear behavior with $\ln(1/S^2)$, as predicted by equation 5.11. From the slope of the graph in figure 4.4, the interfacial tension γ can be calculated. In our case, the γ is found to be $\gamma = 1.3 \pm 0.05$. This value of γ is about twice the experimental value of $\gamma = 0.76kT/d^2$ obtained in [57] from a study of gold NPSC nucleating from a toluene-butadiene mixed solvent. Given the inaccuracies in our theoretical model and the errors involved in estimating γ from a simulation of a finite-sized system, such a discrepancy is not unexpected. Using this value of γ for a given *supersaturation* value in equation 4.2, we can calculate approximate size of the nucleating NPSC. The critical size value of the nucleating NPSC is found to be $n^* \approx 10$.

4.2 Dynamical and Morphological analysis of Prenucleating SCs

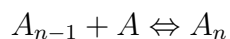
The results obtained in the above section 4.1 imply that our simulations embody CNT, so we proceed further to explore the nucleation process in our simulation and test the validity of CNT for our case, by analyzing some of its postulates. CNT assumes that the nucleating NPSC are compact in shape and the growth of the nucleating NPSC is sequenced by the addition of monomers in the system. In the following sections, we test these assumptions;

4.2.1 Cluster Dynamics

To further test the validity of CNT for our case, we observe the dynamics of the largest NPSC in the system. In order to have better understanding of the dynamics of the largest NPSC, we run 50 different simulations. The dynamics of the biggest NPSC can be divided into two regions as shown in figure 4.6. The region where the nucleating NPSC is unstable and fluctuates around an average size 10, indicated by the hatched area, is named as the prenucleating regime and the region where a nucleating NPSC smoothly grows to a stable size, is named as nucleating regime. It is worth mentioning here that out of 50 runs that we made to study the dynamics of the biggest NPSC, most of the runs show large fluctuations in the size of the NPSC in prenucleation regime while in other runs, these fluctuations are small enough to be ignored. According to classical nucleation theory (CNT), the growth of the stable nucleating NPSC arises from the bimolecular addition of the monomers in the system [20]:



.....



In order to understand the mechanism of the nucleation, we examined the fluctuations in size by looking at the change in size of the biggest NPSC ΔN between two successive time

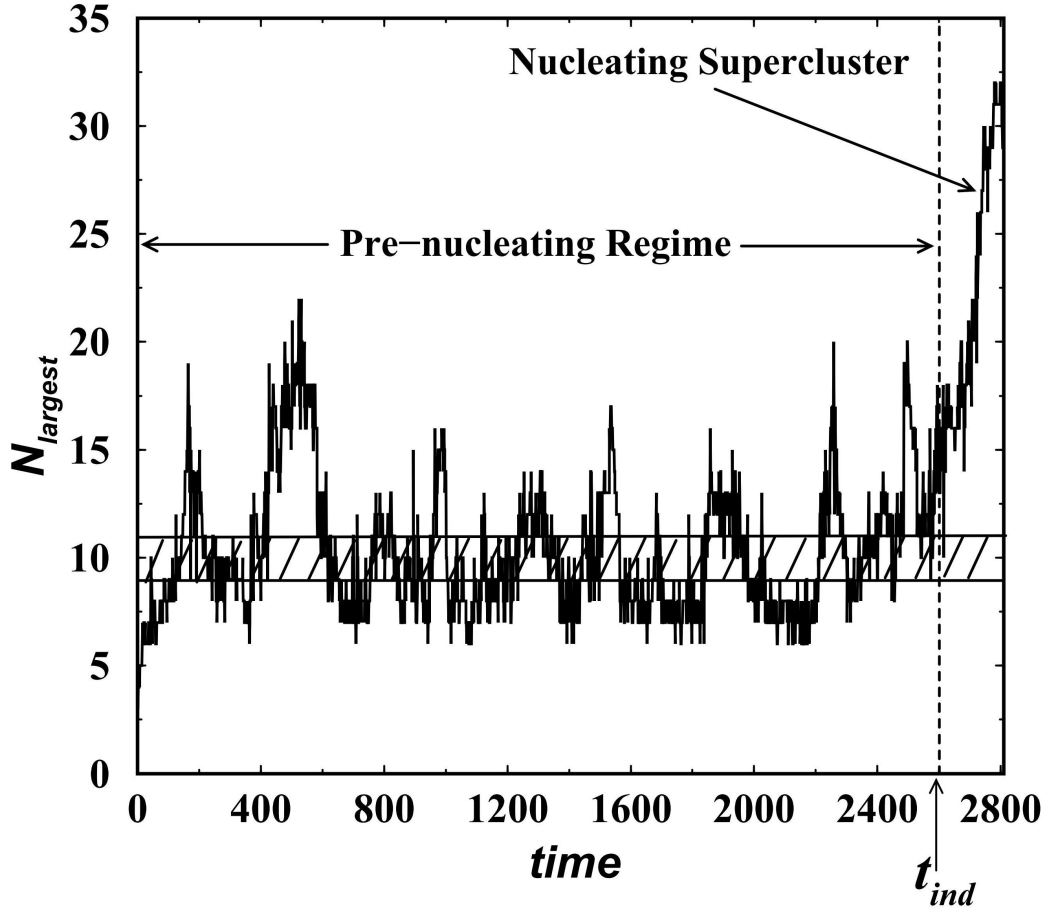


Figure 4.6: Plot showing the size fluctuations of the biggest supercluster in the pre-nucleation regime. The overall dynamics can be divided into two regimes (i.e Pre-nucleating Regime and Nucleation Regime). The induction time is $t_{ind} \approx 2600$. Excursions above the critical size of $N^* \approx 10$ (cross hatched region) can be observed in the pre-nucleation regime.

steps in both pre-nucleating and nucleation regimes. A distribution of the ΔN during the growth and fragmentation of the biggest NPSC in both regions is shown in figure 4.7.

From this distribution, it can be seen that during the growth process in both regimes, the fluctuations in size are mostly dominated by the exchange of monomers and dimers. Even though bigger NPSCs appear to contribute, seemingly due to the loosely bound structure of the biggest NPSC at initial times, still this contribution is small enough to be ignored. The dominance of addition/removal of monomers in both regimes is consistent with the CNT.

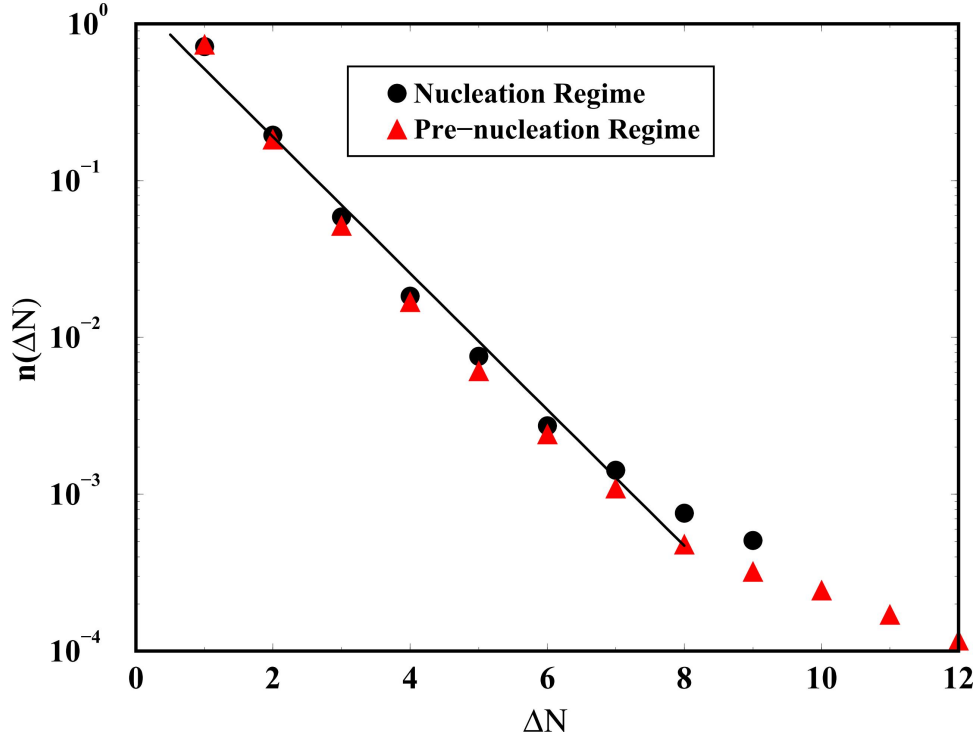


Figure 4.7: A log-linear plot of the normalized distribution of the absolute value of the change in size of biggest NPSC ΔN during consecutive time steps for both pre-nucleation and nucleating regimes. A slope is drawn as a guide to show the exponential behavior of the distribution which seems to describe the data well for smaller values of ΔN . Larger ΔN occurrences are rare and thus have much larger uncertainty..

4.2.2 Morphology and Shape of the Nucleating NPSCs

We also looked at the morphology of the biggest NPSC in both prenucleating and nucleation regimes. At early time (i.e. in prenucleating regime), the biggest NPSC appears to be non-compact (see fig. 4.8) whereas at late times (i.e. in nucleation regime), the structure of the NPSC appears to be more compact (Figs.fig. 4.8b,c,d). CNT also assumes that nucleating NPSCs are compact and spherical in shape.

In this section, we address the issue of shape by plotting the number of monomers in the pre-nucleating NPSCs as a function of the supercluster radius of gyration, R_g , for both the largest NPSC in the system and all NPSCs of specific sizes. The analysis for the biggest NPSC is averaged over 50 runs. Next, we created artificial NPSCs of relevant sizes randomly

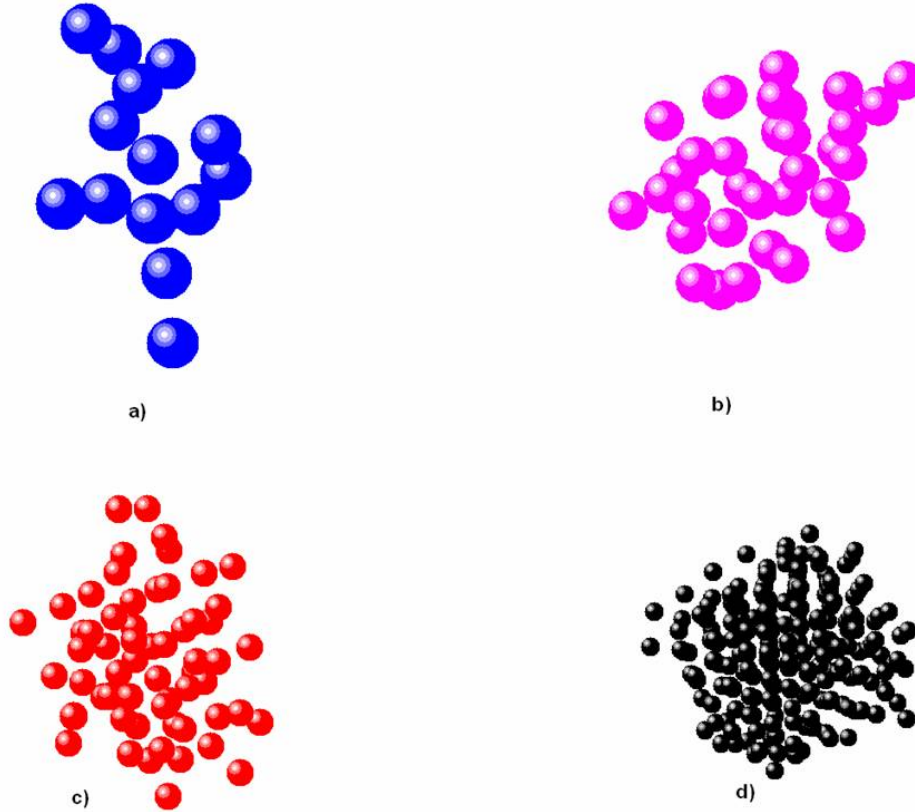


Figure 4.8: *Morphology of the biggest NPSC at various times (a) $t = 2000$ with $n_s = 14$, (b) $t = 3000$ with $n_s = 33$, (c) $t = 4000$ with $n_s = 60$ and (d) $t = 5000$ with $n_s = 209$. The approximate time for the formation of stable cluster is $t \approx 2800$. The symbol sizes for monomers are scaled so that each cluster appears to have the same linear size.*

placed on the lattice sites of pure FCC and BCC crystals using self-avoiding random walk method. Figure 4.9 shows the R_g vs N plot for the biggest NPSC in the system in the prenucleation regime and all the NPSCs present in the system at a given time and one can argue that the small pre-nucleating NPSCs are well described by self-avoiding walks on an fcc lattice. No evidence of any bcc structure in the pre-nucleating NPSCs is seen although such claims exist in the literature [62], [63]. More importantly and surprisingly, the largest NPSC in the pre-nucleating system has a compact morphology once bigger than about size $N = 10$, the critical size. Since the largest cluster plays a critical role in nucleation, the compact morphology for a size comparable to again supports the CNT scenario. Another

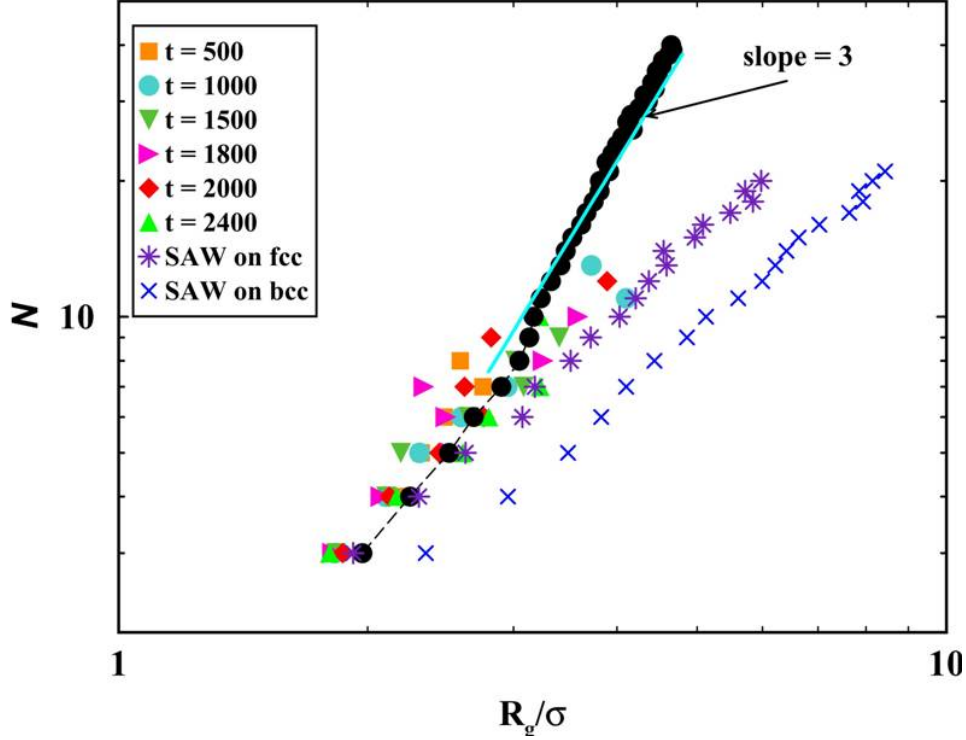


Figure 4.9: Plot of the number of nanoparticles in the supercluster versus supercluster radius of gyration for: 1) the biggest supercluster $N_{largest}$ (●) in the system (averaged over 50 runs) and 2) the other, smaller superclusters in the system at pre-nucleating times. During the pre-nucleating times, the structure of the small NPSCs in the system appears to be non-compact and well described by self-avoiding walks on an fcc lattice, while the largest size NPSCs appear to be more compact with a dimension of ca. 3.

important feature can be observed in fig. 4.6. As one can see that the excursions in the size of the biggest NPSC in the prenucleating region can be observed, leading to the formation of unstable NPSCs of size up to $N \sim 40$ in some cases; a size afar from the one predicted by CNT (i.e $N \sim 10$). These excursions indicate the formation and break-up of the biggest NPSC in the system. To understand these excursions, we compared the energy per NP between prenucleating regime and nucleating regime NPSCs. This comparison is shown in fig. 4.10 where we can see that the nucleating SCs have lower energy than the pre-nucleation NPSCs at any given size of the nucleating SC. This implies that the prenucleating NPSC fluctuates around the critical size predicted by CNT until a SC of enough lower energy

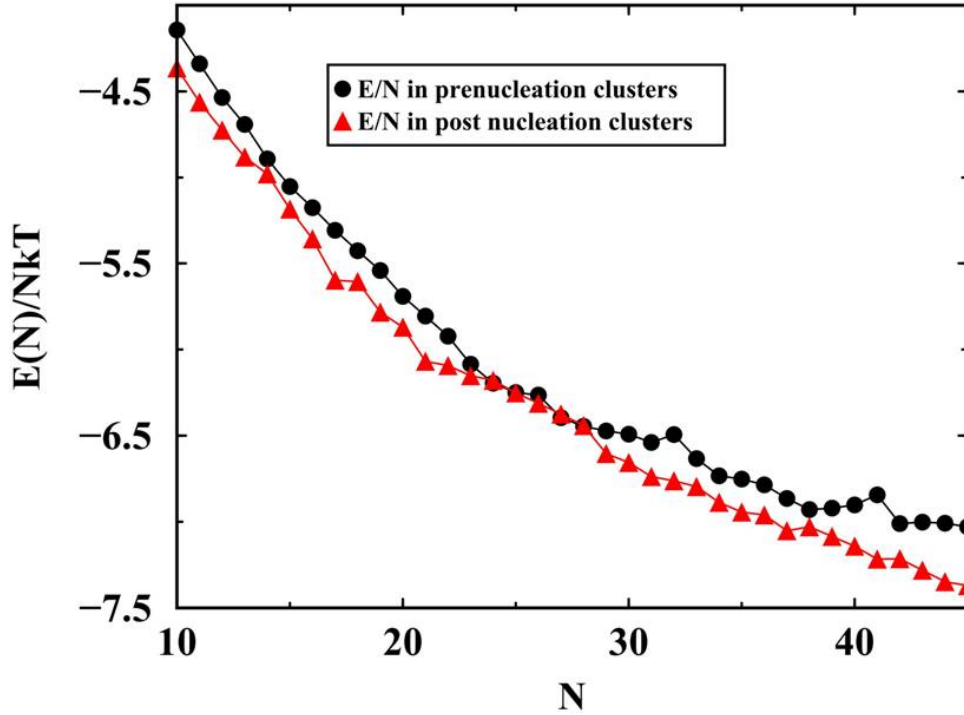


Figure 4.10: Plot of the energy per nanoparticle of the pre- and post-nucleation NPSCs as a function of the supercluster size N .

appears in the system and grows to a stable size.

4.3 Induction Time Analysis using Fisher's Droplet Model

Although the nucleation of our SCs is well described by CNT, for completeness, however, we further analyzed the energetics of the nucleation process going beyond the CNT. Such a theoretical development exists in the literature in terms of Fishers droplet model [28] which differs from the CNT by an additional contribution to the total free energy to accommodate the entropic effects of the shape of the NPSCs. According to this model, the free energy required to form a nucleating NPSC is given by,

$$\Delta G(R) = \frac{-4\pi R^3 \Delta\mu}{3v'_0} + 4\pi\gamma R^2 + \tau kT \ln\left(\frac{4\pi R^3}{3v'_0}\right) \quad (4.12)$$

where the logarithm term on the right hand side is due to the statistical mechanical treatment of the free energy which includes contributions from the translational, rotational and configurational partition functions. Lothe and Pound [64] included the translational and rotational degrees of freedom of the NPSC. According to their theory, $\tau = -4$. Fisher obtained τ to be 2.2 arising from configurational entropy contributions [65]. Other modifications of this model were carried out by several groups. For example, Reiss, Katz, and Cohen included the center of mass fluctuations and Reiss assumed the nucleating droplet as liquid drop and made appropriate modifications. Fisher's theory is found to be in good agreement with experimental results [66], [67]. Later, further modifications were proposed by Lowe and Wallace to account for the presence of smaller clusters in the system [68] and argued that works best to explain experimental data. We have used a modified Fisher droplet model and used to be 1.25 for our analysis. Since, from 4.10, we can relate induction time $t_{ind}(i) = C \exp(\frac{\Delta G^*(S_i, \gamma)}{kT})$ with different *supersaturation* values; for $i = 1, 2, 3$. To estimate the value of γ , we solve this transcendental equation by taking the ratio of the induction time t_{ind} for any of the two given *supersaturation* values as mentioned in the equation 4.13 below;

$$\frac{t_{ind}(i)}{t_{ind}(j)} = \frac{C \exp(\frac{\Delta G^*(S_i, \gamma)}{kT})}{C \exp(\frac{\Delta G^*(S_j, \gamma)}{kT})} \quad (4.13)$$

or we can write

$$\ln\left(\frac{t_{ind}(i)}{t_{ind}(j)}\right) = \Delta G^*(S_i) - \Delta G^*(S_j) \quad (4.14)$$

Plotting both sides of the above equation versus γ , we can obtain the approximated value of γ from the intercept of these two curves as shown in the figure 4.11. After solving equation 4.14 for different volume fractions, we find the value of γ to be about $\gamma = 1.5 \pm 0.5kT/\sigma'^2$. This value of γ compares well to the one calculated earlier from the CNT. Using this value of γ , the critical size of the cluster, n^* , calculated from this model, for a given supersaturation S ,

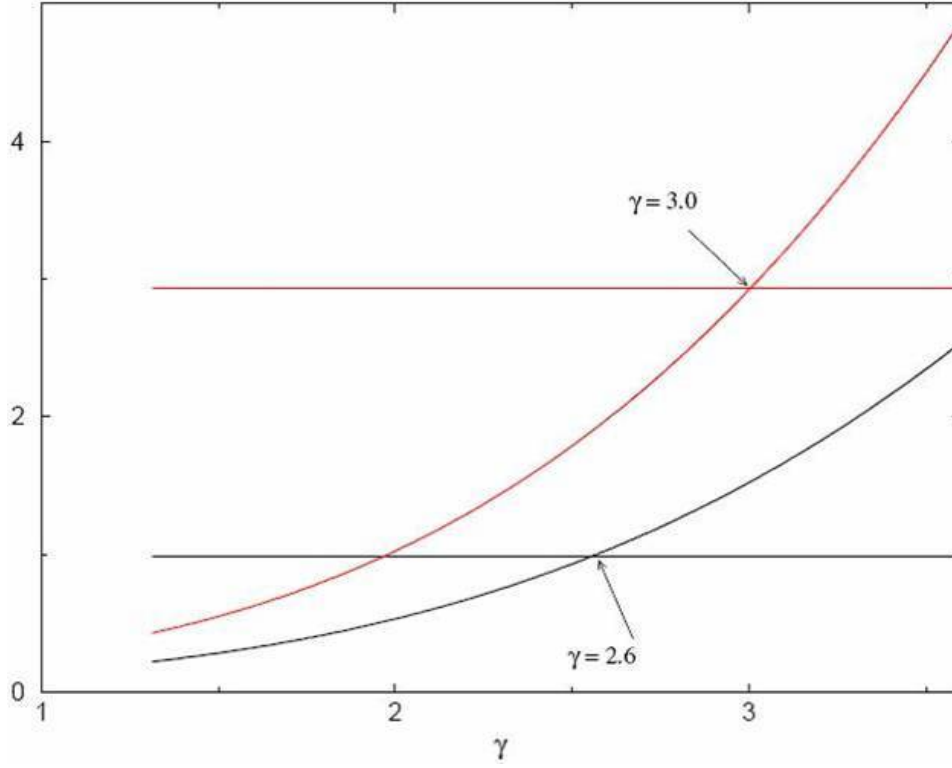


Figure 4.11: A Plot of LHS and RHS of equation 4.14. The constant lines indicate LHS of the equation 4.14 while the curved lines show the RHS of the equation for the two given supersaturation values, showing the variation of γ from minimum of 2.6 to maximum value of 3.0.

is slightly bigger in comparison to the CNT as shown in the Table 4.1. From these results,

Table 4.1: Comparison of the critical size n' between CNT and Fisher Model

S	$S_1(10.95)$	$S_2(11.9)$	$S_3(12.95)$	$S_4(14.28)$	$S_5(15.33)$	$S_6(16.52)$
$n'(CNT)$	9.5	8.5	7.5	6.75	6.25	5.75
$n'(FisherModel)$	12	11.2	10.3	9.5	8.3	7.4

we can conclude that the introduction of the logarithmic term to the CNT does not have a strong effect on the calculations of γ and n^* in our system.

4.4 Aggregation at Higher Volume Fractions

When ligated nanoparticles are mixed with a solvent (Toluene in our case), their aggregation produce different results depending on how far the system is from equilibrium. Aggregation is a process which leads to nonlocal formation of larger clusters of particles. These clusters are formed either by the aggregation of smaller clusters or by the addition of monomers in the system. After quench, if the particles in the bulk can find adjustable position in the growing cluster and can find the suitable position to minimize the surface energy, the growing clusters are assumed to have compact morphology. On the other hand, if the added particles to the cluster stick irreversibly at the point of contact with the aggregate, irregular shaped clusters are formed. As mentioned above, the growing process of the aggregates can be formed due to the addition of monomers known as particle-cluster aggregation or it can be formed due to the small size aggregates known as cluster-cluster aggregation. Furthermore, aggregation also depends on how the particles approach each other (i.e. their trajectory can be either Brownian or Ballistic). Using above mentioned rules, different models are used to describe the aggregation processes. If the two approaching particles stick together immediately and forever, the rate of aggregation is limited by the diffusion mechanism and the aggregation is called the diffusion limited aggregation. If there is a small repulsion involved in the growth then the aggregation is called the *reaction limited aggregation*. In one more possibility, there is a finite probability of dissociation and this process is called the *reversible aggregation* [69]. To understand the morphology and growth kinetics in the dense (at higher volume fraction) systems, we quenched our dodecanethiol (C_{12}) and decanethiol (C_{10}) ligated system at rather higher volume fractions (i.e. $0.005 \leq f \leq 0.02$) [61]. In this section, we will analyze the growth and morphology of the growing NPSCs in our system of C_{12} and C_{10} ligated gold nanoparticles in Toluene. Our analysis is based on the dynamical variations in the NPSC size and their average radius of gyration in the system. Furthermore, we also looked at the morphology of the NPSCs by calculating the *structure factor* of the NPSCs in the system.

4.4.1 Structure Factor

Since, we can relate the scattered field E_{sca} with the scattering wave vector as $E_{sca} \propto \exp(-i\vec{q}\cdot\vec{r})$ where $\vec{q} = \vec{k}_i - \vec{k}_s$ is the momentum transfer between the incoming and scattered wave (or the difference between the incoming and the outgoing wave vectors) and q^{-1} represents the length scale to be compared to the length scale of the scatterer. Under the assumption of elastic scattering, it can be related to the scattering angle θ as;

$$q = \frac{4\pi}{\lambda_0} \sin \frac{\theta}{2} \quad (4.15)$$

For a system of N particles, the scattered intensity $I(q)$ is the square of the scattered amplitude (i.e. $I(q) = |\sum \exp(-i\vec{q}\cdot\vec{r})|^2$). The *Structure Factor* $\mathbf{S}(\mathbf{q})$ is proportional to the scattering intensity and is defined as

$$S(q) = \frac{1}{N} \langle |\sum \exp(-i\vec{q}\cdot\vec{r})|^2 \rangle \quad (4.16)$$

As the magnitude in Eq. 4.16 is the product of the sum and its complex conjugate, $S(q)$ can be written as

$$S(q) = \frac{1}{N} \langle \sum_i \sum_j \exp(-i\vec{q}(\vec{r}_i - \vec{r}_j)) \rangle \quad (4.17)$$

where r_i and r_j represent the positions of the i th and j th scatterers. The *Structure Factor* $\mathbf{S}(\mathbf{q})$ can be defined as the fourier transform of the correlation function $C(r)$ for a system with randomly oriented aggregates;

$$S(q) = 4\pi \int_0^\infty C(r) \frac{\sin(qr)}{qr} r^2 dr \quad (4.18)$$

For the intermediate q regime (regime corresponding to the interparticle distance in the cluster), we can assume that $C(r)$ has power law behavior such that its functional form is given by the expression $C(r) = r^{D-3} f(r/R)$. Here, $f(r/R)$ is the cut-off function for the correlation function such that $f = 0$ for $r \geq R$ where R is the size of the cluster. Using this form for $C(r)$ in equation 4.18, one finds;

$$S(q) \sim q^{-D} \int_0^\infty f(z/qR) \sin(z) z^{D-2} dz \quad (4.19)$$

where $z = qr$. Furthermore, considering the fact that the integral in equation 4.19 is convergent for $D < 2$, we can write that in the intermediate regime, $S(q) \sim q^{-D}$.

4.4.2 Growth Kinetics in C_{12} Ligated System

In this section, we will focus on the growth kinetics and morphology of the clusters formed at higher volume fractions in our C_{12} ligated system. First, we observe the morphology by looking at the snapshots of the simulation clusters. For $f > 0.003$, several clusters are found to nucleate and grow with time in the system. This can be seen in Figure 4.12A for $f = 0.005$, for example, where several spherical clusters grow in the system indicating a compact morphology of the clusters. Next, we quenched at further higher volume fraction of $f=0.02$. For such dense system (such as shown in Figure 4.12B for $f=0.02$), the morphology of domains is quite similar to the interconnected structure seen in a typical spinodal decomposition of a liquid-liquid mixture. Also, by focusing on one individual cluster for both $f = 0.005$ and 0.02 , we were able to see the ordered close-packed structures of the clusters.

In order to study the kinetic growth of these clusters in the system, we studied the variation in the shape of the growing clusters. For that matter, we calculated the radius of gyration R_g of these growing clusters. In Figure 4.13, we show log-log plots of the average radius of gyration R_g of the clusters as a function of time for $f = 0.005$. The data shown in the figure is averaged over 10 runs. As we can see from the figure 4.13 that for $f = 0.005$, we see three regimes in the growth kinetics. First, there is an induction period ($t \leq 300$) where droplets of critical size are yet to nucleate and hence only small clusters of fluctuating sizes are observed in the system. This regime is then followed by second regime where nucleating clusters are found to have sudden fast growth corresponding to the heterogeneous nucleation of many clusters ($300 \leq t \leq 3000$). Subsequently, these clusters grow with time with a power law of $R_g \approx t^n$ with $n \approx 0.16$. Although the data at this stage show large fluctuations even after averaging over 10 runs, one can understand the observed value of the exponent n in

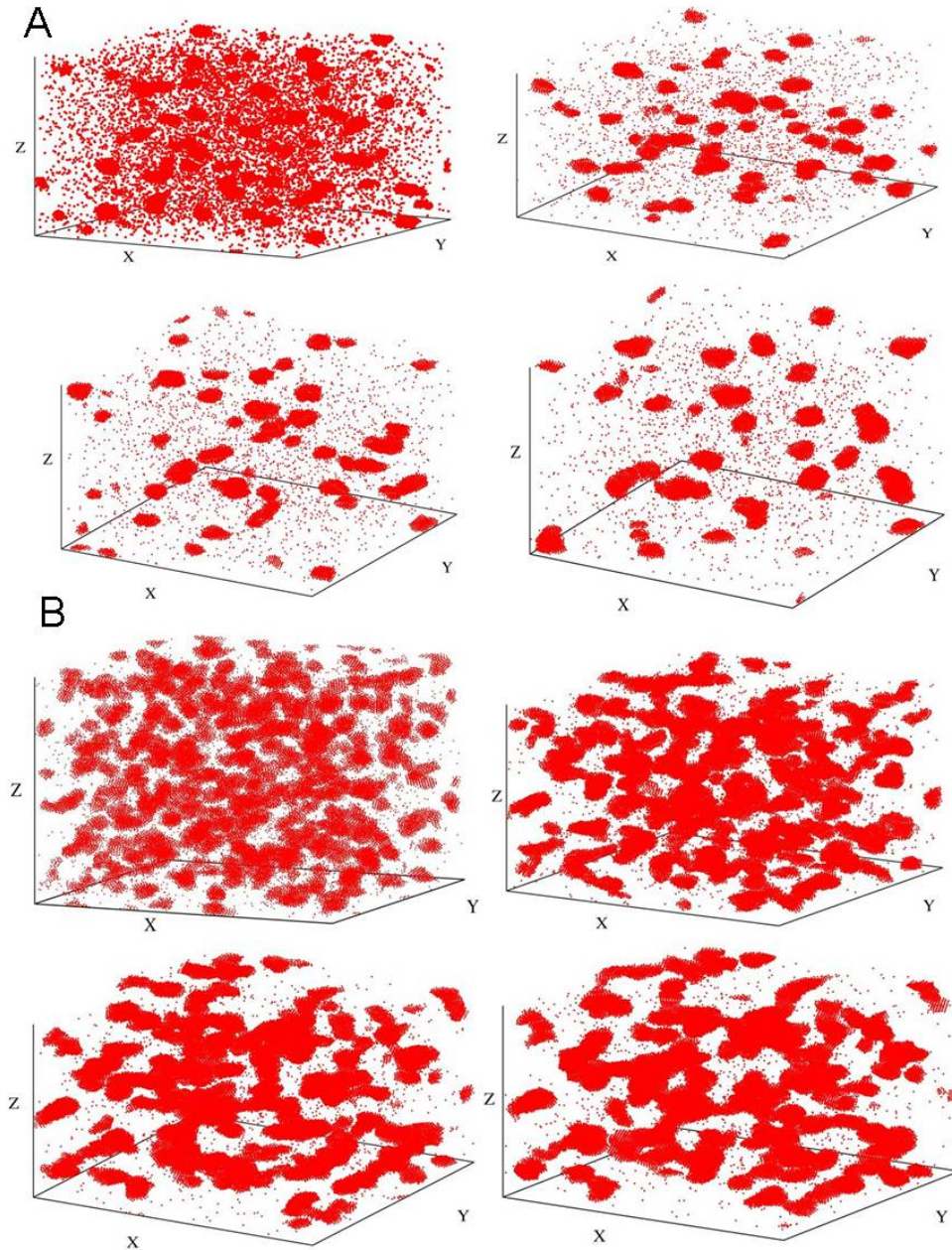


Figure 4.12: (A) Simulation snapshots for dodecanethiol-ligated nanoparticles at different times for a volume fraction of $f=0.005$: (a) $t=1000$, (b) $t=3000$, (c) $t=5000$, (d) $t=10,000$. (B) Simulation snapshots for dodecanethiol ligated nanoparticles at different times for a volume fraction of $f = 0.02$: (a) $t=500$, (b) $t=1000$, (c) $t=4500$, (d) $t=6000$.

the following ways. As first suggested by Binder and Stauffer [70] and nicely summarized by Furukawa, [71], the domain growth kinetics at this stage is mostly controlled by surface

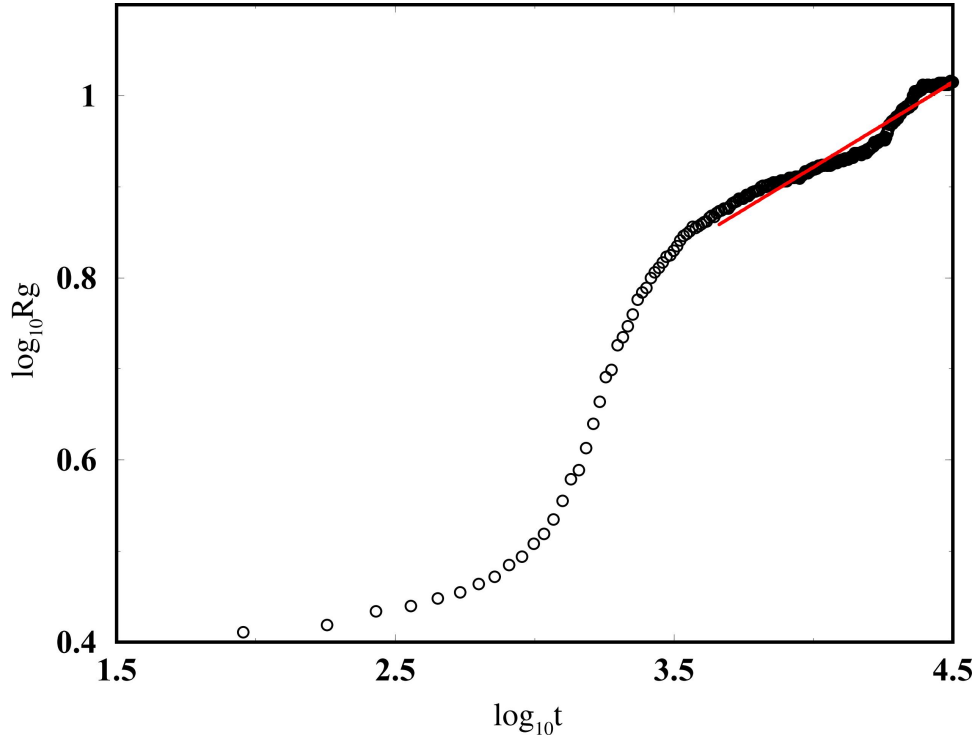


Figure 4.13: *Log-log plot of the radius of gyration (R_g) versus time for dodecanethiol-ligated nanoparticles. Here the volume fraction is $f = 0.005$. The solid line yields an exponent of ~ 0.16 . Even after averaging over 10 runs, the statistics are poor here because there are relatively few clusters formed at this volume fraction. Simulations with a much larger system would be necessary to get better statistics on the clusters at long times.*

reorganization of the clusters in order to reduce interfacial tension. In such a case of domain growth, one obtains $n=1/(D+3)$ where $D=3$ is the spatial dimension of the system. Our observed value of $n \approx 0.16$ agrees with the theoretical prediction. Next, we study the dynamics at higher volume fraction of $f = 0.02$. A plot of the cluster dynamics is shown in figure 4.14. In this case, the domain growth is so fast that we did not observe any induction period and the growing clusters are found to follow the power law of $R_g \approx t^n$ with $n \sim 0.3$ over a long period of time. This value of the exponent is consistent with a domain growth exponent of $n = 1/3$ in the spinodal decomposition of off-critical liquid-liquid mixtures [72], (when hydrodynamic interactions are not important).

Next, we further analyzed the morphology of the clusters by calculating the *Structure*

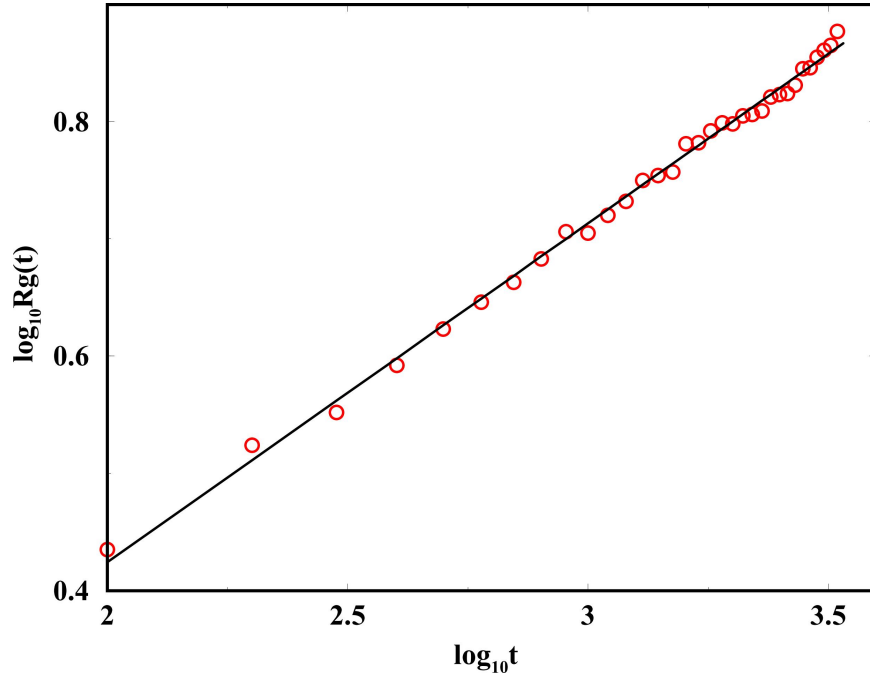


Figure 4.14: Log-log plot of the radius of gyration (R_g) versus time for dodecanethiol-ligated nanoparticles. Here the volume fraction is $f = 0.02$. The solid line yields an exponent of ~ 0.3 .

Factor $S(q)$ for the volume fraction of $f = 0.02$. A plot of the Structure Factor $S(q)$ is shown in figure 4.15. In Figure 4.15(A), we show the log-log plot of the structure factor $S(q,t)$ versus q . A fit to the data shows that $S(q)$ is consistent with Porod's law ($S(q) \sim q^{-4}$) over a large range of q values, confirming our direct observations that the growing clusters are compact at both short and large length scales. Phase-separation processes in liquid mixtures can be described by a dynamical scaling form with a time-dependent characteristic length. [73] A major feature of this description is that the structure factor $S(q, t)$ can be written in a time-independent dynamical scaling form $k_m^d(t)S(q, t) = F[q/q_m(t)]$ where $q_m(t)$ is the location of the peak in the structure factor and is a measure of the (inverse) characteristic length in the system. We have tested the dynamical scaling hypothesis for domain growth in quenched nanoparticle solutions for $f = 0.02$. The results are shown in Figure 4.15B. Reasonably good scaling is observed in the simulation over the time interval shown in the

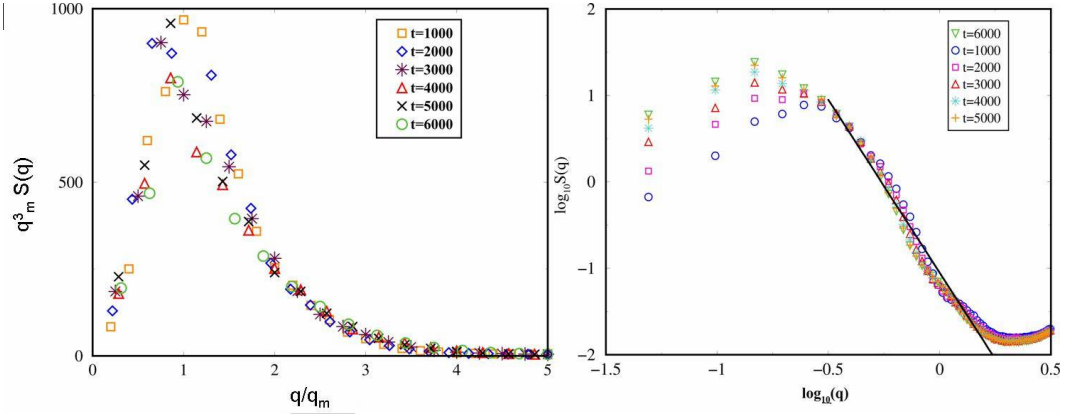


Figure 4.15: (A) Log-log plot of the structure factor at different times for dodecanethiol-ligated nanoparticles. Here the volume fraction is $f = 0.02$. The solid line yields a slope of -4 (Porod's law), indicating the compact structure of the clusters at both short and large length scales. Deviations from Porod's law might arise from finite-size effects. Simulations of a much larger system size would be necessary to get more accurate results for the structure factor. (B) Dynamical scaling plot for the structure factor (see text) for dodecanethiol-ligated nanoparticles.

Figure 4.15(B). We also note that the quality of scaling actually improves at late times.

4.4.3 Growth Kinetics in C_{10} Ligated System

In this case, the potential well depth is deeper than for the previous case of C_{12} studied in our simulations. Here also, our analysis is confined to same two volume fractions of $f=0.005$ and $f=0.02$. By looking at the snapshots of the system for both volume fractions, the large-scale morphology is fractal-like as seen in Figure 4.16(A,B) whereas the short-range close-packed ordering becomes clear as we focus on individual clusters (Figure 4.16C). So, the C_{10} ligated system is seen to have hybrid morphology and such hybrid morphology of clusters has previously been seen in both simulations [74], [17] and experiments [75], [76] of colloidal self-assembly.

The hybrid morphology of the clusters observed in real space leaves its mark on the structure factor as well. In Figure 4.17, we show the log plot of *structure factor* $S(q, t)$ versus q . A fit to the data shows that $S(q)$ is consistent with Porod's law ($S(q) \approx q^{-4}$) for large q

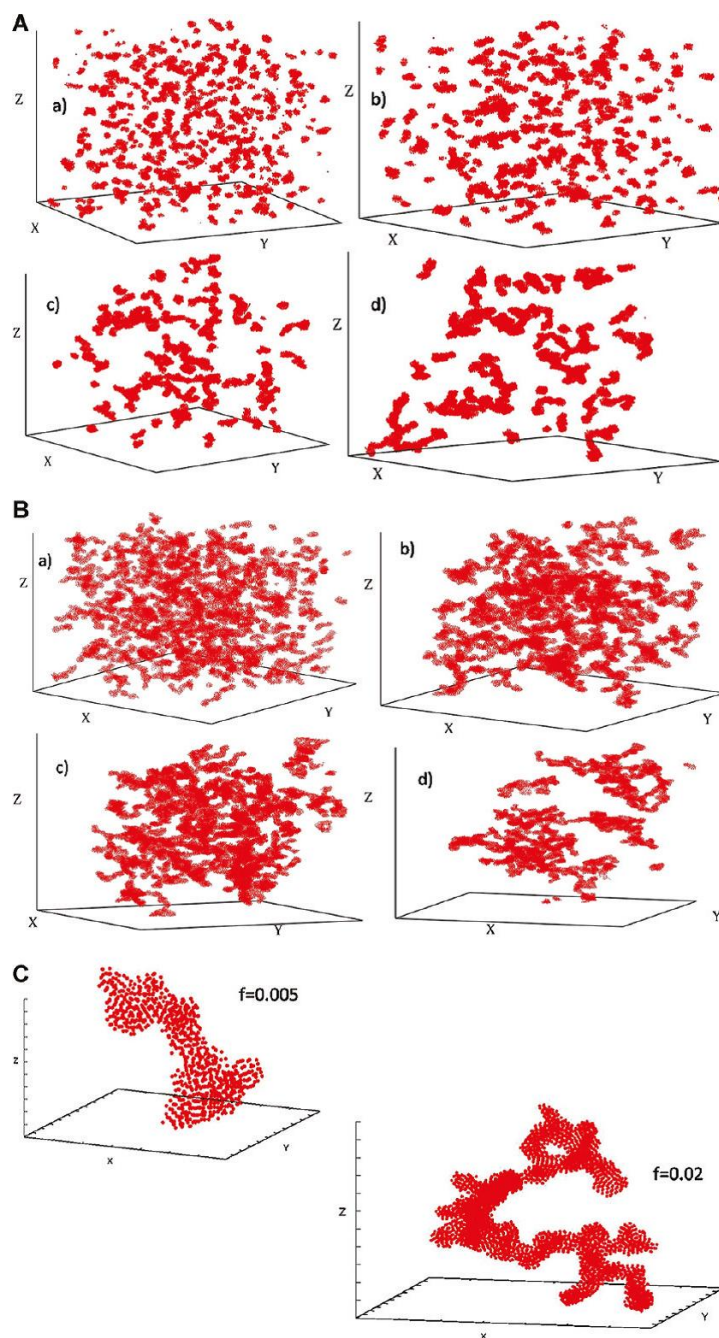


Figure 4.16: (A) Simulation snapshots for decanethiol-ligated nanoparticles at different times for a volume fraction of $f = 0.005$ (a) $t = 500$, (b) $t = 1000$, (c) $t = 5000$, (d) $t = 10000$. (B) Simulation snapshots for decanethiol-ligated nanoparticles at different times for a volume fraction of $f = 0.02$ (a) $t = 500$, (b) $t = 2000$, (c) $t = 3000$, (d) $t = 4000$. (C) Close-up structure of decanethiol-ligated nanoparticle clusters for volume fractions of $f = 0.005$ and 0.02 .

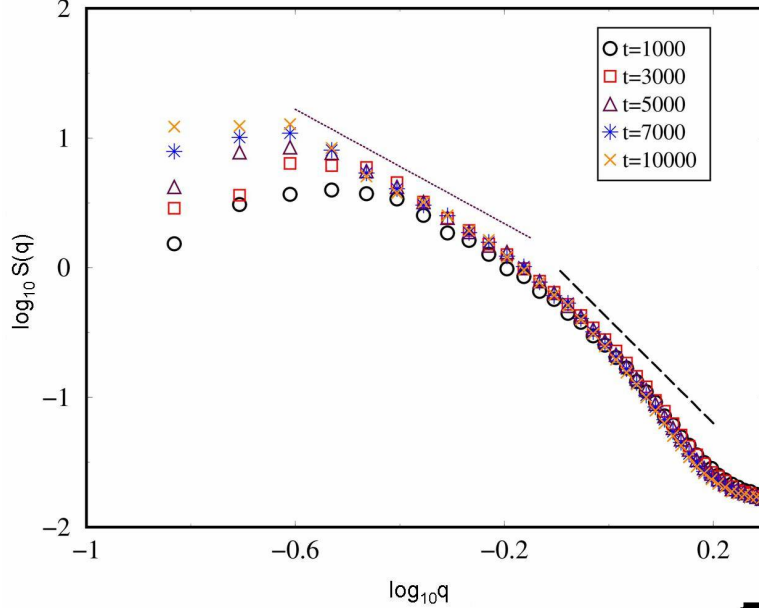


Figure 4.17: *log-log plot of the structure factor at several times for decanethiol-ligated nanoparticles with $f=0.005$. The two dashed lines yield exponents of ~ -1.8 and ~ -4 , respectively, indicating the hybrid nature of the clusters with a short length scale compact structure and a large length scale DLCA-type fractal structure.*

values, whereas for intermediate values of q , $S(q) \approx q^{-D_f}$ with $D_f \approx 1.8$ consisting of the well-known diffusion-limited cluster-cluster aggregation (DLCA) value [77]. This confirms our direct observations that the growing clusters are compact at short length scales but are fractal-like at large length scales. For fractal cluster growth in the traditional DLCA model, one can use kinetic theory based on the Smoluchowski equation for irreversible aggregation [78]. At late times, one finds that the mean cluster size grows as $s(t) \approx t^z$ where the kinetic exponent is $z = 1$ for Brownian coagulation. Because the total number of monomers is fixed in the system, the number of clusters N_c then decays with time as $N_c \approx t^{-z}$. In addition, if the fractal dimension of the clusters is given by D_f , then $s \approx R_g^{D_f}$ or $R_g \approx t^n \approx t^{z/D_f}$ with time, yielding $n = z/D_f$. For the 3D DLCA model, $D_f \approx 1.8$ and one finds $n \approx 0.55$.

Our results for R_g versus t and N_c versus t are shown in Figure 4.18A,B in the log-log plots. Figure 4.18 A shows the temporal evolution of R_g for volume fractions of 0.005 and

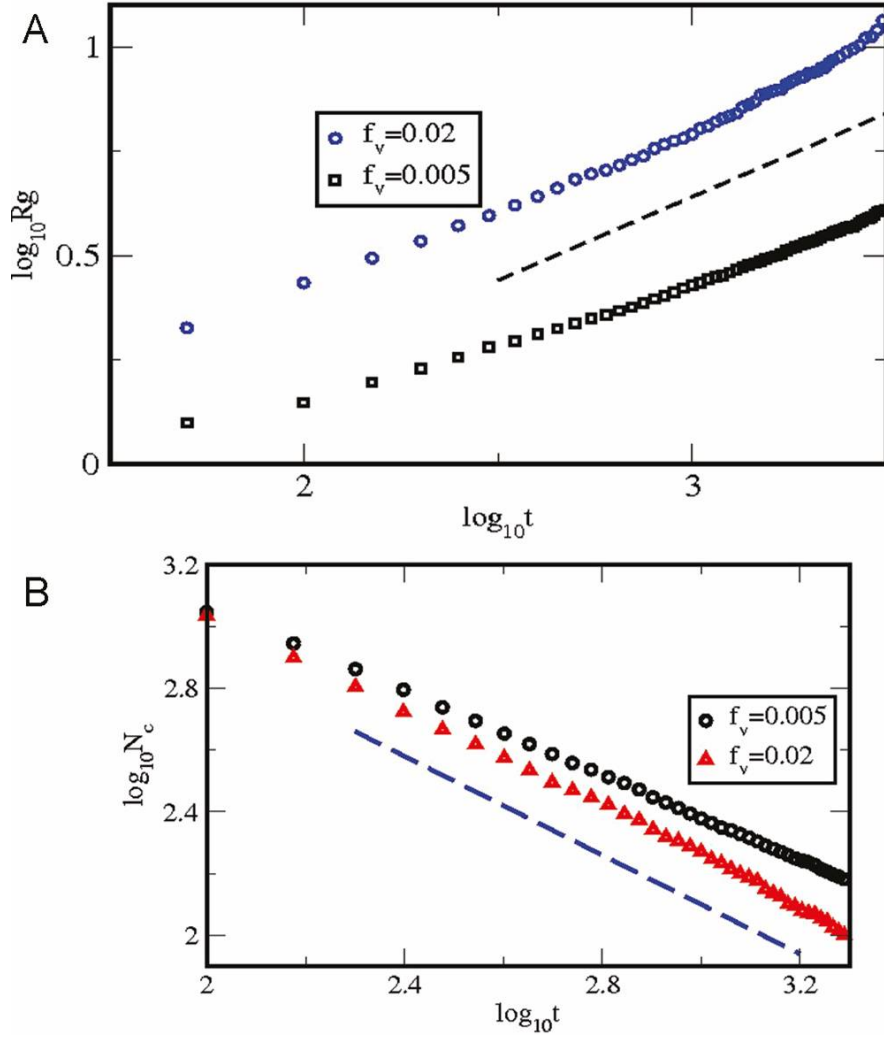


Figure 4.18: (A) *log-log* plot of the radius of gyration (R_g) versus time for decanethiol-ligated nanoparticles with $f=0.005$ and 0.02 . The dotted line yields an exponent of ~ 0.45 . (B) *log-log* plot of the number of clusters (N_c) versus time for decanethiol-ligated nanoparticles with $f = 0.005$ and 0.02 . The dotted line yields an exponent of ~ -0.8 .

0.02. Both curves yield a slope of 0.45. In Figure 4.18B, the variation of the number of clusters N_c with time is plotted on a log-log scale. The curves yield a slope of -0.8. From the kinetic exponents observed in Figure 4.18A,B, it seems that although the potential well is deeper for the decanethiol ligand case, the growth kinetics still does not belong to the pure DLCA model. To test whether the DLCA model is truly recovered when the potential well depth is extremely deep, we set $kT = 0.5kT_{room}$ in the next set of simulations. This would

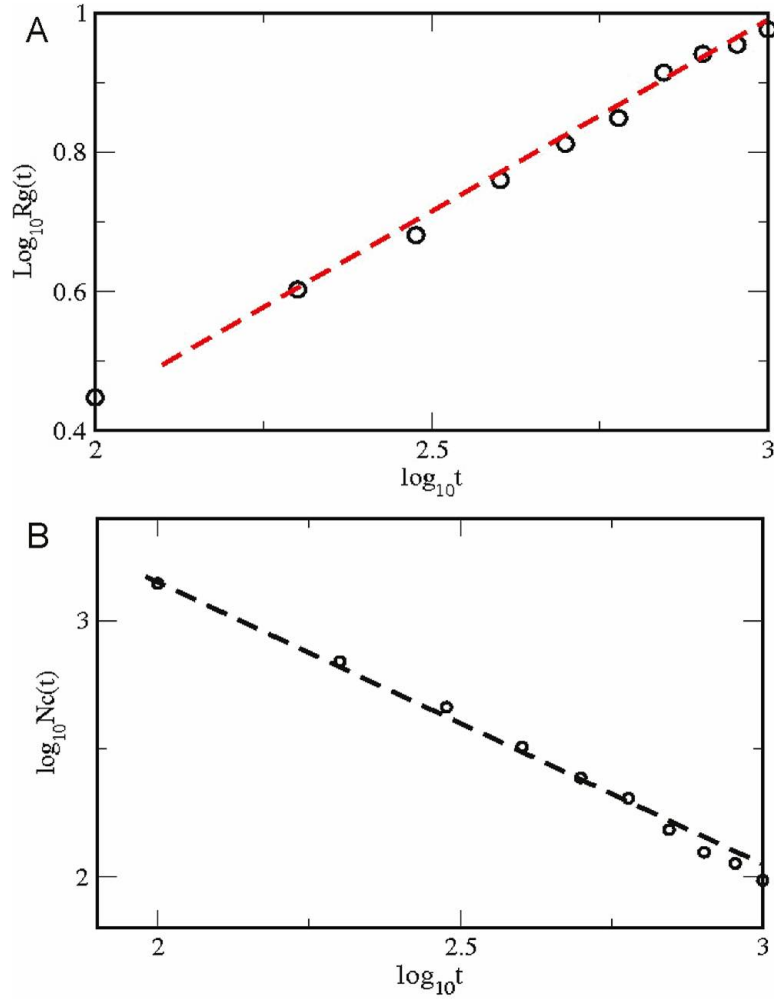


Figure 4.19: (A) *log-log plot of the radius of gyration (R_g) versus time for deeply quenched decanethiol-ligated nanoparticles with $f = 0.02$. The solid line yields an exponent of ~ 0.55 .* (B) *log-log plot of the number of clusters (N_c) versus time for deeply quenched decanethiol-ligated nanoparticles with $f = 0.02$. The dotted line yields an exponent of ~ -1 .*

make the minimum of the potential well depth equivalent to $10 kT_{room}$. Results for such a deep quench are shown in Figure 4.19A,B. It is exciting to observe that indeed, irreversible DLCA model results are recovered in the limit of deep potential well depths.

4.5 Conclusion.

In summary, in this chapter, we have used an effective pair potential between two ligated 5 nm gold nanoparticles (detailed description in chapter 2) in a Brownian dynamics simulation to study nucleation of NPSCs from a temperature quenched NP solution. Both the kinetics and morphology of the NPSCs were studied. To study the nucleation phenomenon in the aggregates of NPSC, we divide the dynamics of the growing cluster into two regimes; pre-nucleation regime and nucleation regime. Analysis of a pre-nucleation induction period with classical nucleation theory yielded a supercluster interfacial tension that compare reasonably well with other theory and experimental measurements. We observed that most of the smaller sized pre-nucleating NPSCs have non-compact morphology whereas the larger sized NPSCs are compact, and the growth of the nucleating NPSC is dominated by the addition/subtraction of monomers as postulated by CNT. An unexpected and surprising observation was that the pre-nucleation cluster size can occasionally range greater than the critical size in the pre-nucleation regime without nucleation occurring. Only when a cluster with low enough energy occurs will nucleation ensue.

Next, we study the aggregation at higher volume fractions for both dodecanethiol (C12) and decanethiol (C10) ligated NPs. For the case of C12 NPs, where the depth of the interaction potential between the NPs is 3.1kT, round shaped clusters are found to coexist with the dispersed phase and the cluster morphology is found to be compact at all length scales. The kinetics of cluster growth in this case is compared with phase separations in binary mixtures. For decanethiol-ligated NPs, where the model potential well depth is found to be deeper (- 5.15kT), the aggregating NPSCs at higher volume fraction are found to have hybrid, fractal-like structure. Cluster morphology in this case shows a compact structure at short length scales and a fractal structure at large length scales. The growth kinetics for this deeper potential depth is compared with the diffusion limited cluster-cluster aggregation (DLCA) model.

Chapter 5

Crystalline Structure of the nucleating cluster in Dodecanethiol Ligated Nanoparticles

In chapter 4, we have studied the nucleation of NPSCs in the quenched ligated gold nanoparticle system. During that study, we not only calculated the approximate size of the critical size of the nucleating NPSC but also analyzed the structure of the prenucleating NPSCs in the system. In this chapter, our work will be focused on the dynamics and structure of the stable nucleating cluster (i.e in the *nucleation regime*). We will start our discussion by looking at the morphology of the stable nucleating NPSC at late times in our simulations shown in figure 4.1. Since our NPSC is mostly spherically symmetric throughout this region, we compute the radius of gyration R_g and perimeter radius R_p of the nucleating NPSC by using the relations;

$$R_g = \sqrt{\frac{1}{N} \sum_{i=1}^N (r_i - r_{COM})^2} \quad (5.1a)$$

$$R_p = \sqrt{\frac{5}{3}} R_g \quad (5.1b)$$

where r_{COM} represents the position of the Center of Mass(COM) of the cluster and all the particles residing inside the R_g define the *core* of the NPSC whereas all particles residing outside R_p are considered to form the *surface* of the NPSC. In the following section, we will focus on identifying the structure of the particles in the *core* and the *surface* of the NPSC.

5.1 Radial Distribution Function

To define the neighbors of the particles in the NPSC, we calculate the radial distribution function $g(r)$ for a given size of the NPSC. Physically speaking, the radial distribution function (RDF) describes the variation in the density of the particles as a function of the distance from the reference particle. For detailed description, let us consider a system of N particles. The Probability of finding particle 1 in dr_1 , particle 2 in dr_2 and so on ..., is given by [79]

$$P^N(r_1, \dots, r_N) dr_1 \dots dr_N = \frac{\exp(-\beta U_N) dr_1 dr_2 \dots dr_N}{Z_N} \quad (5.2)$$

where Z_N is the configurational integral. The probability that particle 1 is in dr_1 at r_1, \dots , molecule n in dr_n at r_n , irrespective of the configuration of the remaining $N - n$ is obtained by integrating equation 5.2 over the coordinates of molecules $n + 1$ through N :

$$P^N(r_1, \dots, r_n) = \frac{\int \dots \int \exp(-\beta U_N) dr_{n+1} \dots dr_N}{Z_N} \quad (5.3)$$

Now, if *any* particle 1 is in dr_1 at r_1, \dots , and *any* particle n in dr_n at r_n then the probability is given by

$$\rho^n(r_1, \dots, r_n) = \frac{N!}{(N - n)!} P^N(r_1, \dots, r_n) \quad (5.4)$$

The prefactor comes from the fact that the 1st particle can be chosen in N ways, the 2nd one in $(N - 1)$ ways and so on. So the probability of finding any particle at \vec{r}_1 in $d\vec{r}_1$ for an isotropic fluid is given by

$$\rho^1 = N \frac{\int \dots \int \exp(-\beta U_N) dr_2 \dots dr_N}{Z_N} \quad (5.5)$$

or $\int \rho^1 d\vec{r}_1 = N$. But since ρ^1 is independent of \vec{r}_1 (isotropic fluid) so we can write $\rho^1 = \frac{N}{V} = \rho$. Similarly, it can be shown that for an ideal gas, $\rho^2(\vec{r}_1, \vec{r}_2) \approx \rho^2$. We define the *distribution functions* $g^{(n)}(\vec{r}_1, \vec{r}_2, \dots, \vec{r}_n)$ as $g^{(n)}(\vec{r}_1, \vec{r}_2, \dots, \vec{r}_n) = \frac{1}{\rho^n} \rho^{(n)}(\vec{r}_1, \vec{r}_2, \dots, \vec{r}_n)$. In the

case of spherically symmetric particles of a liquid, we can write $g^2(\vec{r}_1, \vec{r}_2) = g^{(2)}(r) = g(r)$ such that we can write

$$\int \rho^2 g(r) d\vec{r} = \frac{N(N-1)}{V} \quad (5.6a)$$

$$\int \rho g(r) 4\pi r^2 dr \approx N \quad (5.6b)$$

Here $\rho g(r) 4\pi r^2 dr$ is really the number of particles between r and $r + dr$ from the reference particle. This is why, $g(r)$ is called the radial distribution function. We calculate the radial distribution function for our late time cluster with $N_p \sim 10000$. Figure 5.1 shows the RDF of the nucleating NPSC. The sharp peaks of the RDF indicate the presence of the crystalline structure in our nucleating NPSC. The first minima of $g(r)$ correspond to the

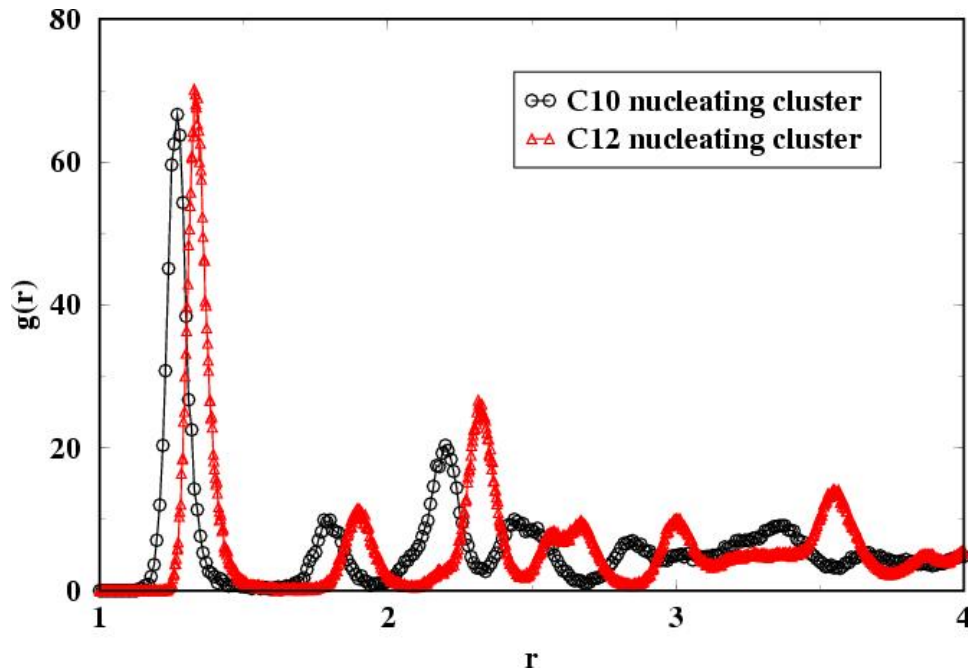


Figure 5.1: A plot of the Radial Distribution Function $g(r)$ as a function of separation between the particles ' r ' for the nucleating NPSC for C12 and C10 ligated gold nanoparticles. The first minima of the radial distribution function $g(r)$ is used to identify the neighbors in a NPSC.

nearest neighbor (NN) distance δ between the particles in the NPSC whereas first maxima

are indicative of the lattice spacing in the NPSC [80]. So, in our analysis, all the particles separated by the NN distance δ are known as the *neighbors* of the particles in the NPSC. Next we calculate the distance of the i th nearest neighbor (NN) of each particle and average over the *core* and *surface* particles separately. This is shown in Fig. 5.2 for NPSCs at early and late times. Since the potential minimum for dodecanethiol ligated system is at $r_{min} = 1.33$ (see figure 3 in Chapter 2) , the first NN is located at this distance. At the latest time, the NPSC core shows 12 NN within a small spread of distance indicating a closed packed crystal structure (fcc or hcp). A subsequent discontinuity in distance indicates the beginning of the

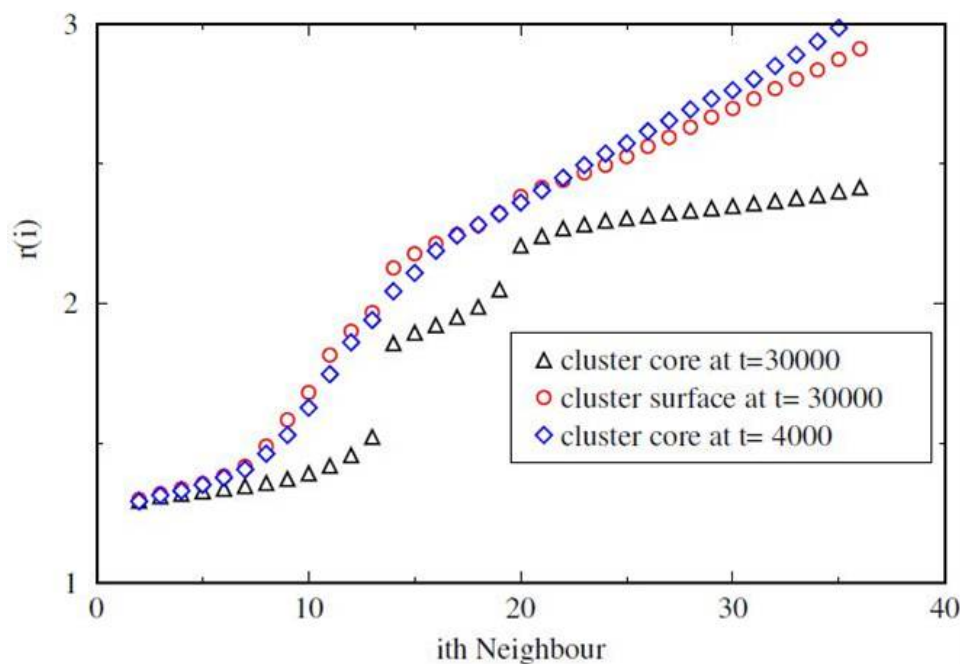


Figure 5.2: Plots for the average distance $r(i)$ of the i th neighbor for the particles in the nucleating cluster at given time for dodecanethiol ligated gold nanoparticles. Early time cluster behaves the same way as the surface of the late time cluster

next NN sequence and six such next NNs follow. Another weak discontinuity comes next and then the sequence of 12 third NNs follows. In contrast, at earlier times, the growing NPSC has only five or six pure NNs at separation $r_{min} = 1.33$ and then a sequence of neighbors whose distance increases continuously. As also shown in Fig. 5.2, this liquidlike morphology of the NPSC at early times is strikingly similar to the surface structure of the NPSC at late

times. To further characterize the crystalline structure of the nucleating NPSC, we analyze the growing NPSC by using the *local bond order parameters* first introduced by Steinhardt *et al* [81] which represents the local orientational symmetry of the neighbors of each particle in the system.

5.2 Bond-orientational order Parameter

During the growth of a nucleating NPSC in our system, a transition may take place from an isotropic *liquidlike* structure to more ordered *solidlike* structure. To distinguish between the structure of the crystalline solids and isotropic liquids, a study of the translational and rotational broken symmetries plays an important role. A "broken" symmetry process is a process which results due to a transition from a disordered state to a more ordered state. Here less ordered state is considered more symmetric in the sense that small variations to it would not have much effect on its overall state. The isotropicnematic phase transition in liquid crystals and the isotropiclamellar phase transition for amphiphiles or block copolymers can be considered as the prominent examples of the symmetry breaking transitions. The orientational anisotropy refers to the "bonds" joining the *neighbors* of the particles rather than the particles themselves and its importance in 3D was first emphasized by Frank [82] in 1952. Here "bonds" meanings are different from the chemical bonds and represent the line joining the *neighbors* of a particle in the NPSC. Local *bond order parameters* can also be used for the accurate identification of the crystalline structure of the NPSCs and are obtained from an algorithm which is based on the spherical harmonics and is given by the quantity;

$$q_{lm}(i) = \frac{1}{N_b(i)} \sum_{j=1}^{N_b(i)} Y_{lm}(\theta(\vec{r}_{ij}), \phi(\vec{r}_{ij})) \quad (5.7)$$

where the $Y_{lm}(\theta, \phi)$ are the spherical harmonics and $\theta(\vec{r})$ and $\phi(\vec{r})$ are the polar angles of the bond measured with respect to some reference coordinate system. Since all the even spherical harmonics are invariant under inversion, we limit our analysis to the even l values.

Here $N_b(i)$ represents the number of neighbors of the i th particle and the sum is taken over all the $N_b(i)$ bonds that the i th particle has with its *neighbors*. Because the $q_{lm}(i)$ for a given l can be scrambled drastically with the variation in the rotation coordinate system, it is important to have a rotationally invariant combination of the coordinates such as;

$$q_l(i) = \sqrt{\frac{4\pi}{2l+1} \sum_{m=-l}^l |q_{lm}(i)|^2} \quad (5.8)$$

and

$$\hat{w}_l(i) = w_i(i) / \left(\sum_{m=-l}^l |q_{lm}(i)|^2 \right)^{3/2} \quad (5.9)$$

where

$$w_l(i) = \sum_{m_1, m_2, m_3, m_1+m_2+m_3=0} \begin{pmatrix} l & l & l \\ m_1 & m_2 & m_3 \end{pmatrix} q_{lm_1}(i) q_{lm_2}(i) q_{lm_3}(i) \quad (5.10)$$

These local order parameters are used to determine the order around particle i . For the case of $l=6$, the vectors add up coherently for the case of *solidlike* particles and hence a larger nonzero global bond order parameter value is obtained for each crystalline structure while in the case of *liquidlike* particle, the vectors add up incoherently such that the bond order parameter value is zero. Table 5.1 shows the different global order parameter values for different structures. From the table 5.1, we can see that the bond order parameter for $l=6$, not only distinguishes between the solidlike and liquidlike structures but also we can differentiate between different crystalline structure [83].

5.3 Crystalline Structure of Dodecanethiol and Decanethiol Ligated System NPSCs

In this section, we look at the morphology of the nucleating NPSC at late times using the bond order parameter algorithm. Our observation is confined to q_6 parameter calculations.

Table 5.1: *Bond Orientational Order Parameter values for different crystalline structures*

structure	Q_4	Q_6	\widehat{W}_4	\widehat{W}_6
fcc	0.191	0.575	-0.159	-0.013
hcp	0.097	0.485	0.134	-0.012
bcc	0.036	0.511	0.159	0.013
sc	0.764	0.354	0.159	0.013
icosahedral	0	0.663	0	-0.17
liquid	0	0	0	0

As an example, q_6 distribution of the pure crystals of fcc, bcc, hcp and Mackay Icosahedral [84] is shown in the figure 5.3. Each structure has its distinct peak such that one can easily differentiate between different crystalline structures. Next, we calculate the q_6 distribution for the late time nucleating NPSC of C12 ligated system and compare it with pure crystals as shown in figure 5.3. Notice the broad distribution of our nucleating NPSC near the fcc and hcp peaks and also that there appears to be no contribution of the pure icosahedral structure. In order to have better understanding in the spread of the nucleating NPSC distribution, we artificially created spread in the distribution of pure fcc, bcc and hcp crystals. This spread is created by randomly displacing the particles in the crystals about their lattice sites. The random displacement of the particles varies differently in different regions of the crystals indicating the different levels of distortions created by the thermal vibrations of the particles in the crystal about their lattice points as described in table 5.2. A plot of q_6 distribution of these randomly displaced crystals along with the nucleating NPSC is shown in fig. 5.4.

The matching of the randomly displaced structures of fcc and hcp with the nucleating NPSC also indicates that there is no indication of the bcc structure in the NPSC. We also observe that the q_6 distribution of the NPSC *core* is analogous to the structure of a mixture of fcc/hcp randomly distorted structure whereas the distribution of the NPSC *surface* at late times (at $t = 40,000$ and N being 10147) overlaps with the initial time *liquid-like* structure of the NPSC (at $t = 4000$ and N being 57). This observation matches well with the analysis

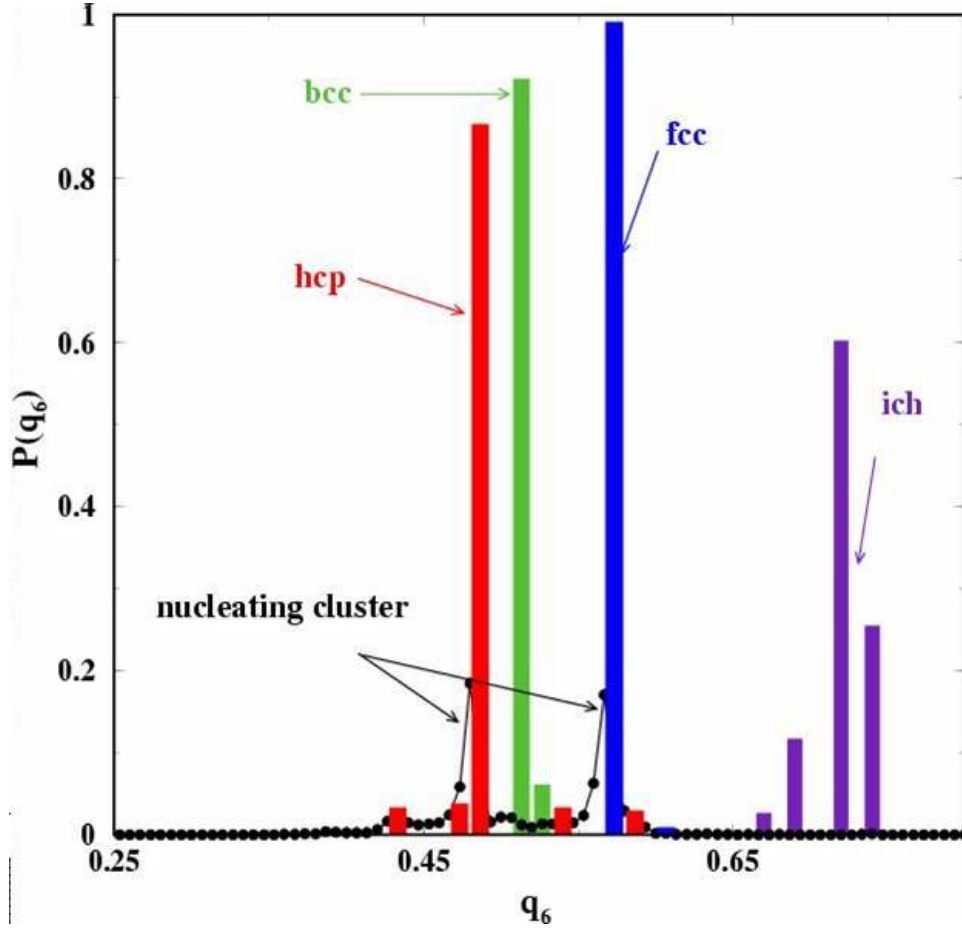


Figure 5.3: q_6 distribution of the pure crystals of hcp, bcc, fcc and icosahedral in comparison with the nucleating cluster at $t = 40,000$ ($n_p = 10147$).

Table 5.2: A table of the random variations in the lattice sites at different shells in the hcp, bcc, fcc and ich crystal lattices

shell	$shell < R_g$	$R_g < shell2 < R_p$	$R_p \leq shell3$
fcc	2%	4%	10%
bcc	2%	4%	10%
hcp	2%	4%	10%
ich	2%	4%	10%

done in 5.1. For the case of C10 ligated system, the crystalline structure of the nucleating NPSC at late times is found analogous to the C12 system NPSC.

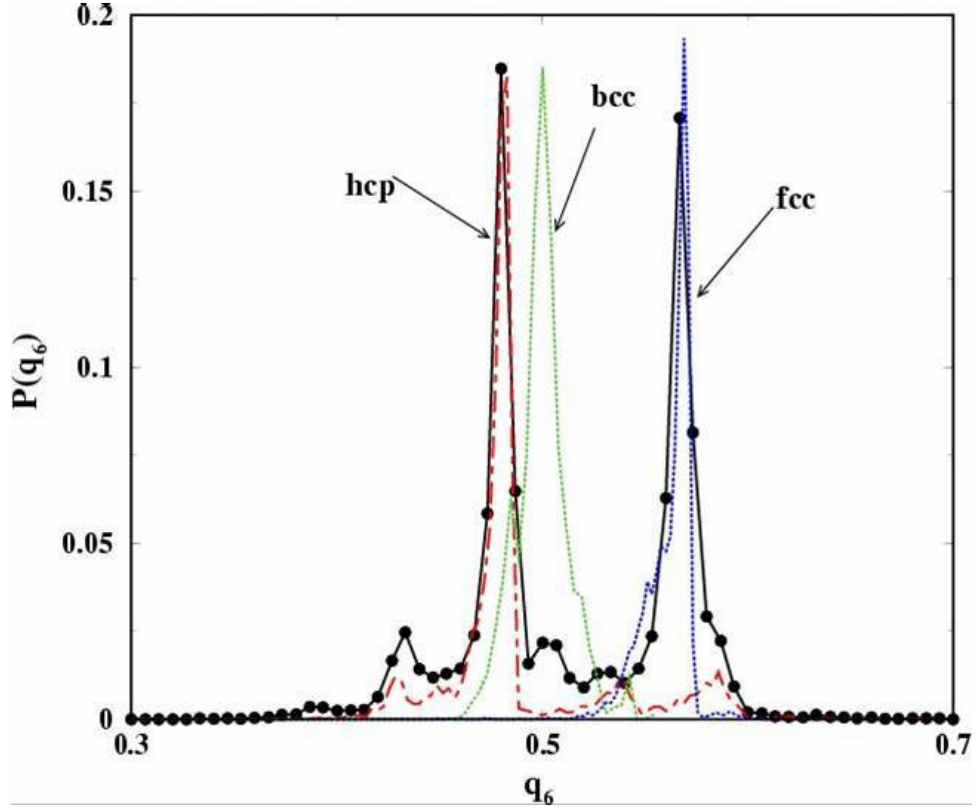


Figure 5.4: A comparison of the nucleating NPSC at $t = 40000$ with the randomly varying crystals of bcc, fcc and hcp. The particles in the pure crystals are given 5% displacement.

5.3.1 Possibility of icosahedral (ich) structure

The Icosahedral structure is another example of the closed packed structure. From figure 5.3, it can easily be perceived that there is no structural contribution of a pure icosahedral structure to our nucleating NPSC. What happens when we randomly displace the particles about their lattice points in a pure icosahedral structure? For that purpose, we created a 14 layered cluster on an icosahedral structure (with $N = 10179$) such that the particles in the cluster are given random distortions about their lattice points as shown in the Table 5.2. Figure 2.5 shows the comparison of the q_6 distribution of this random cluster on icosahedral (ich) lattice with our nucleating NPSC at $t = 40,000$ ($withnp = 10147$). It can be seen that the q_6 distribution of the random cluster on ich lattice overlaps with the distribution of our

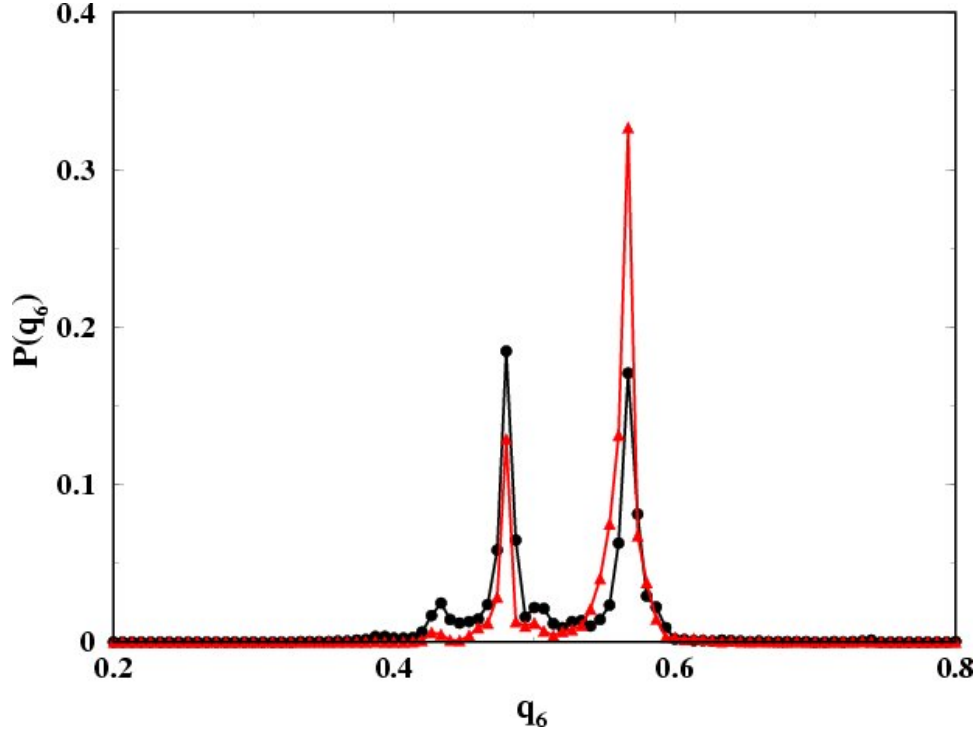


Figure 5.5: q_6 distribution of icosahedral structure (red curve) with randomly distorted regions in comparison with the nucleating NPSC (black curve). The particles in the pure crystals are given 5% displacement.

nucleating NPSC, although the peak positions are not the same in the two cases. In our understanding, the reason of the similarities between fcc, hcp and ich randomly distorted structures lies in the fundamental structural difference of these crystals. In the case of fcc and hcp structures, all *neighbors* are equally spaced while in the case of icosahedral (ich), the *neighbors* on upper and lower layers are separated by d distance while the *neighbors* on the same layer are $1.05d$ distance apart. So, giving a random variation of 5% or more about the lattice sites will remove this spacing difference between the *neighbors* and the structure of the cluster on ich lattice would behave very similar to the cluster on fcc/hcp lattice. To further test the possibility of the presence of an ich structure in our system, we focus on the morphology and energetics of the *inner core* of the nucleating NPSCs in the post-nucleation regime for both C_{12} and C_{10} ligated systems. All particles closest to

the center of mass (COM) are considered as *inner core* particles. To study the energetics of the *inner core* particles, we select first 13, 55 and 147 particles nearest to the COM of NPSC. Next, we created a system of same number of particles on a fcc, hcp and ich lattices using our nanoparticle interaction model potential in chapter 2. Although energy per particle calculation favors fcc/hcp structures for each of the special sized 13, 55 and 147 (icosahedral magic numbers) [84] N clusters, the actual NPSCs of these sizes seen during time evolution show a distinct tendency (see Fig. 5.6) toward icosahedral (ich) morphology for the C_{10} system. The C_{12} clusters of these special sizes are, on the other hand, non-crystalline because no ordered structure was found in these special size clusters for C_{12} system.

Although few crystalline particles can be seen in the *inner core* of $N = 147$ but overall it behaves as *liquidlike*. To gain a better understanding on the evolution of the NPSC morphology, we then looked at the *inner core* of a 2000 particle NPSC during its growth dynamics. In both systems (*i.e.* C_{12} and C_{10}), we observe that both systems have ich morphology in the *inner core* as shown in fig. 5.6. For the C_{10} ligated case, as the system is deeply quenched in comparison of the C_{12} system such that thermal fluctuations have little effect on the formation of small size clusters and hence more stable crystalline structures are observed. On the other hand, C_{12} system is shallower and the smaller size NPSCs are unstable leading to the formation of loosely bound structures. But as the nucleating NPSC size grows, the *inner core* of the NPSCs starts getting thermally stable and ordered structures also start appearing in the *inner core* of the C_{12} NPSCs as shown in fig. 5.6. From this observation, it can be concluded that the randomly distorted icosahedral (ich) and other closely packed crystals (hcp and fcc) have similar crystalline structure although *inner core* analysis shows that energetically ich structure is more favorable for these stable nucleating NPSCs. Another way of looking at the crystalline structure of the nucleating NPSC is to observe the scatter plot of the NPSC in the $q_4 - q_6$ and $q_4 - w_4$ planes and has been used before [85], [86]. The graph of $q_4 - q_6$ and $q_4 - w_4$ planes in figure 5.7 shows the

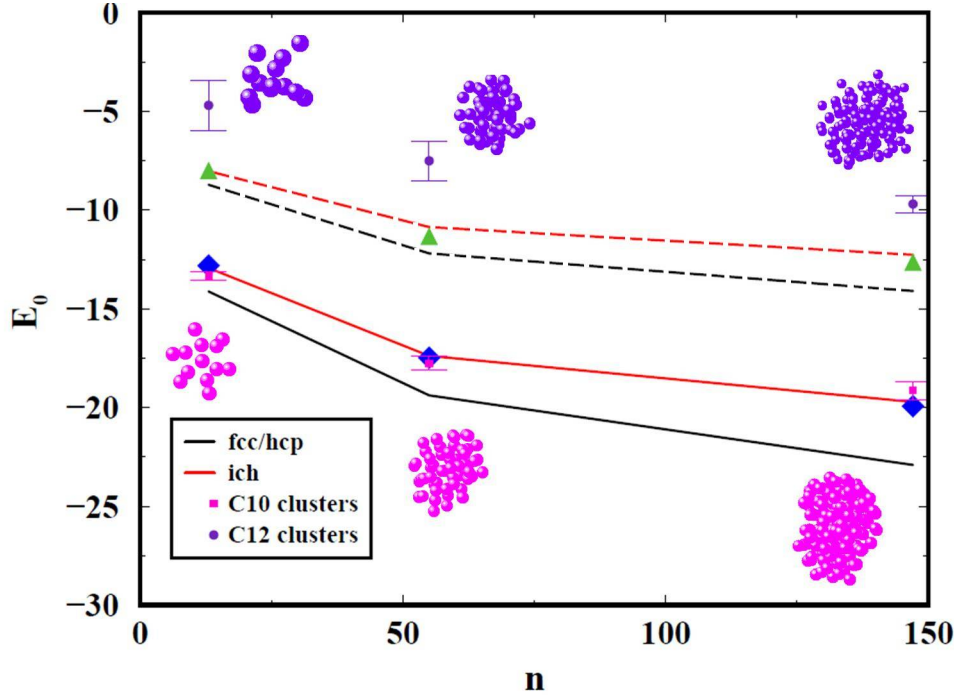


Figure 5.6: A plot of the energetic comparison of the nucleating NPSCs for C_{12} and C_{10} ligated nanoparticles with the energetically stable clusters on the ich, fcc and hcp lattices. The solid line represent the C_{10} clusters of size 13,55 and 147 on the fcc/hcp and ich lattices whereas the dashed lines correspond to the respective size clusters for the C_{12} case. The squares and the circles represent the C_{10} and C_{12} NPSCs in the simulations. The C_{10} NPSCs overlap with the ich clusters whereas C_{12} NPSCs energetically show no evidence of crystalline structure. The core clusters of respective size of the C_{10} and C_{12} late time NPSCs of size 2000 also show that the core of the nucleating growing NPSCs in both cases behaves like ich.

scatter plot for the structure of the C_{12} ligated nanoparticles in comparison with randomly distorted crystalline structures.

The Fig. 5.7 shows the $q_4 - q_6$ 2D plane plot of the nucleating NPSC in comparison with the randomly distorted fcc, and hcp crystals. From these plots, one can clearly identify and distinguish the patchy regions of different crystalline structures. The data points of the nucleating NPSC in this $q_4 - q_6$ plane plot appears to be overlapping with the random crystals in some regions of the plane but still there are few areas which can not be explained with these random crystal structures. Same nucleating NPSC is then overlapped with randomly

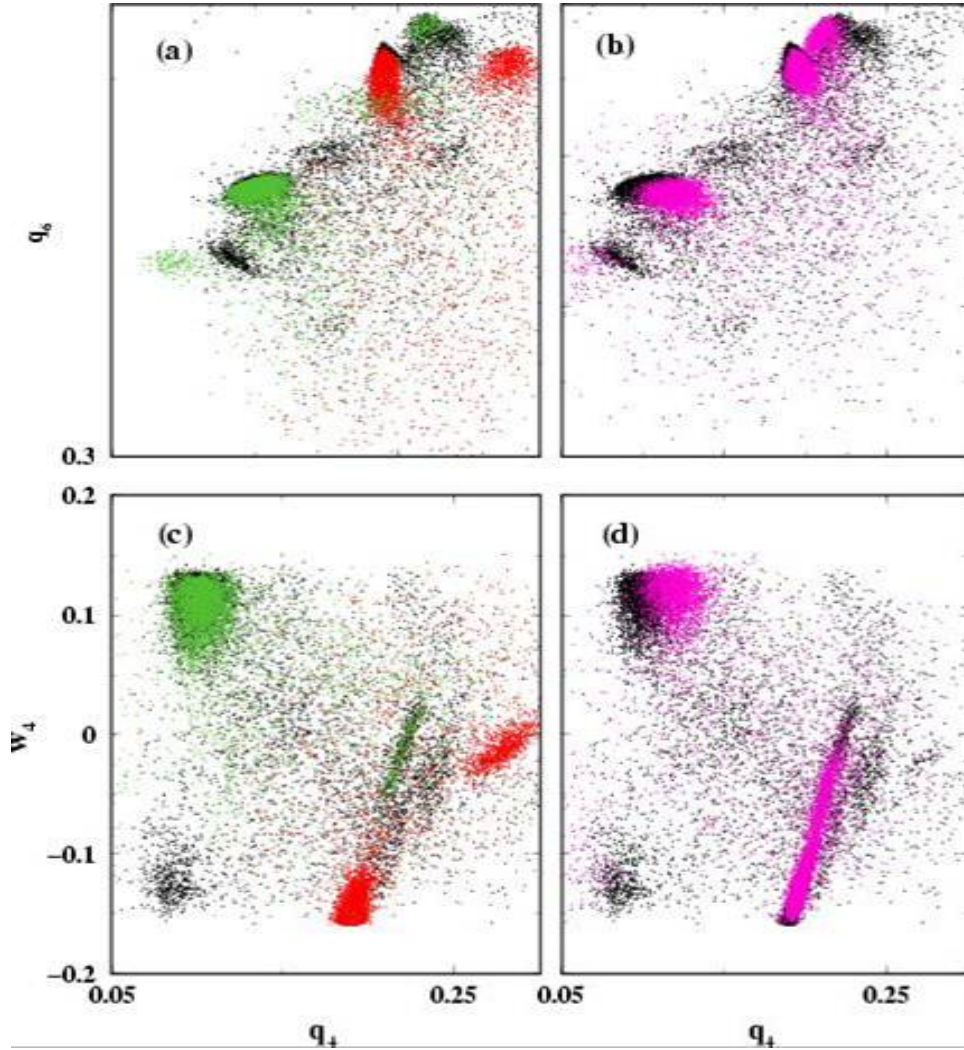


Figure 5.7: The $q_4 - q_6$ plane plot (a) showing the comparison between the nucleating NPSC (black) and the randomly distorted fcc and hcp crystals (red and green respectively) and (b) between the nucleating cluster (black) and the randomly distorted icosahedral structure (magenta color). Comparing (a) and (b), one finds that there is a huge overlap between fcc, hcp and icosahedral structures. Similarly, $q_4 - w_4$ plane plots of the respective structures are shown in fig. 19(c) and (d). Surprisingly, no fcc overlap with icosahedral is observed from this comparison of $q_4 - w_4$ plot.

distorted icosahedral structure of 14 layers (as the number of particles in the nucleating NPSC ($np = 10147$) is nearly same as the 14 layered icosahedral structure ($np = 10179$)) as shown in fig. 5.7(b). From fig. 5.7(b), we can see that the patches created by the randomly distorted icosahedral structure overlaps with the nucleating NPSC in the crystalline regions

of the scatter plot and also it overlaps with both fcc and hcp distorted crystals. Similarly, figs. 5.7(c) and (d) show the comparison of the hcp, fcc and icosahedral structures and the nucleating NPSC in the $q_4 - w_4$ plane plots. From fig. 5.7(c) and (d), it can also be noted that the crystalline structures of fcc and hcp can better be distinguished as compared to $q_4 - q_6$ plane plots as the patchy regions indicating these both crystalline structures are well separated out in the planes. Although these plots are helpful to distinguish between fcc and hcp structures but still the overlap between the hcp, fcc crystalline structures and icosahedral can not be separated out and it becomes difficult to determine the exact structure of the nucleating cluster based on these bond order parameter analysis. Lechner and Dellago [85] introduced another method based on averaged local bond order parameters to determine the crystalline structure. According to their improved method, the information of the structure is not restricted to the neighboring shell of each particle (as is in the case of the conventional local order parameter) but the second shell is also included in the analysis. Our analysis based on this method does not show any improvement in the structure identification.

5.3.2 Evaluation of Crystalline Fraction

To further look at the details of the cluster morphology and to differentiate between the *liquid-like* and *solid-like* particles, we make use of the scalar product definition of the vector q_6 for the i th particle with the *neighboring* j particles which is given by;

$$c_{ij} = q_6(i) \cdot q_6(j)^* = \sum_{m=-l}^l \tilde{q}_{lm}(i) \cdot \tilde{q}_{lm}(j)^* \quad (5.11)$$

This vector product between the neighboring particles helps to distinguish between the *solid-like* and *liquid-like* particles in the whole NPSC. First, we define the *connected* neighbors. Two neighbors are considered to be *connected* if the above mentioned correlation function is greater than a threshold value of 0.5 as described in [87]. In order to indicate the threshold for the choice of connected particles, all the particles with value of 0.5 or more are considered *connected* particles. For distinction between *solid-like* and *liquid-like* particles, we set the threshold value of more than 6 connections per particles as mentioned by Frenkel [87].

All the particles having more than 6 connections are considered as solid-like particles and otherwise they are considered as *liquid-like*. In literature, different definitions have been used to distinguish between the *solid-like* and *liquid-like* particles. For example, Eduardo Mendez-Villuendas and Bowles [88] have used a threshold value of 0.65 of C_{ij} instead of 0.5 as used by ten Wolde et al [87] for definition of the *connected* particles and also their method to identify the *liquid-like* and *solid-like* particles is different. In our observation, both of these definitions give more or less same result for the distinction between the liquid-like and solid-like particles in our analysis of the nucleating cluster. Now, to further identify the crystalline structure in the solid-like particles, we use the method described in Ref. [89]. This method is based on the values of $w_6(i)$ and $q_4(i)$. According to their definition, if $w_6(i) \leq 0$ and $q_4(i) \geq 0.15$ then the structure of the i th *solid-like* particle is considered as FCC structure and if $q_4(i) \leq 0.15$ and $w_6(i) \geq 0$ then the structure is considered as HCP. Furthermore, based on scatter plots in fig. 5.7, we find that there are some dense regions (representing crystalline structures) which are different from any of the described structures. These supplementary structural regions are categorized as unknown structures. So, based on above mentioned definition for the identification of the crystalline structure, we looked at the morphology of the nucleating cluster at four different times of the growing cluster in our simulation. The morphology is shown in fig. 5.8. It can be seen in fig. 5.8(a) that at initial times, the particles in the nucleating NPSC behaves as liquid-like particles and all different crystalline structures start to appear simultaneously in the NPSC once it achieves a certain size (around 150 particles in this case) and as the NPSC grows, the core becomes more and more crystalline while its *surface* is more liquidlike as shown in fig. 5.8(b)-(d). From this analysis, it has been observed that the formation of a stable nucleating NPSC is a two step process. The nucleating embryo is initially *liquidlike* and then in the second step, fcc/hcp crystalline structure start to evolve alongside other unknown structure in the stable nucleus simultaneously and ultimately different layers of crystalline structure are formed. Another important conclusion can be drawn from our analysis that the surface of the nucleating cluster is always dominated by

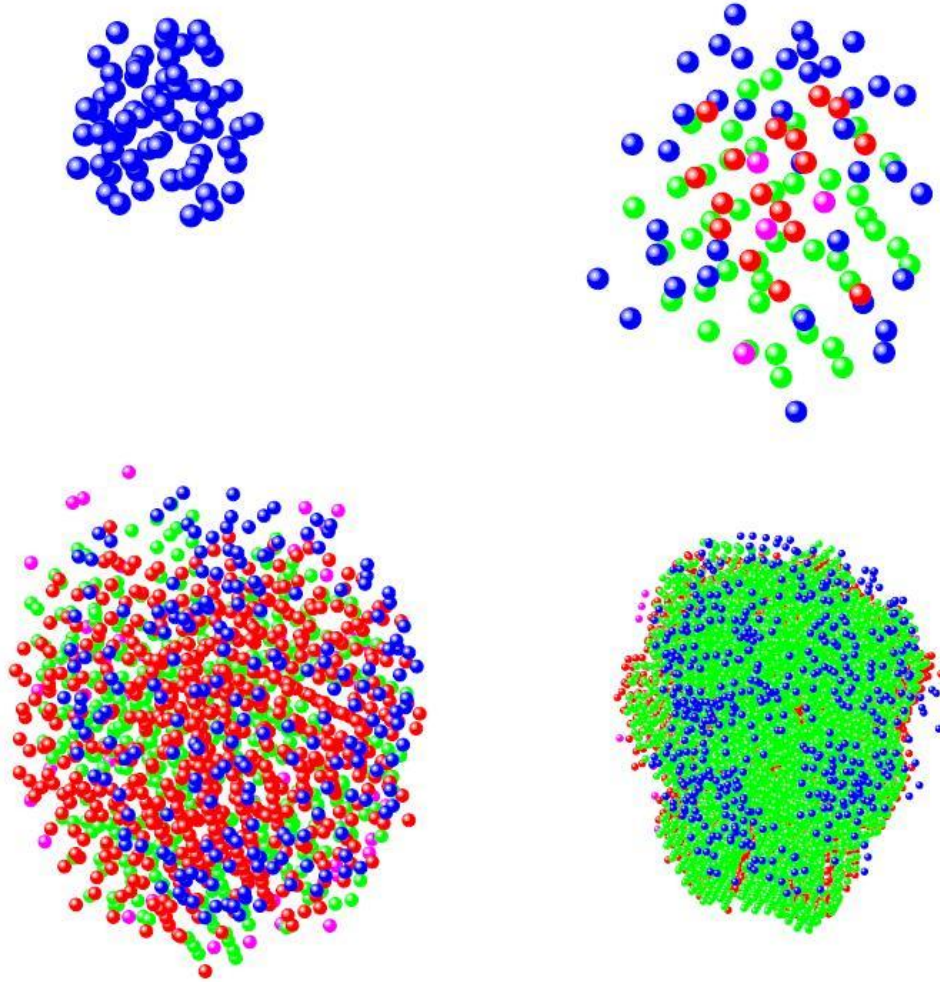


Figure 5.8: *The morphology of the nucleating cluster in the C_{12} system showing the presence of liquid structure and different crystalline structures at a) $t = 3000$ ($np = 147$), b) $t = 5000$ ($np = 1296$), c) $t = 10,000$ ($np = 5346$) and d) $t = 40,000$ ($np = 10147$). The blue color indicates the liquid-like particles in the cluster, green indicates the hcp structure, red color is indicative of the presence of fcc and unknown structure in the system is shown in the pink color.*

the *liquid-like* particles. Similar observation was found by van Meel et al during their study of the LJ system below triple point [90].

Another view of looking at the crystalline structure of the nucleating cluster is to see the fractional composition of different crystalline structures existing in the cluster. Figure 5.9 shows the structural composition of the nucleating NPSC as a function of the time for C_{12}

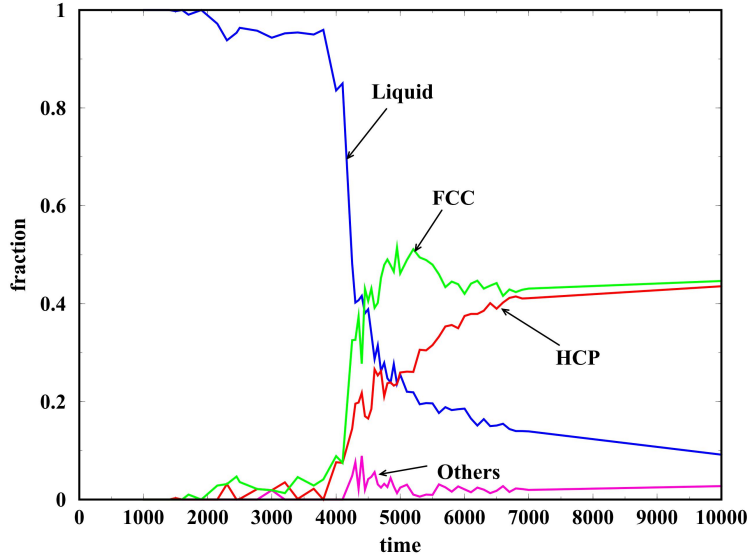


Figure 5.9: A plot showing the variation and growth of the different crystalline structure in a nucleating cluster as a function of time. At initial times, when the size of the nucleating cluster is small, the structure is dominated by liquidlike structure but as the size increases, different crystalline structures start to dominate

ligated system. It can be seen from the figure that the initial time NPSC is dominantly liquid-like in structure but it grows in size, crystalline structures start appearing at its core. Also, by looking at the fractional composition as a function of the distance from COM suggests that even though, crystalline structures do constitute the core of the NPSC, the surface is always dominated by the liquid-like particles.

5.4 Conclusion.

In this chapter, we gave a detailed structural description of the nucleating NPSC . Our analysis is based on the bond orientational order parameter and for the case of C12 ligated system, we observed that the formation of the stable nucleating cluster is a two step process.

Initially, a stable liquid-like structure is formed leading to the formation of different crystalline structures growing in the core of the cluster. Even though the crystalline structure is found to be dominant in the *core*, the *surface* of the growing NPSC is always found to be liquid-like. Also, the crystalline structures in the NPSC are found to be similar to the distorted close-packed crystalline structures of fcc and hcp crystals. A comparison of the crystalline structures between large size (more than 2000 particles in the cluster) stable C10 and C12 nucleating NPSCs shows that the nucleating NPSCs in both cases have same crystalline fraction. But, in the case of small size clusters (as an example, we used $N=13$), C10 being deeper quench, appears to have more crystalline order as compared to C12 system.

Chapter 6

Self-Assembly in a model of short-range attractive colloids

Self-Assembly of the interacting colloidal systems results in the phase transition between gas, liquid and solid states [91]. The liquid phase can be amorphous or liquid crystalline and the solid phases can be crystalline, amorphous (often fractal), and gel. The possibilities of formation of certain structures are related to the details of the potential between the disperse components of the structure. For the case of hard sphere interactions, a fluid to crystal transition occurs whereas an addition of attractive potential brings the possibility of an equilibrium between different phases. One important parameter that affects larger changes in the phase diagram is the relative range of the attractive interaction between the colloidal particles. For short-range attractive potentials, the system develops a gas-crystalline coexistence with a metastable liquid-liquid coexistence region. The presence of such a metastable liquid-liquid coexistence region affects the kinetics of nucleation and growth of clusters in colloidal and protein solutions [24]. In addition, kinetics of cluster growth in colloidal systems with short-range attractions [92] has striking similarity with other phase changes such as spinodal decomposition in binary mixtures of molecular systems [72] and the formation of precipitated crystalline solids from solutions [93]. Thus, colloidal systems are of fundamental interest for a detailed understanding of how a dispersed phase, such as particles in a colloid or molecules in a solution, comes together when destabilized and forms a con-

densified phase such as aggregates, gels, or crystalline solids. Parts of this grand problem have seen considerable previous research such as irreversible aggregation and the formation of fractal aggregates, [94] gelation, spinodal decomposition, [72] nucleation, and early studies of growth during precipitation. [93] However, a general theory that encompasses all these related phenomena is lacking.

Phase behavior of short-range attractive colloids has been studied extensively both theoretically and experimentally. The equilibrium behavior of these systems being reasonably well understood, recent attention has been directed to the understanding of kinetics of phase transitions and colloidal gelation [95] and its relation to glass transition and the more general jamming transition [96], [97]. Hobbie [98] studied the growth kinetics of the crystallization process in depletion driven colloids and compared experimental results with mean-field theories of aggregation-fragmentation [99]. Direct observation of crystallization and aggregation, on one hand, and sublimation of these crystals, on the other, has been carried out by de Hoog et al [100] and more recently by Savage et al [101] by varying the depth of the depletion potential. Arrested spinodal decomposition and the formation of *solidlike* network in colloids and protein solutions were studied by several groups [102], [103], [104]. A recent work by Lu et al. [102] suggested that gelation in short-range attractive colloids starts from density fluctuations (en route to spinodal decomposition) that get dynamically arrested. Computer simulations have also been carried out to study transient gel formation and crystallization in these systems. Evidence of metastability, homogeneous nucleation, kinetically arrested gel state, and density instability was reported in various simulations [102], [105]–[106]. In addition, simulations strongly suggest that kinetic behaviors in short-range attractive colloids [102] do not depend on microscopic details but generally apply to any particle system with short-range attractions. [107]

In this chapter, we present results from extensive Brownian dynamics (BD) simulations (details in chapter 3) for a system of colloidal particles interacting via a short-range and relatively long-range attractive potential. To demonstrate our general results with a specific

example, we consider the AsakuraOosawaVrij (AOV) model of depletion interaction [34], [33] which approximately accounts for the interaction between a pair of colloidal particles by an effective two-body interaction. We focus on lower monomer concentrations and study the nucleation, kinetics, morphology and structure of clusters growing in the large-scale three-dimensional simulations. In the context of recent experiments by Lu et al. [102] mentioned above, how the cluster growth kinetics changes as one increases the volume fraction and the depth of the potential well will be of particular interest. This is studied in our large scale simulations. Clusters obtained in the simulations range from dense faceted crystals to fractal aggregates which show ramified morphology on large scales but close-packed crystalline morphology on short length scales. For low volume fractions, the morphology and crystal structure of a nucleating cluster are studied at various times after the quench. Also, we estimated the critical size of the nucleating cluster based on the fact that most energetic clusters would grow out to form a stable nucleating cluster. We also observed some ordered structure arising in the nucleating clusters. Although, the nucleating cluster seem to grow some ordered structure in their core, the overall structures are quite liquid-like at early times. As the volume fraction of the colloids is increased, growth of clusters is controlled by cluster diffusion and cluster-cluster interactions. For shallower quenches and low volume fractions, clusters are compact and the growth-law exponent agrees well with theoretical predictions [70], [108] and with recent experimental results [102]. As the volume fraction is increased, clusters do not coalesce when they meet each other and the kinetics crosses over to the diffusion-limited cluster-cluster aggregation [109] (DLCA) limit. For deeper quenches, clusters are fractals even at low volume fractions and the growth kinetics asymptotically reaches the irreversible case, namely, the DLCA. Fractal clusters observed in our simulations have a hybrid structure [76], [74] with a closed-packed crystalline ordering at short length scales and a ramified morphology at larger length scales.

6.1 Interaction Model Potential and Simulation Parameters

In our BD simulations [49] (discussed in chapter 3), we consider three-dimensional systems of sizes $L = 128d$ in units of monomer diameter d . All other length scales are measured in units of d as well. We consider a wide range of monomer volume fractions from $f = 0.0001$ to 0.02, with the number of monomers ranging up to $N_m = 84000$. The potential U acting upon each colloidal particle has a twofold contribution: the two-body depletion potential of AOV (U_{AO}) plus a repulsive hard-core-like interaction (U_{hc}) given by the following expressions;

$$U(r_{ij}) = U_{AO}(r_{ij}) + U_{hc}(r_{ij}) \quad (6.1)$$

where $U_{AO}(r_{ij})$ represents the depletion interaction potential and $U_{hc}(r_{ij})$ represents the hardcore potential. The depletion interaction is attractive in nature and arises whenever the solution contains, in addition to suspended colloidal particles, other particles of intermediate size (most commonly polymers are used which do not adsorb on the suspended particles) as compared to the size of the colloidal particles and solvent molecules. The depletion interaction arises due to the osmotic pressure when the polymer molecules are excluded from the *depletion zone* between the colloidal particles as they approach each other. Mathematically, the depletion interaction is given by;

$$\begin{aligned} \frac{U_{AO}(r_{ij})}{kT} &= \phi_p \left(\frac{1+\zeta}{\zeta}\right)^3 \left[\frac{3r_{ij}}{2(1+\zeta)} - \frac{1}{2} \left(\frac{r_{ij}}{1+\zeta}\right)^3 - 1 \right] \text{ for } r_{ij} < 1 + \zeta \\ &= 0 \text{ for } r_{ij} > 1 + \zeta \end{aligned} \quad (6.2)$$

where ζ is the size ratio between a polymer coil (R_g of the coil) and a colloidal particle which controls the range of the depletion interaction in the AOV model and ϕ_p is the polymer volume fraction which controls the strength of the interaction. Most of our simulations are for $\zeta = 0.03$ and 0.1, while some simulations have also been carried out for $\zeta = 0.06$. For the nucleation studies purpose, our simulation is done for $\zeta = 0.05$ and $\zeta = 0.3$ and we consider a monomer volume fractions of $f = 0.003$ with number of monomer N_m equal to

12000 for $\zeta = 0.05$ and potential depth of $U_{min} = 4kT$. At $10kT$, the volume fraction is set at $f = 0.000017$ with $N_m = 1500$ and $L = 360d$. For the case of $\zeta = 0.3$, monomer volume fraction is chosen to be $f = 0.00364$ and $N_m = 14680$ at $U_{min} = 3kT$ whereas at $U_{min} = 10kT$, we set $f = 0.0004$, $N_m = 1750$ and $L = 128d$. For the case of $\zeta = 0.8$, volume fraction is set to be $f = 0.000186$ and $N_m = 6000$ at $U_{min} = 4kT$ with $L = 256d$. In the hardcore-like repulsive interaction given by Eq. 6.3 as;

$$\frac{U_{hc}(r_{ij})}{kT} = r_{ij}^{-\alpha} \quad (6.3)$$

where we have set $\alpha = 36$. Exponents $\alpha \geq 36$ are reported to lead to anomalies when a hardcore mimic is required in the potential [105], [110]. The total pair potential $U = U_{AO} + U_{hc}$ passes through a minimum value (U_{min}) that depends on ζ and ϕ_p . In what follows, we will often characterize the strength of the potential in terms of the absolute value of the minimum potential depth, $Um = |U_{min}|$. In the simulation parameters, we choose $\Gamma = 0.5$ and time step $\Delta t = 0.005$ in reduced time units of $\sigma(m/kT)^{1/2}$ with $m=1$. For this choice of Γ , particle motion is purely diffusive for $t \gg 1/\Gamma$, i.e., $t \gg 2$ in our units. Periodic boundary conditions are enforced to minimize wall effects. All simulations start from a random initial monomer conformation and the results for the kinetics are averaged over several (five to ten) runs whereas for nucleation, the results are averaged over 100 runs.

6.2 Nucleation and Crystalline Structures for short-ranged shallow quenches

To study the nucleation process in the bulk of our quenched system at finite temperature, the largest cluster of size N plays an important role in understanding the behavior and growth of the nucleating cluster. So our analysis is based on the dynamics of the largest cluster in the bulk. To study the effect of range of interaction on nucleation process, we perform our simulation at two different ranges, r_c , i.e. $1.05d$, and $1.3d$, where d is the diameter of the particles and the depth of the potential well is set to be $4k_B T$ and the volume fraction, f , is

tuned such that only one or few small clusters grow in the quenched systems at all ranges. To have better comprehension of the nucleation phenomenon, we made 100 different runs for both ranges at correspondingly different volume fractions. In these simulation runs, we show that the largest cluster in the system grows in two ways. In Type-1, frequent excursions in size take place in the prenucleation regime (it is the time domain in which the largest cluster is unstable) whereas in Type-2, there are no huge size fluctuations in the prenucleation regime and the cluster smoothly enters the nucleation regime (the time domain in which a stable growing cluster is formed) without many hiccups. We also observe that Type-1 dynamics of the largest cluster happen more frequently (60% of the total number of runs) as compared to Type-2 dynamics. Fig. 6.1 shows the size fluctuations of the largest cluster formed in both types of nucleation processes during the simulation for the case of range of 1.05d.

In both cases, such fluctuations were observed although, for the case of long-range systems of $r_c = 1.3d$, the size variations are not large at well depth (maximum excursion up to $N = 10$). Thus, it becomes difficult to do the analysis for such small size clusters. So, for better understanding of these size fluctuations, we study the nucleation mechanism at 3kT for the case of $r_c = 1.3d$ where we observe the size variations up to $N = 40$. To further investigate such complex dynamics, we compared the morphology and structure of the prenucleating and nucleating regime clusters by comparing the radius of gyration R_g and cluster shape anisotropy (A_{13}) variations with size for both regimes. The radius of gyration (R_g) and cluster shape anisotropy (A_{13}) calculations done for the pre-nucleating and nucleation regime clusters are shown in fig. 6.2. As it can be seen from figs. 6.2(a&b) that radius of gyration (R_g) calculations give us the indication of compact structure (*i.e.* $N \sim R_g^3$) of both pre-nucleation regime and nucleation regime clusters in both short-ranges and relatively long-ranged systems. Also, from the cluster shape anisotropy studies (ratio of the major and minor axes eigenvalues of the moment of inertia tensor) [16] shown in figs. 6.2(c&d) for both ranges, it can be established that both prenucleating and nucleating regime clusters

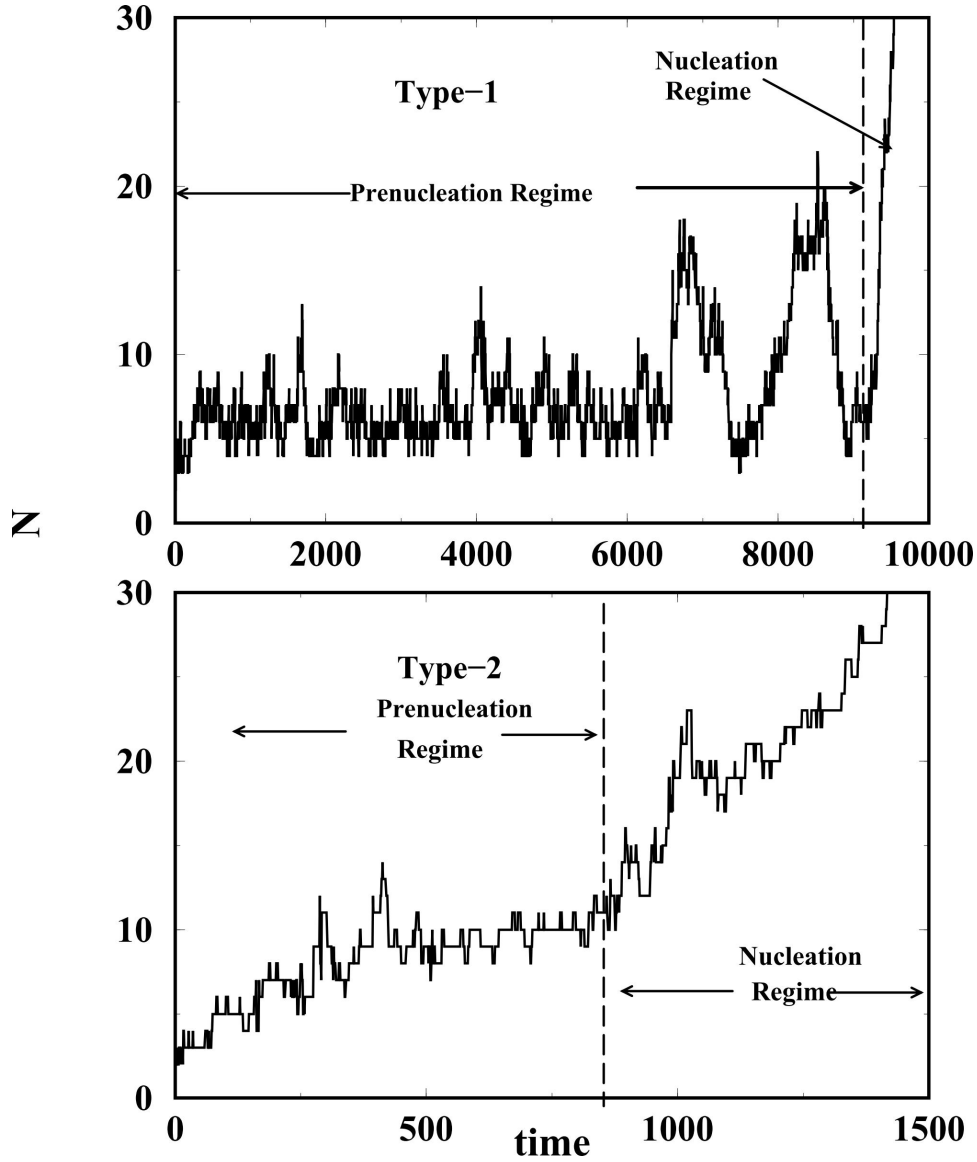


Figure 6.1: A plot showing two different types of size fluctuations during the dynamics of the largest cluster in the system. Type 1 shows the excursions above the critical size in the prenucleating regime whereas in Type 2, no such excursions are seen. Rather a nucleating cluster is seen to grow monotonically to a stable size in this type of nucleation.

have identical shape morphology though the larger error bars for the pre-nucleation regime clusters suggest the shape fluctuations of these clusters.

Next, we calculate and compared the averaged potential energy $\langle E \rangle$ per particle of the clusters in both prenucleating and nucleating regimes.

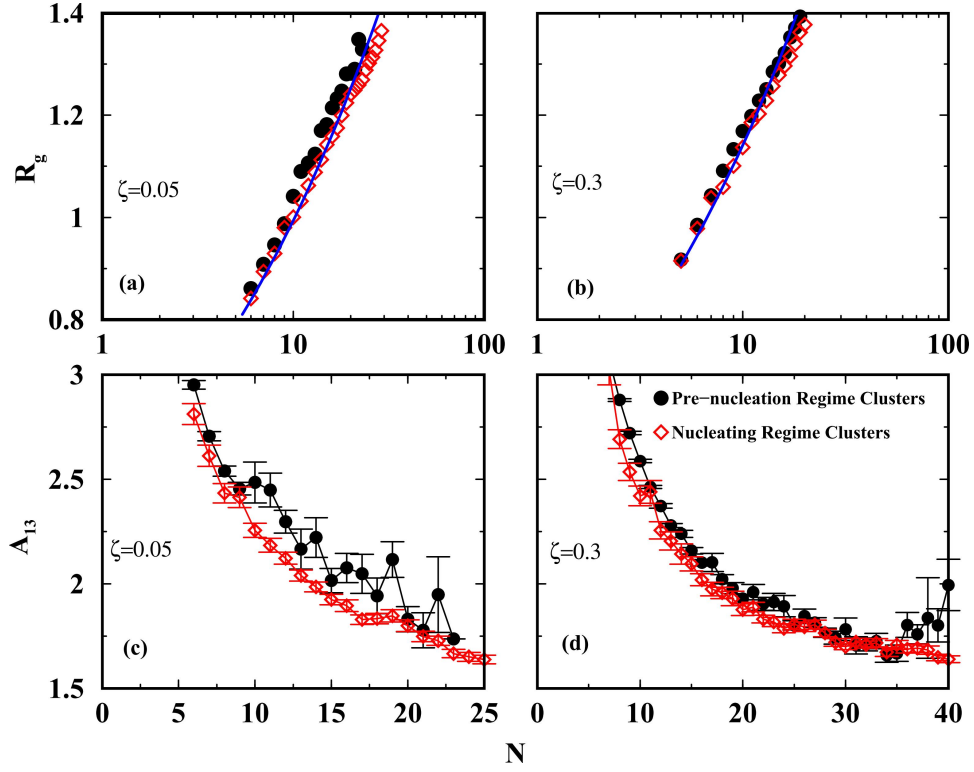


Figure 6.2: A plot showing the variation of the radius of gyration (R_g) and shape anisotropy (A_{13}) as a function of the size (N) for both ranges of $\zeta = 0.05$ and 0.3 . Figs. 6.2(a&b) show the variation of the R_g indicating a compact morphology of the clusters in both cases. Figs. 6.2(c&d) describe the variation of the shape anisotropy parameter A_{13} as a function of the size indicating that the clusters in both regimes have identical shape although bigger error bars for the pre-nucleation regime indicate the shape fluctuations of these clusters

The comparison is shown in figure 6.3 suggesting the fact that, in the case of short range interaction (*i.e.* $r_c = 1.05d$), the nucleating regime clusters have higher $\langle E \rangle$ values as compared to pre-nucleating regime clusters for size $N \geq 10$. It indicates that the nucleating regime clusters of size $N \geq 10$ are more stable energetically as compared to pre-nucleating clusters of the same size while the smaller size clusters seem energetically identical. The bifurcation in energies also gives an indication of the critical size of the nucleating cluster. Similarly, for the case of relatively long range interaction (*i.e.* $r_c = 1.3d$), this division in energies between pre-nucleation and nucleation regime clusters start appearing at $N \sim 16$ and the nucleating regime clusters are always seem energetically more stable.

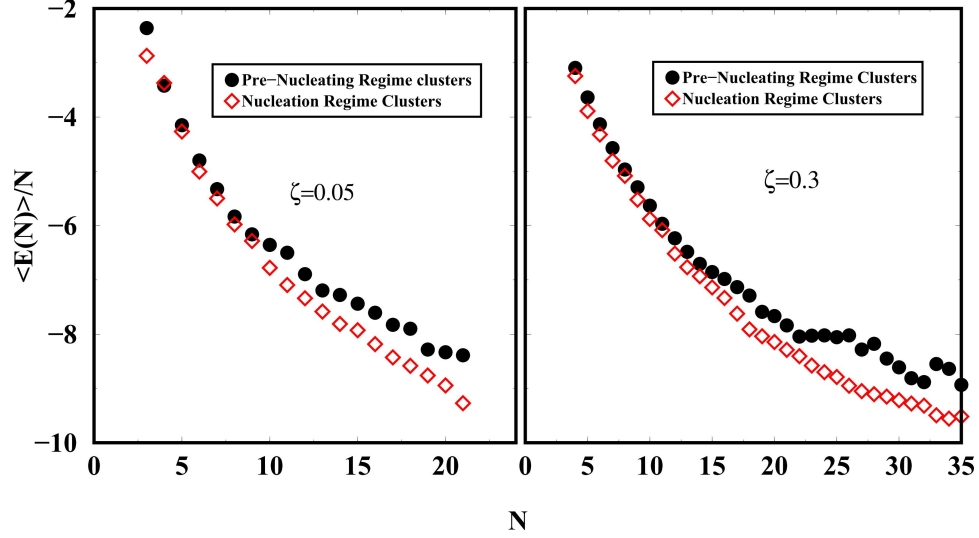


Figure 6.3: A plot for the comparison of the potential energy per particle $\langle E \rangle$ as a function of the size for both prenucleating and nucleation regime clusters. The bifurcation in energy takes place at $N = 10$ and 16 for $\zeta = 0.05$ and 0.3 respectively indicating that the nucleating clusters are energetically more stable as compared to the prenucleating regime clusters once they are above those sizes.

So far, we have been able to establish the fact that, in the case of short range attractive colloidal system, the clusters in nucleating regime are energetically more stable as compared to the clusters in prenucleating regime even though they are equally compact and isotropic. We further probe the problem of nucleation mechanism by looking at the inner structure of these clusters in more details. One important parameter leading to nucleation process is the crystallization mechanism. To study the crystallization process, we used the scalar product $q_6(i) \cdot q_6(j)$ parameters derived from the Steinhardt bond order parameters [81].

If this scalar product for any two neighboring particles is greater than a threshold value of 0.7 , the particles are regarded as the connected and a particle with more than 8 connections is known as crystalline particle. Since the number of crystalline particles N_c fluctuate with time in both prenucleating and nucleating regimes, we calculate the average number of crystalline particles $\langle N_c \rangle$ in a given size cluster for both regime. A comparison of the $\langle N_c \rangle$ between the regions is shown in figure 6.4. It can be seen from the figure that

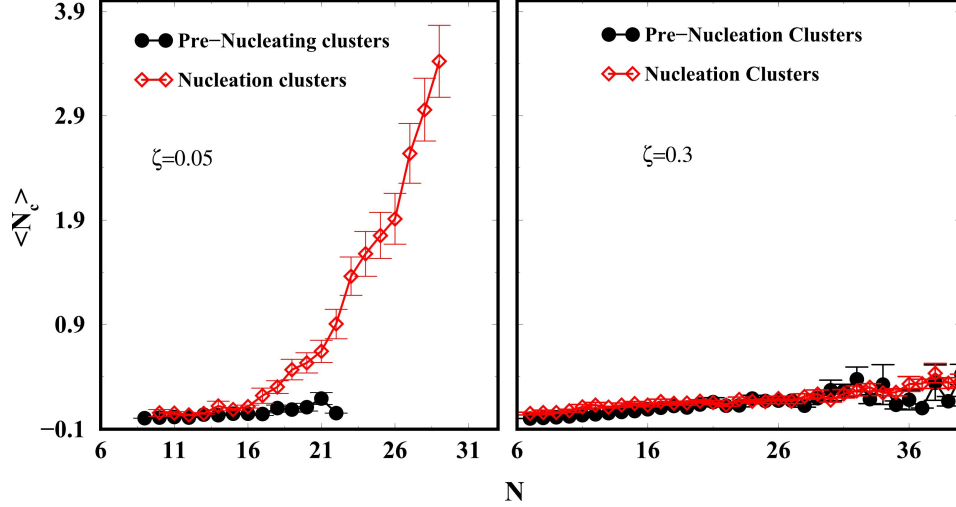


Figure 6.4: A plot showing the variation in the number of crystalline particles N_c (averaged over 100 runs) as a function of the cluster size N for both nucleating and prenucleating regime clusters. The averaged number of crystalline particles $\langle N_c \rangle$, remain almost zero up to size zero in both regimes. The y-axis is shown to have the same values in both graphs to emphasize the presence of no crystalline structure for $r_c = 1.3d$. A significant rise in $\langle N_c \rangle$ is observed in nucleating regime for $N \geq 14$ indicating the importance of the crystalline particles in the nucleation process.

for the short range system of $r_c = 1.05d$, the clusters in prenucleating regime have no or very small number of crystalline particles while, in the nucleation regime, the clusters have significant rise in the $\langle N_c \rangle$ once their size is more than 13 indicating that the ordered structure plays an important role in the formation of stable nucleating cluster. On the other hand, for the case when $r_c = 1.3d$, on presence of crystalline structure is observed. The y-axes of both graphs in figure 6.4 are kept at the same scale to emphasize the absence of crystalline structure in $r_c = 1.3d$ system. As an example, snapshots at different times during the dynamics of the largest cluster for a given size are shown in Figure 6.5 in both nucleating and prenucleating regimes of a typical simulation run.

These snapshots indicate that only the clusters with crystalline structure grow up to a stable size whereas the clusters with no crystalline order disintegrate back in the bulk. The formation of the crystalline structure in the nucleating regime cluster indicates that crystallization plays an important role in the nucleation mechanism of the short range

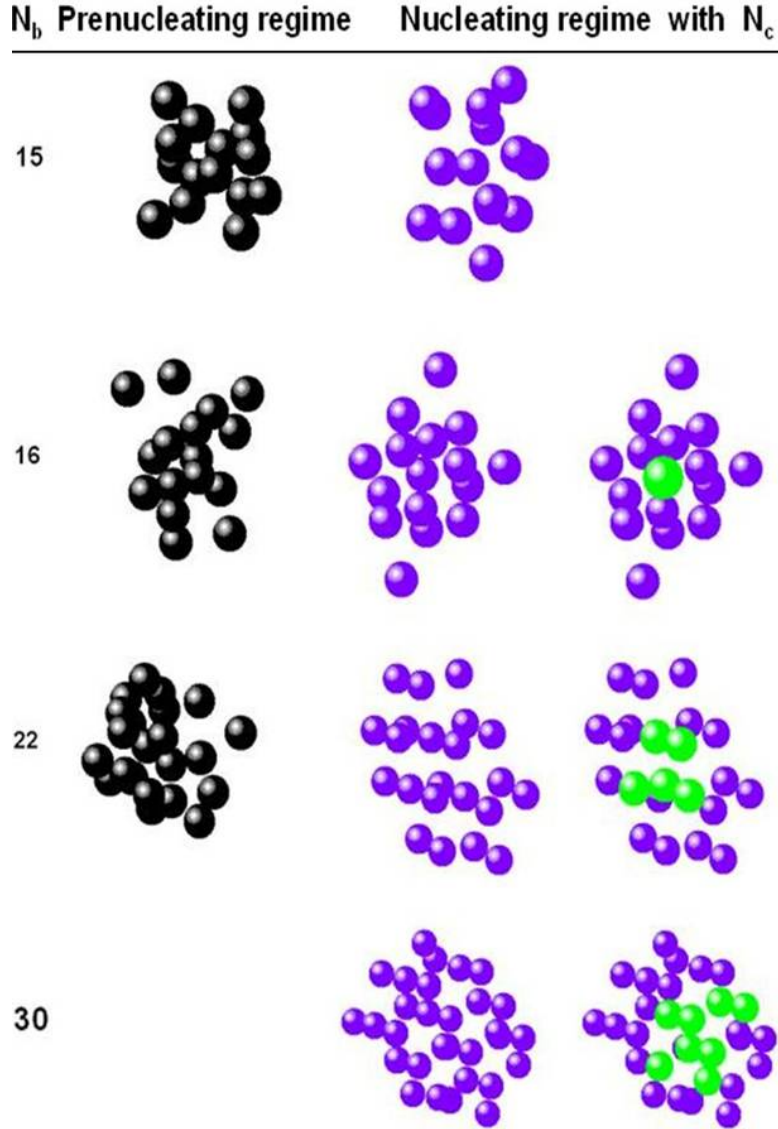


Figure 6.5: A comparison of the crystalline structure between the prenucleating and nucleation regime clusters of a given size N . No crystalline structure is observed in the prenucleating clusters (in black color) whereas nucleating regime clusters have the ordered structure indicated by crystalline particles N_c

interaction colloidal system and the nucleating clusters are not only energetically more stable but also they develop some ordered structure in their core during their growth.

We also characterize the crystalline structure of the growing cluster. To characterize such a cluster at different times during the growth process, we compute the radius of gyration

R_g and the perimeter radius R_p for the growing cluster. For a compact spherical cluster, R_p is related to R_g such that $R_p = \sqrt{5/3}R_g$ such that the core of the cluster is comprised of all particles residing at a distance $\leq R_g$ from the center of mass and the cluster surface as a collection of all particles residing at a distance $\geq R_p$ from the center of mass. Next we calculate the distance of the i th nearest neighbor (NN) of each particle and average over the core and surface particles separately. At the latest time, the cluster core shows 12 NN within a small spread of distance indicating a closed packed crystal structure (fcc or hcp). A subsequent discontinuity in distance indicates the beginning of the next NN sequence and six such next NNs follow. Another weak discontinuity comes next and then the sequence of 12 third NNs follows. In contrast, at earlier times, the growing cluster has only five or six pure NNs at separation of the position of the minima of the interaction potential and then a sequence of neighbors whose distance increases continuously, indicating a liquidlike behavior of the particles. We have also observed that this liquidlike morphology of the cluster at early times is strikingly similar to the surface structure of the cluster at late times.

Next, we compute local bond order parameters for particles in the growing cluster, as described in details in chapter 5. Based on our results for the frequency distribution $P(q_6)$ for the cluster core, we observe that the crystal structure inside the core of the cluster is predominantly a mixture of fcc and hcp. Similar analysis of the bond orientational order of the surface sites at late times is compared with the core of the growing cluster at early times as shown in Fig. 6.5.

From the broad distribution of the order parameters observed in Fig. 6.6, one can conclude that both the early time cluster core and the late time surface sites are liquidlike in structure. These results are in good agreement with experimental results obtained from real-space imaging of colloidal crystallization [25]. We do not see any evidence of a bcc structure either at early times or at the surface of the growing cluster at late times. It seems that the hcp structure is more dominant at early stages while the fcc structure is dominant in the later stages. Our analysis for $P(q_4)$ supports these conclusions.

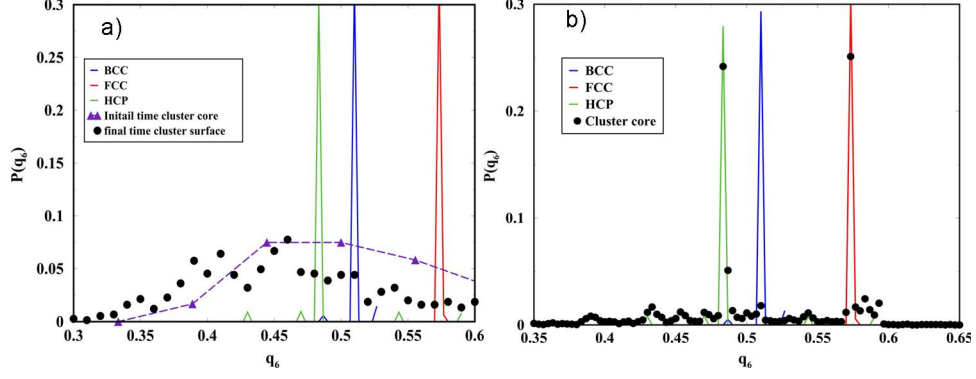


Figure 6.6: (a) Distribution of bond order parameter q_6 for surface particles at a late time of $t=40,000$ of the nucleating cluster for $Um=4kT$, $\zeta = 0.05$, and $f = 0.002$ and its comparison with an early time cluster core at $t=8500$. Distribution for pure crystals of bcc, fcc, and hcp are also shown in the figure. (b) Distribution of bond order parameter q_6 for the nucleating cluster core in comparison with pure crystals of bcc, fcc, and hcp.

6.3 Symmetric Structures of Small Size Clusters and Their Distribution

During nucleation process, while a nucleating cluster is forming and growing in the system, different small size clusters grow and disappear in the bulk. To observe the presence of the most symmetric structures in our system for a given size N , we accumulated the clusters of different sizes at different times as they grow and dissolve in the system. We classified the clusters of a given size based on the number of contacts, C , present in the cluster. In the case of short-range interaction, where the energy of the cluster is proportional to the number of contacts, the bond length (r_{min}) of the contacts can be approximated by the range of interaction (r_c) between the particles (*i.e.* $r_{min} = r_c$) whereas, for the long-range interaction, the bond length is approximated by neighbor separation for the particles (r_{bond}) in the cluster (*i.e.* $r_{min} = r_{bond}$). Furthermore, since our system is not in equilibrium with the environment and the clusters are energetically unstable, so in order to reduce the thermal effects, we increase the quench to $10kT$ instead of $4kT$ and hence the volume fraction is lowered such that only one or few isolated clusters grow in the system at $10kT$. First, we study the structure of small size clusters for the short range colloidal system where the

range of interaction is 5% the size of the particles. A list of maximum number of contacts (C_{max}) is shown in Table1 for such system in comparison with the theoretically calculated values of C_{max} using the concept of minimally rigid packing of spheres. For details about the Packing of Spheres, see reference [111]. For example, for a cluster of size $N = 6$, there can be a minimum of 5 and maximum of 12 possible contacts. So, in our system, we can see a distribution of contacts from minimum of $C_{min} = 5$ to the maximum of $C_{max} = 12$. After selecting the clusters at different times during the nucleation process, we can filter out the clusters with maximum number of contacts (for example, 12 contact clusters for $N = 6$). Based on the finite sphere packing calculations [112], there are two possible structures (octahedron and polytetrahedron) with maximum number of contacts ($C_{max} = 12$) for $N = 6$ size clusters. The presence of these two structures can be observed based on the moment

Table 6.1: *A comparison of our simulation clusters with maximum number of contacts for a given size ground state cluster with a short range interaction system and long-range interaction such as LJ system are also given.*

n	C_{max} for short range intercation	C_{max} in our System for $r_c = 1.05$	C_{max} for LJ interaction
3	3n-6	3n-6	3n-6
4	3n-6	3n-6	3n-6
5	3n-6	3n-6	3n-6
6	3n-6	3n-6	3n-6
7	3n-6	3n-5	3n-5
8	3n-6	3n-5	3n-5
9	3n-6	3n-4	3n-4
10	3n-5	3n-4	3n-3
11	3n-4	3n-3	3n-2
12	3n-3	3n-3	3n
13	3n-3	3n-2	3n+3
14	3n-2	3n-1	3n+3
15	3n-1	3n-1	3n+3

of inertia (I) and symmetry number (σ) calculations. The most symmetric structures will have lower I value and higher symmetry number value as compared to the one with less symmetric structure. These two parameters are also related through the rotational partition

function (*i.e.* $Z_{rot} \approx \sqrt{I}/\sigma$). So the smaller values of Z_{rot} will represent the more symmetric structures in the system. Since, it has been proposed earlier by Meng et. al. [113] that rotational entropy makes the largest contribution to the free energy difference between the two structures in equilibrium so the analysis here is based on the calculation of these two parameters. For the calculations of symmetry numbers [114], we make use of an algorithm mentioned in ref. [115]. Since our clusters, being in the bulk, are not in equilibrium with the environment, it is difficult to achieve the exact value of the symmetry numbers for a given cluster with higher symmetry numbers. For example, for the case of Octahedron structure, O_h , the exact value of symmetry number is $\sigma = 24$. But in our calculations, we get a broad distribution of symmetry numbers ranging from $\sigma = 4$ to $\sigma = 24$ as shown in the figure 6.7.

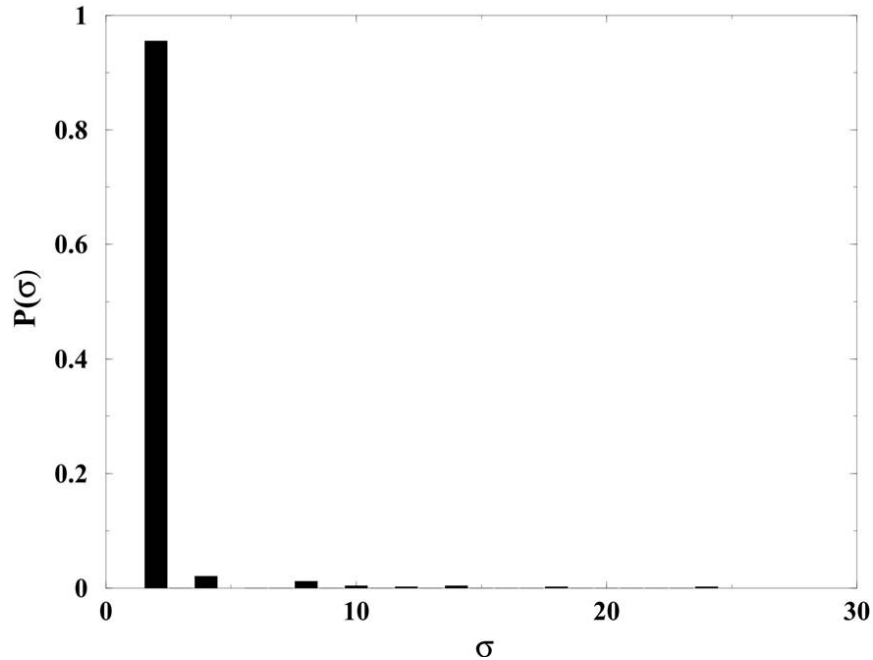


Figure 6.7: A plot of the distribution of symmetry numbers calculated for $N = 6$ size clusters with $C_{max} = 12$.

The calculations of the symmetry number (σ) are very sensitive to the positions of the particles and since the clusters are not in equilibrium with the environment, the broadness in distribution is due to the thermal noise present in the system. On the other hand, since

most symmetric structures have lower moment of inertia (I) values [116], these calculations seem more reliable as shown in fig. 6.8.

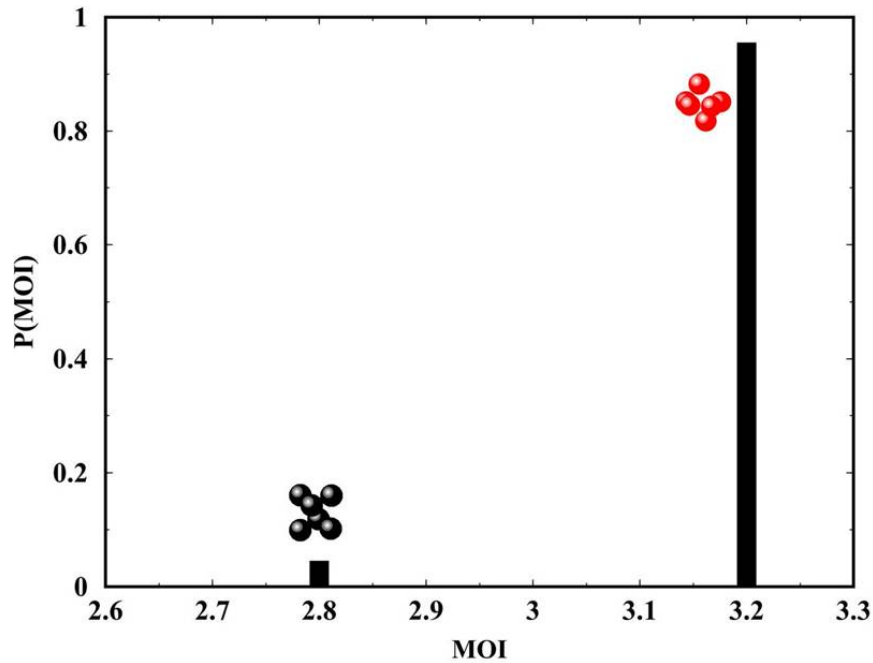


Figure 6.8: A plot of the moment of inertia (MOI) distribution for $N = 6$ cluster. Less symmetric structure polytetrahedron (red structure) is found to appear 20 times more frequently as compared to more symmetric one of octahedron (black structure).

The distribution shows that the most symmetric ones occur less frequently as compared to the less symmetric ones i.e. less symmetric structure of polytetrahedron appears approximately 25-30 times more frequently as compared to the most symmetric Octahedron structure, even though both structures are energetically same (as both have same number of contacts). To confirm the validity of moment of inertia calculations regarding the distribution of the structures, we also made use of the $W_6(i)$ parameter calculations [31], based on the measurement of the local bond order parameters defined in eqn. 5.8 and it describes the order of the neighbors around each particle in the cluster. Mathematically, it is defined in chapter 5. Each structure has unique value of W_6 parameter [31] and we calculate the W_6 for each particle and average over all the particles in the cluster. Based

on these calculations, we also found that the distribution of the structures is very much consistent with our moment of inertia (I) calculations. For smaller size clusters (i.e. $n = 3,4,5$), moment of inertia calculations show that there is only one ground state structure with maximum number of contacts present in the system, another observation consistent with the experiment and theory mentioned in ref. [113].

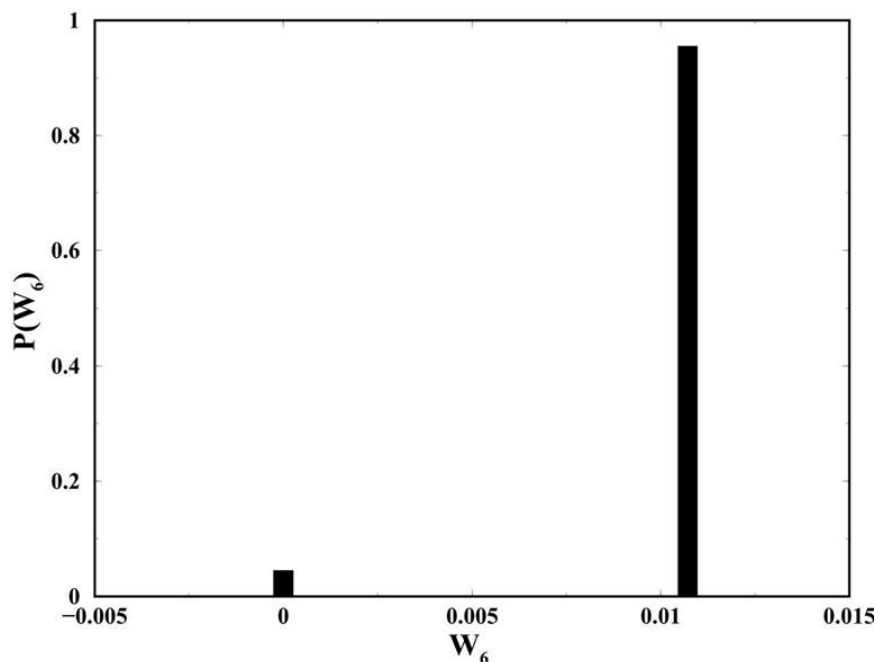


Figure 6.9: A plot of the W_6 distribution showing the comparative appearance of octahedron and polytetrahedron structures in the system. $W_6 = 0.0$ is indicative of the appearance of the Octahedron while $W_6 = 0.013$ indicates the formation of Polytetrahedron.

For the higher size clusters, the number of ground state structures increases with minor differences in their moment of inertia values and it becomes difficult to distinguish these structures based on this analysis. But based on the symmetry number calculations, we can identify the presence of most symmetric structures for $N=7$ and $N=8$. Figure 8 shows our analysis based on the symmetry number calculations and it can be seen that the most symmetric structures do appear in the bulk and the probability of the occurrence is very much comparable to the theoretically and experimentally observed values [113]. For the case

of $N = 7$, the most symmetric structure is D_{5h} and our calculations indicate the presence of this structure in the bulk sample and more surprisingly, this distribution is very much comparable to experimental value of 3% . Also, for the case of $N = 8$, we did not find any presence of the highly symmetric structures of T_d , and D_{3d} , which is yet another evidence of the relevance of our results with the experimental observations by Meng et al.

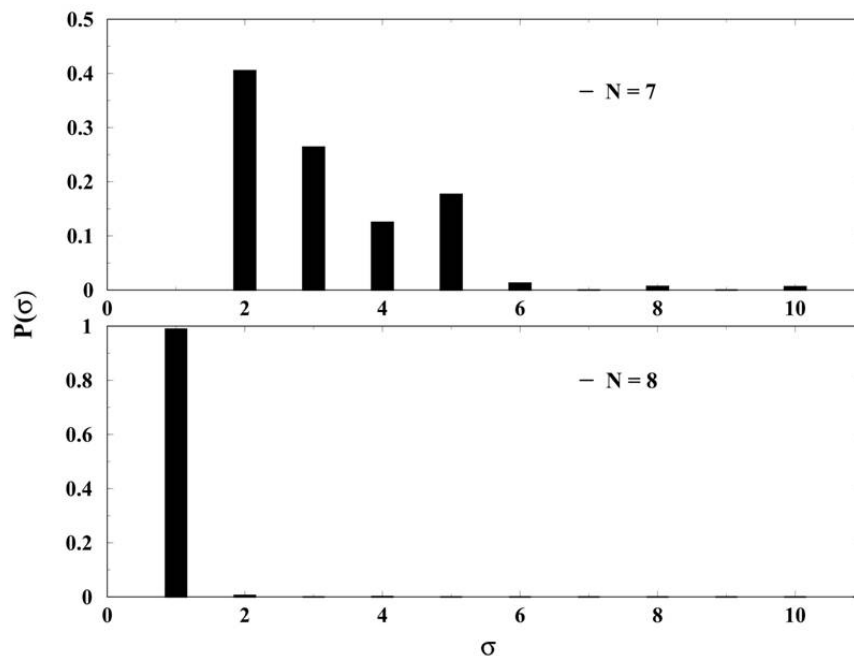


Figure 6.10: A plot of the distribution of symmetry numbers calculated for $N = 7$ and $N = 8$ with maximum number of contacts. About 4 % presence of the most symmetric structure (D_{5h}) for the $N = 7$ and appearance of no symmetric structures of T_d , D_{3d} and D_{2d} for $N = 8$ in the sample is surprisingly similar to the experimental observations mentioned in the text.

Next, we study the effects of range of interaction on the distribution of these structures. For this purpose, we studied these structures for $r_c = 1.3d$ and $1.8d$ respectively. It has been observed that for these long range systems, the number of contacts of the ground state structures is similar to the Lennard-Jones potential ground state clusters [117] mentioned in the Table 6.1. For example, for $N=13$, we observed the presence of icosahedral structures in the bulk for $r_c = 1.3d$ and $r_c = 1.8d$ systems. During our study of nucleation process,

it was also noticed that the distribution of the symmetric structures is same in the pre-nucleation and nucleation regimes indicating that most symmetric structures do not play any role in the formation of the stable nucleating cluster. Also, an interesting observation during our analysis was to study the nascent structures for a given size cluster. Based on the distribution of number of contacts for both short range and long range systems, we observe that the small size nascent clusters are relatively open structures (i.e. $C < C_{max}$). From this observation, we can conclude that the small size clusters have open structures in the beginning and as the time progresses, they develop into either larger size clusters by the addition of monomers/dimers or grow into more compact structures.

6.4 Morphology and growth kinetics for shallow quenches

In this section we continue with quenches to a depth of $4kT$ but increase the volume fraction of the colloids. In Fig. 6.11, we show snapshots for the system at various times for $f = 0.005$ and $\zeta = 0.1$. Now several clusters nucleate and grow with time. The shape of the clusters is

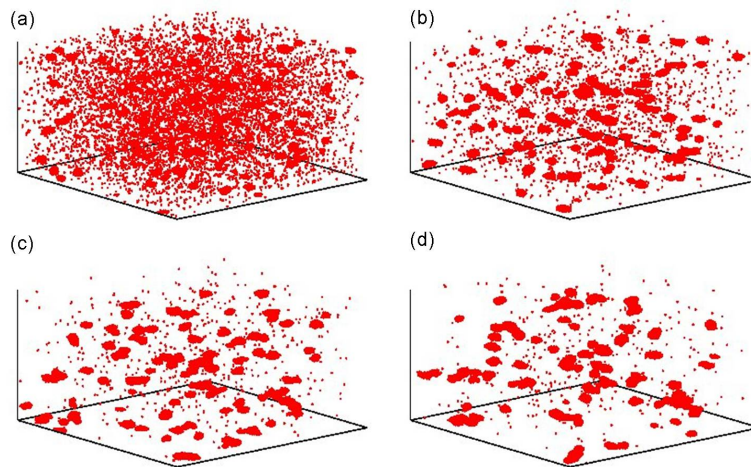


Figure 6.11: Snapshots of the system for a $Um=4kT$ quench with $f=0.005$ and $\zeta = 0.1$ at different times: (a) $t=1000$, (b) $t=2000$, (c) $t=5000$, and (d) $t=10\ 000$.

generally round for all values of ζ . When two clusters meet each other, it seems that they have time to coalesce into one spherical droplet before another cluster is encountered. If

the clusters do not encounter a any other clusters, spherically round clusters grow by the addition of monomers in the system. Next, we analyze at the morphology of the clusters by calculating the *Structure Factor* $S(q)$. In Fig. 6.11, we show the log-log plot of the structure factor $S(q, t)$ versus q . From the figure 6.12 for $\zeta = 0.03$, a fit of slope -4 to

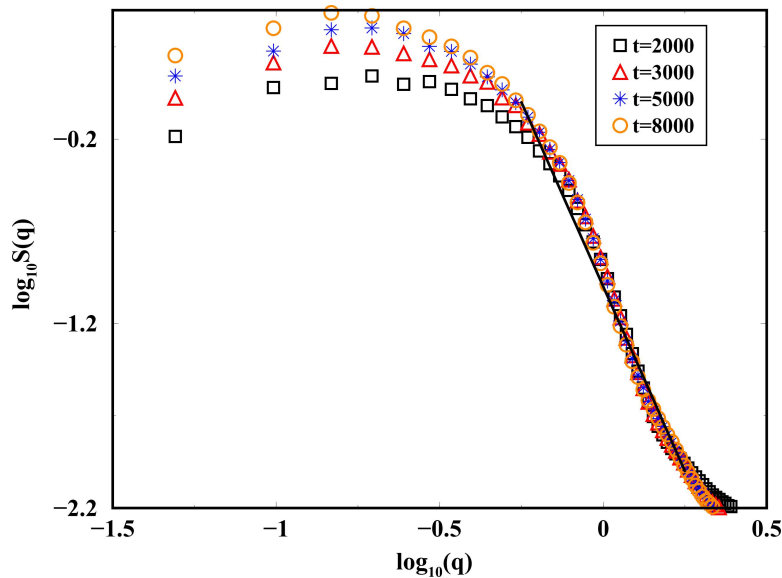


Figure 6.12: Log-log plot of the structure factor $S(q, t)$ as a function of q at different times for system with $U_m = 4kT$, $f = 0.005$, and $\zeta = 0.03$. For large and intermediate q values, $S(q)$ is consistent with Porods law although some deviations from q^{-4} form can be observed.

the data at different times, during the growth, shows that $S(q, t)$ is consistent with Porods law [118] [$S(q) \sim q^{-4}$] over a large range of k values, confirming our direct observations that the growing clusters are compact at both short and large length scales. Furthermore, we studied the growth dynamics by studying the variation of radiation of gyration R_g with time. In Fig. 6.13, we show log-log plots of average radius of gyration R_g of the clusters as a function of time for $\zeta = 0.03$ and $\zeta = 0.1$. Initially, we observe a sudden fast growth of R_g corresponding to heterogeneous nucleation of many clusters ($100 \leq t \leq 1000$). Subsequently, these clusters grow with time with a power law

$$R_g \sim t^n \tag{6.4}$$

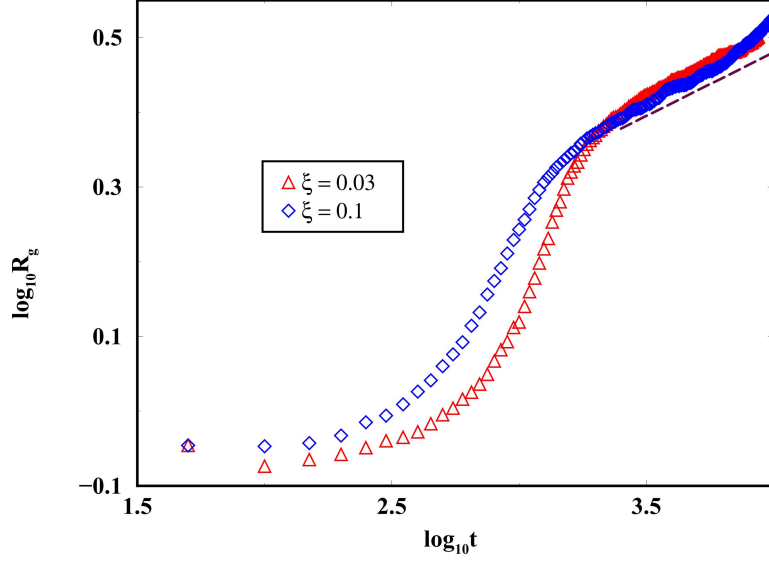


Figure 6.13: Log-log plot of radius of gyration R_g as a function of time for $f = 0.005$, $Um = 4kT$, and two different ζ values (0.03 and 0.1). The dotted line with slope of 0.17 is a guide to the eyes.

with $n \approx 0.17$. As suggested by Binder and Stauffer [70] and Binder and Kalos [108] and later summarized by Gunton et al. [72] and Furukawa [71], domain growth kinetics at this stage is mostly controlled by cluster diffusion until eventually two such clusters coalesce. The mechanics of cluster diffusion is dominated by *surface reorganization of the particles* in the cluster. Following Gunton et al. [72], we briefly summarize these arguments below.

The diffusion constant of a cluster containing N particles can be estimated as

$$D_N \approx \omega(\Delta x_G)^2 \quad (6.5)$$

where Δx_G is the change in the center of mass position by a given process of particle motion in the cluster and ω is the rate at which such a process takes place. In a typical process of particle motion on the surface of a cluster, a particle changes its position by a few units of σ . As a result the center of mass of a cluster containing N particles changes by

$$\Delta x_G \approx N^{-1} \quad (6.6)$$

in units of σ . As the rate of such a particle motion at the surface is proportional to the number of surface sites, one estimates

$$\omega \approx R_g^2 \quad (6.7)$$

If the clusters are compact, $R_g \sim N^{1/d}$, where d is the spatial dimension. One thus obtains

$$D_N \approx N^{2/d-2} \quad (6.8)$$

Once an estimate for cluster diffusion constant is obtained, one can now treat the cluster-cluster coalescence in terms of the mean-field Smoluchowski equation (SE) [119] which expresses the rate of change of cluster concentration, $n_k(t)$, containing k monomers per cluster as

$$\frac{dN_k}{dt} = \sum_{i=1}^{k-1} K(i, k-i)n_i n_{k-i} - n_k \sum_{i=1}^{\infty} K(i, k)n_i \quad (6.9)$$

The kernel $K(i,j)$ expresses the rate of aggregation or coalescence between clusters of size i with clusters of size j . If K is a homogeneous function of cluster size, i.e., $K(ai, aj) = a^\lambda K(i, j)$, where λ is the degree of homogeneity, the solutions to the SE are self-preserving scaling solutions for n_k . If one further assumes that the cluster size distribution is approximately monodisperse, one can write the appropriate collision kernel as

$$K \sim N^\lambda \quad (6.10)$$

The kinetic exponent z , which characterizes the power-law decay with time of the number of clusters $N_c(t)$, is related to the homogeneity λ by

$$z = \frac{1}{1-\lambda} \quad (6.11)$$

In addition, since $N_c N = \text{constant}$ (=the number of monomers), one easily finds that $R_g(t) \sim t^n$, where

$$n = z/d \quad (6.12)$$

for compact clusters. The next step in this scaling description [120], [121] is to pinpoint limiting cases of the functional form of the kernel and hence determine the homogeneity. The rate at which two clusters collide, K , is proportional to their relative collision cross-sectional area A and relative velocity, v , yielding $K \sim Av$, consistent with the units of $[L^3/t]$. One typically writes A as $A \sim Rg^2$, where Rg is the radius of gyration of a cluster with number of particles N . For the diffusive case of cluster motion, v becomes a characteristic velocity relevant for diffusion. This velocity must scale as

$$v \sim \frac{D_N}{R_c} \quad (6.13)$$

where D_N is the diffusion constant of a cluster containing N particles and R_c is a characteristic diffusional length scale. In the dilute limit of the StokesEinstein diffusion, Rg is the only relevant length scale in the system and one can write $v \sim D_N/Rg$. In addition, $A \sim Rg^2$. Thus one finds $K \sim D_N Rg$, a result originally derived by Smoluchowski [119] in a more rigorous fashion. For the BinderStauffer [70] cluster growth mechanism $D_N \approx N^{2/d-2}$ and for compact clusters $Rg \sim N^{1/d}$. One thus finds

$$K \sim D_N Rg \sim N^{(2/d)-2+(1/d)} \sim N^{3/d-2} \quad (6.14)$$

Hence the homogeneity

$$\lambda = \frac{3}{d} - 2 = -1 \quad (6.15)$$

in three dimensions and

$$z = \frac{d}{3d-2} = \frac{1}{2} \quad (6.16)$$

also in three dimensions. The domain growth kinetics is then governed by the exponent n which is given by

$$n = \frac{z}{d} = \frac{1}{3d-3} \quad (6.17)$$

Our observed value of $n \approx 0.17$ agrees quite well with the theoretical prediction. In addition, we note that this same growth exponent has recently been observed in experiments on

depletion driven colloids [102]. For the case of denser systems, we study the shallow quench at $f = 0.01$ and $f = 0.02$. A plot of the morphology for these two volume fractions is shown in figure 6.14. The morphology of domains in figure 6.14 is similar to the interconnected

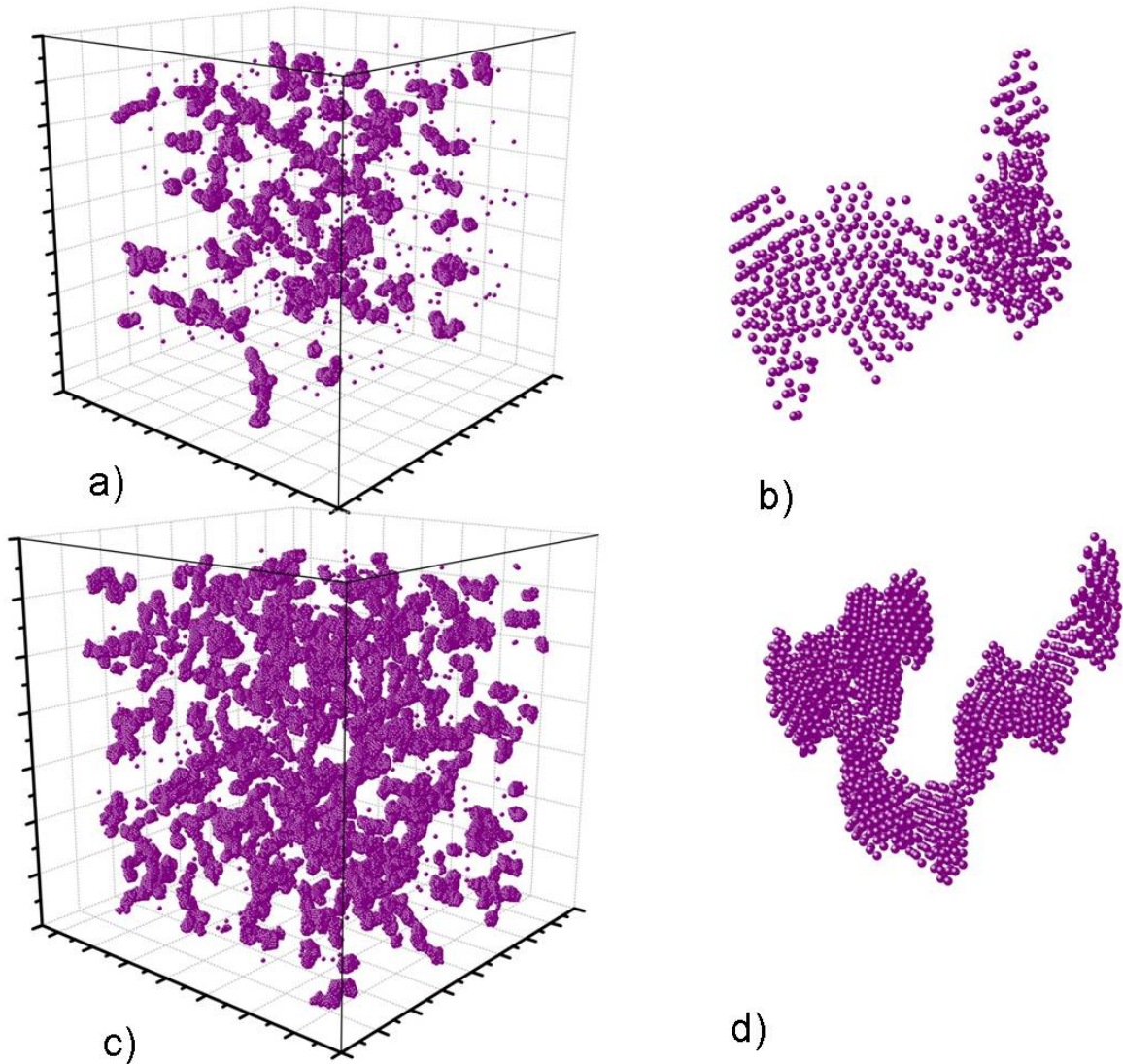


Figure 6.14: Late time configuration for $U_m = 4kT$ and $\zeta = 0.1$ for (a) $f = 0.01$ and (c) $f = 0.02$ at $t=5000$. A zoomed-in cluster for the corresponding cases are shown in (b) $f = 0.01$ and (d) $f = 0.02$.

structure seen in a typical spinodal decomposition of a liquid-liquid mixture. The structure factor data for these volume fractions show interesting features.

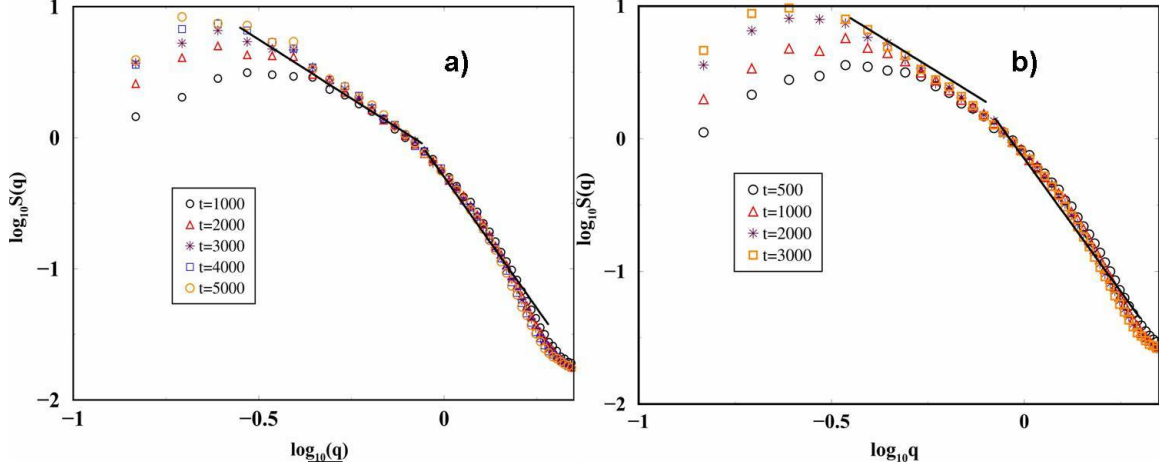


Figure 6.15: (a) Log-log plot of the structure factor $S(q,t)$ as a function of q at different times for $U_m = 4kT$, $f = 0.01$, and $\zeta = 0.1$. Our results are consistent with Porods law for large q values and for small q values; a slope of -1.8 is consistent with the data. (b) Log-log plot of the structure factor $S(q,t)$ as a function of q at different times for $U_m = 4kT$, $f = 0.02$, and $\zeta = 0.1$. Our results are consistent with Porods law for large q values and for small q values; a slope of -1.8 is consistent with the data.

Fits to the data in Figs. 6.15(a) and 6.15(b) show that $S(q)$ is consistent with Porods law [$S(q) \approx q^{-4}$] for large q values while for intermediate values of q , $S(q) \approx q^{-D_f}$ with $D_f \sim 1.8$ consistent with the well-known DLCA value. [109] We see such hybrid morphology in Fig. 6.13 as well when we zoom in to the clusters: the growing clusters are compact at short length scales but are fractal-like at large length scales [76]. Growth kinetics for these denser systems is still controlled by cluster-cluster interactions. As before, clusters do diffuse around until they meet each other. However, the clusters at these denser systems do not seem to coalesce into compact clusters when they meet but keep their ramified shape. Thus one would expect that the growth-law exponent would crossover to the irreversible limit, i.e., to the DLCA limit for dense systems. Further, we studied the variation of the number of clusters with time. In Figs. 6.16(a) and 6.16(b), we plot the number of clusters versus time in log-log plots for volume fractions $f = 0.01$ and $f = 0.02$, respectively. For $f = 0.02$, $N_c(t) \sim t^{-1}$ consistent with the DLCA value of $z = 1$ as discussed above. Note that if the clusters are compact and they would completely coalesce when they meet, $z = 1/2$ corresponding to the

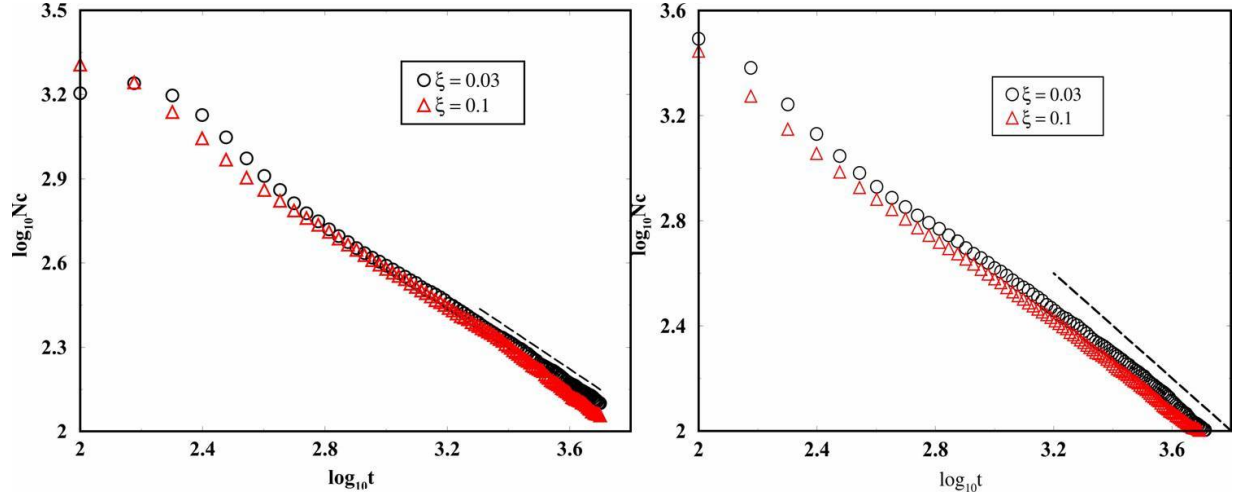


Figure 6.16: (a) Log-log plot of the number of clusters N_c as a function of time for $U_m = 4kT$ and $f = 0.01$. The dotted line with the slope of -0.75 is a guide to the eyes. (b) Log-log plot of the number of clusters N_c as a function of time for a $U_m = 4kT$ and $f = 0.02$. The dotted line with the slope of -1 is a guide to the eyes.

value of $n=1/6$ seen before. It seems that for $f=0.01$, one gets an intermediate value of $z \approx 0.75$, in between the coalescence and the DLCA limit. These conclusions are supported

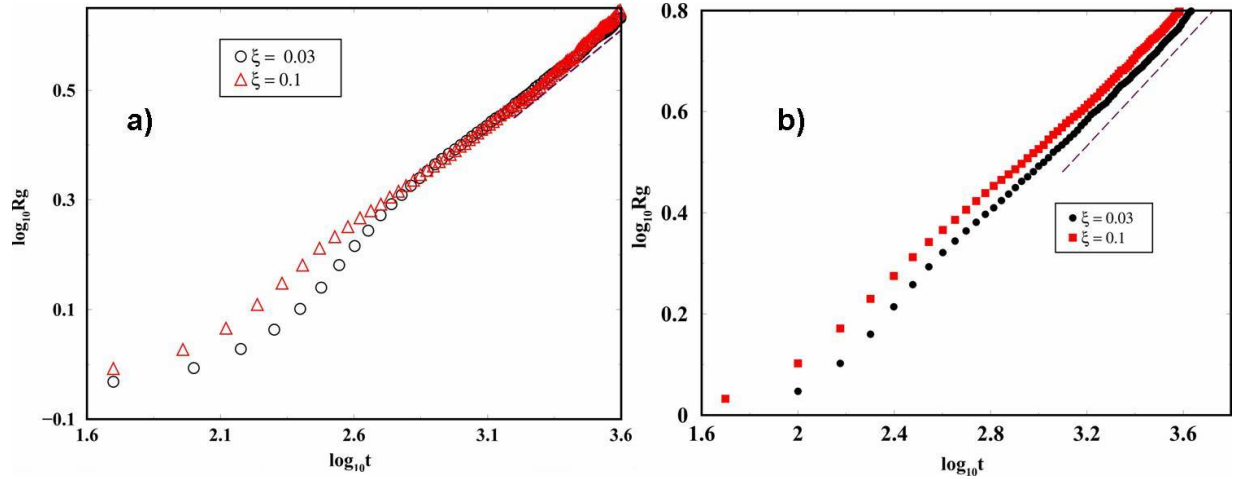


Figure 6.17: (a) Log-log plot of radius of gyration R_g as a function of time for $U_m = 4kT$ and $f = 0.01$. The dotted line with the slope of 0.4 is a guide to the eyes. (b) Log-log plot of radius of gyration R_g as a function of time for $U_m = 4kT$ and $f = 0.02$. The dotted line with the slope of 0.55 is a guide to the eyes.

by the data for the radius of gyration as shown in Figs. 6.17(a) and 6.17(b). For $f=0.02$, one gets a clear-cut DLCA value for $n = z/D_f = 0.55$ with $z=1$ and $D_f = 1.8$, while for $f=0.01$, the growth exponent is yet to reach the DLCA limit and one finds an intermediate exponent of $n \sim 0.4$. This intermediate value of $n \sim 0.4$, however, is consistent with the intermediate value of $z \approx 0.75$ seen before as $n = z/D_f = 0.75/1.8 = 0.42$. We now provide estimation for the intermediate value of the growth exponent seen above. For this purpose we assume that the cluster growth kinetics is still controlled by a BinderStauffer mechanism but clusters do not coalesce completely when they meet each other. As a result clusters can be treated as fractals in the modified BinderStauffer scheme instead of treating them as compact objects. Equations 6.5 and 6.6 will still be valid but now $R_g \sim N^{1/D_f}$ and hence

$$D_N \approx N^{2/D_f-2} \quad (6.18)$$

The kernel K is then given by

$$K \sim D_N R_g \sim N^{2/D_f-2} \sim N^{(2/D_f)-2+(1/D_f)} \quad (6.19)$$

yielding a homogeneity of $\lambda = 3/D_f - 2$, a kinetic exponent of

$$z = \frac{1}{1-\lambda} = \frac{D_f}{3D_f-3} \quad (6.20)$$

and a growth exponent of

$$n = \frac{z}{D_f} = \frac{1}{3D_f-3} \quad (6.21)$$

For $D_f = 1.8$, one finds $z = 0.75$ and $n = 0.42$ in excellent agreement with our simulation results described above.

6.5 Morphology and growth kinetics for deep quenches

In this section, we study morphology and growth kinetics of clusters for a deep quench characterized by $U_m = 10kT$ and $\zeta = 0.1$. Snapshots of the system for two different volume fractions $f = 0.002$ and $f = 0.02$ are shown in Fig. 6.18.

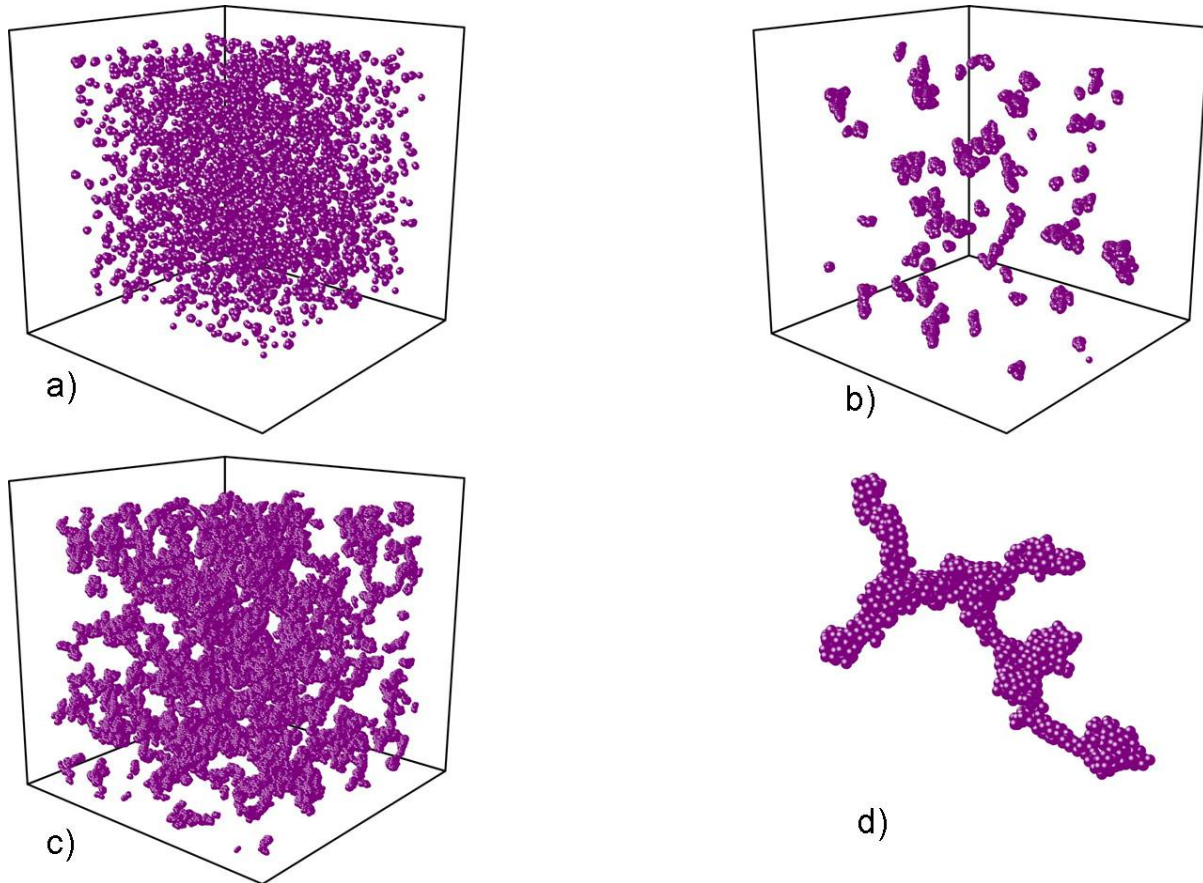


Figure 6.18: Snapshots of deep quenched ($U_m = 10kT$) systems for two different volume fractions. (a) and (b) are for a volume fraction $f = 0.002$ at $t = 250$ and $t = 10\,000$, respectively. (c) is for $f = 0.02$ at $t = 5000$ while (d) shows the zoomed-in version of a typical cluster of the system shown in (c). Short range crystalline order in the zoomed-in cluster of (d) is much weaker than the ones seen, for example, in Figs. 6.4(b) and 6.4(d).

As observed in Fig. 6.18(b), now the clusters have fractal morphology even at very low volume fractions. Also, noteworthy is the fact that the zoomed-in version of a typical cluster of the system [Fig. 6.18(d)] shows much weaker short-range crystalline order than seen in

clusters for 4kT quenches shown in Figs. 6.14(b) and 6.14(d), for example. This is expected as for deeper quenches, colloidal particles do not break as often from the parent cluster and thus get stuck in low coordination number sites. Growth kinetics in this case crosses over to the DLCA limit as the volume fraction is increased. For a dilute system characterized by $f = 0.002$, the kinetic exponent is given by $z \sim 0.75$ consistent with our scaling analysis for the intermediate regimes as can be seen from Fig. 6.19(a). It is interesting to note that for

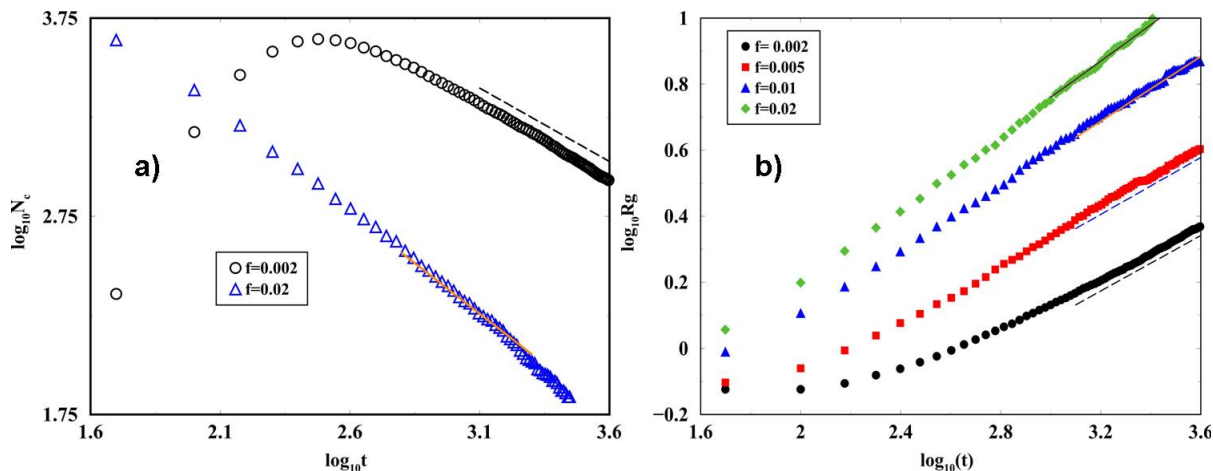


Figure 6.19: (a) Log-log plot of the number of clusters N_c as a function of time for a deep quenched system of $U_m=10kT$ at $f=0.002$ and $f=0.02$, respectively. The kinetic exponents computed from the slopes of these graphs are $z = 0.75$ and $z = 1$, respectively. (b) Log-log plot of radius of gyration R_g as a function of time for a 10kT deep quenched system with $\zeta = 0.1$ for four different values of the volume fraction f : 0.002, 0.005, 0.01, and 0.02. The growth exponents n for these volume fractions are given by $n=0.4$, 0.43, 0.5, and 0.55. The growth exponent at low volume fractions is consistent with the intermediate regime scaling value of $n \sim 0.42$ discussed in the text while for larger volume fractions one asymptotically obtains the pure DLCA value of $n = 0.55$.

this deep quench, the intermediate regime result applies to much smaller volume fractions than for the 4kT quench analyzed before. The kinetic exponent takes on a pure DLCA value of $z = 1$ for $f = 0.02$. The evolution of the growth exponent n with volume fractions is depicted in Fig. 6.15(b). For low volume fractions, we again obtain the intermediate value of the growth exponent given by $n \sim 0.42$ while for larger volume fractions, the growth exponent is given by a pure DLCA value of $n = 0.55$.

6.6 Conclusion.

In summary, we have carried out extensive BD simulations to study cluster morphology and growth kinetics in quenched short-range attractive colloidal systems. The model potential we have studied here is given by the AOV depletion interaction. However, we expect that our results would apply for general short-range attractive potentials. For very low volume fractions and shallow quench depths, we have studied the morphology of the growing crystals in terms of various bond orientational order parameters. Also, we estimated the critical size of the nucleating cluster based on the fact that most energetic clusters would grow out to form a stable nucleating cluster. We also observed an ordered structure arising in the nucleating clusters indicating that the nucleating clusters not only are energetically more favorable but the presence of an ordered structure plays an important role to their stable growth. Although, the nucleating cluster seem to grow some ordered structure in their core, the overall structures are quite liquid-like at early times. At late times, the core of the crystal is characterized by a close-packed symmetry (mixture of fcc and hcp) while the surface of the crystal at late times is liquid-like. We have not seen any evidence of a bcc structure at early times or at the surface of the growing crystal. As the volume fraction is increased for a shallow quench, cluster-cluster interactions control the growth kinetics. For low volume fractions, clusters seem to diffuse following a mechanism described by Binder and Stauffer many years ago. When two clusters meet each other, they coalesce and clusters remain compact. In this regime the growth-law exponent agrees well with BinderStauffer predictions and with recent experimental results. When volume fractions are increased further, clusters do not have time to completely coalesce when they meet each other. Clusters show hybrid morphology now: ramified on large length scales but close-packed crystalline at short length scales. We have extended the BinderStauffer mechanism to explain the observed growth kinetics for this intermediate regime. Such an intermediate value of the growth exponent ($n \approx 0.42$) has not been observed in experiments yet and our simulations would motivate further experimental studies. For deeper quenches, clusters are

fractals even at low volume fractions and the intermediate value of the kinetic exponent is observed even at very low volume fractions. When volume fractions are increased further, the growth kinetics asymptotically reaches the DLCA limit.

Chapter 7

Conclusions

In this thesis work, we present extensive simulation studies of the *self-assembly* of ligated nanoparticles and short-range attractive colloidal systems. For the case of ligated nanoparticles, we have developed a phenomenological model to describe the interactions between two such particles in solution. Besides the van der Waals interaction between the nanoparticles, we also consider the free energy of mixing and elastic compression of the ligands in the model. The location of the minimum of the phenomenological pair potential agrees well with the experimentally observed values for the superlattice constants for gold nanoparticles decorated with decanethiol, dodecanethiol, and hexadecanethiol ligands. Next we use the model potential as input for Brownian dynamics simulations to obtain a broad perspective in the dispersed-phase to solid-phase transition. For dodecanethiol ligated nanoparticles, the minimum of the interaction potential is $-3.1kT$. At room temperature, the system remains in the single phase until a critical volume fraction is reached, when the nucleation process starts. Analysis of a pre-nucleation induction period in terms of classical nucleation theory yields a supercluster interfacial tension that compares reasonably well with other theory and experimental measurements. We observe that most of the smaller sized pre-nucleating NPSCs have non-compact morphology whereas the larger sized NPSCs are compact, and the growth of the nucleating cluster is dominated by the addition/subtraction of monomers as postulated by CNT. An unexpected and surprising observation was that the pre-nucleation cluster size can occasionally range greater than the critical size in the

pre-nucleation regime without nucleation occurring. Only when a cluster with low enough energy occurs will nucleation ensue. Furthermore, our analysis of the crystalline structure of the nucleating cluster based on the bond orientational order parameter suggests that the formation of the stable nucleating cluster is a two step process. Initially, a liquid-like structure is formed. Subsequently, we observe the formation of different crystalline structures growing in the core of the cluster. At higher volume fractions, compact clusters are found to coexist with the dispersed phase. The kinetics of cluster growth in this case is compared with phase separations in binary mixtures.

For decanethiol-ligated nanoparticles, the model well depth is found to be deeper ($-5.15kT$), and simulations show hybrid, fractal-like morphology for the clusters. Cluster morphology in this case shows a compact structure at short length scales and a fractal structure at large length scales. The growth kinetics for this deeper potential depth is compared with the diffusion limited cluster-cluster aggregation (DLCA) model. There is very little experimental work available in the literature on the kinetics of self-assembly of nanoparticles. This is why a comparison of our Brownian dynamics simulation results to experiments is not possible at this time.

In the second part of the thesis, we have carried out extensive BD simulations to study cluster morphology and growth kinetics in quenched short-range attractive colloidal systems. The model potential we have studied here is given by the Asakura-Oosawa-Vrij (AOV) depletion interaction. However, we expect that our results would apply for general short-range attractive potentials as well. For very low volume fractions and shallow quench depths, we have studied the morphology of the growing crystals in terms of various bond orientational order parameters. Also, we have observed in our analysis that, in the case of very short range system (i.e. 5% of the diameter of the particles), the nucleating clusters are not only energetically more stable than the same sized pre-nucleating clusters but also develop some crystalline order in their structure. In spite of the presence of some crystalline structure in the core of the nucleating clusters, the overall structures are quite liquid-like

at early times. In contrast, on relatively long-range systems (i.e. 30% of the diameter of the particles), our simulations show that the nucleating clusters are liquidlike and no crystalline order is present in a nucleating cluster. However, the nucleating clusters are still energetically more stable as compared to the same sized prenucleating clusters. At late times, the core of the crystal in both short range and relatively long-range systems is characterized by a close packed symmetry (mixture of fcc and hcp) while the surface of the crystal at late times is liquidlike. We have not seen any evidence of a bcc structure at early times or at the surface of the growing crystal.

As the volume fraction is increased for a shallow quench, cluster-cluster interactions control the growth kinetics. For low volume fractions, clusters seem to diffuse following a mechanism described by Binder and Stauffer many years ago. When two clusters meet each other, they coalesce and clusters remain compact. In this regime the growth-law exponent agrees well with Binder-Stauffer predictions and with recent experimental results. When volume fractions are increased further, clusters do not have time to completely coalesce when they meet each other. Clusters show hybrid morphology: ramified on large length scales but close-packed crystalline at short length scales. We have extended the Binder-Stauffer mechanism to explain the observed growth kinetics for this intermediate regime. Such an intermediate value of the growth exponent ($n \sim 0.42$) has not been observed in experiments yet and our simulations would motivate further experimental studies. For deeper quenches, clusters are fractals even at low volume fractions and the intermediate value of the kinetic exponent is observed even at very low volume fractions. When volume fractions are increased further, the growth kinetics asymptotically reaches the DLCA limit.

Bibliography

- [1] M. Akbulut et al., *Langmuir* , 3961 (2007).
- [2] M. Faraday, *Phil. trans.* , 145 (1857).
- [3] J. Turkevich, page 86 (1985).
- [4] B. Gilbert, F. Huang, H. Zhang, G. A. Waychunas, and J. F. Banfield, *Science* **305**, 651 (2004).
- [5] K. L. Kelly, E. Coronado, L. L. Zhao, and G. C. Schatz, *J. Phys. Chem. B* **107**, 668 (2003).
- [6] R. L. Whetten et al., *Adv. Mater.* **8**, 428 (1996).
- [7] R. A. Sperling, P. R. Gil, F. Zhang, M. Zanella, and W. J. Parak, *Chem. Soc. Rev.* **37**, 1745 (2008).
- [8] X. M. Lin, G. M. Wang, C. M. Sorensen, and K. J. Klabunde, *J. Phys. Chem. B* **103**, 5488 (1999).
- [9] X. M. Lin, H. M. Jaeger, C. M. Sorensen, and K. J. Klabunde, *J. Phys. Chem. B* **105**, 3353 (2001).
- [10] X. M. Lin, C. M. Sorensen, and K. J. Klabunde, **11**, 198 (1999).
- [11] P. C. Ohara, D. V. Leff, J. R. Heath, and W. M. Gelbart, *Phys. Rev. Lett.* **75**, 3466 (1995).
- [12] D. V. Leff, P. C. Ohara, J. R. Heath, and W. M. Gelbart, *J. Phys. Chem.* **99**, 7036 (1995).

- [13] B. A. Korgel, S. Fullam, S. Connolly, and D. Fitzmaurice, *J. Phys. Chem. B* **102**, 8379 (1998).
- [14] S. R. Raghavan, J. Hou, G. L. Baker, and S. A. Khan, *Langmuir* **16**, 1066 (2000).
- [15] T. M. Krishna and J. C. Meredith, *Langmuir* **21**, 487 (2005).
- [16] P. Schapotschnikow, R. Pool, and T. J. H. Vlugt, *Nano Lett* **8**, 2930 (2008).
- [17] J. J. Cerdà, S. Tomàs, C. Holm, C. M. Sorensen, and A. Chakrabarti, *Phys. Rev. E* **78**, 031403 (2008).
- [18] A. M. Kulkarni and C. F. Zukoski, *Langmuir* **18**, 3090 (2002).
- [19] D. Kashchiev, *Nucleation: Basic Theory with Applications*, Butterworth-Heiemann, Oxford, 2000.
- [20] F. F. Abraham, *Homogeneous Nucleation Theory*, Academic Press, New York and London, 1974.
- [21] J. W. Mullin, *Crystallization*, Butterworth, 1972.
- [22] P. Vekilov, *J. Cryst. Growth* **275**, 65 (2005).
- [23] D. Erdemir, Y. A. Lee, and A. S. Myerson, *Acc. Chem. Res.* **42**, 621 (2009).
- [24] P. R. t. Wolde and D. Frenkel, *Science* **277**, 1975 (1997).
- [25] U. Gasser et al., *Science* **292**, 258 (2001).
- [26] E. Sloutskin, Nucleation of hard-sphere colloidal crystals, *Bull. of Amer. Phys. Soc.*, P-514, 2010, (March Meeting).
- [27] P. M. Chaikin and T. C. Lubensky, *Principles of Condensed Matter Physics*, Cambridge, 2000.

- [28] M. E. Fisher, *Physics* **3**, 255 (1967).
- [29] D. H. Everett, *Basic Principles of Colloid Science*, Royal Society of Chemistry, 1988.
- [30] J. N. Israelachvili, *Intermolecular and Surface Forces, 2nd Ed.*, ACADEMIC PRESS LTD, 1992.
- [31] S. Auer and D. Frenkel, *Adv. Polym. Sci.* **173**, 149 (2005).
- [32] R. A. L. Jones, *Soft Condensed Matter*, Oxford University Press, 2002.
- [33] A. Vrij, *Pure Appl. Chem.* **48**, 471 (1976).
- [34] S. Asakura and F. Oosawa, *J. Chem. Phys.* **22**, 1255 (1954).
- [35] Y. S. Lee, *Self-Assembly and Nanotechnology: A Force Balance Approach*, John Wiley and Sons, Inc, 2008.
- [36] H. C. Hamaker, *Physica* **4(10)**, 1058 (1937).
- [37] E. J. W. Verwey and J. T. G. Overbeck, *Theory of the Stability of Lyophobic Colloids*, Elsevier: Amsterdam, 1948.
- [38] R. Smitham, J. B.; and Evans and D. H. J. Napper, *J. Chem. Soc., Faraday. Trans.1* **71**, 285 (1975).
- [39] R. Evans and D. H. J. Smitham, J. B. and Napper, *Colloid Polym. Sci* **255**, 161 (1977).
- [40] L. Motte, F. Billoudet, and M. P. Pilani, *J. Phys. Chem.* **99**, 16425 (1995).
- [41] G. Poirier and E. Pylant, *Science* **272**, 1145 (1996).
- [42] J. Brandrup, E. H. Immergut, and E. A. Gruike, *Polymer Handbook*, Wiley: New York, 1999.

- [43] C. L. Yaws, *Chemical Properties Handbook*, McGraw Hill: New York, 1999.
- [44] C. Bain, J. Evall, and G. M. Whitesides, *J. Am. Chem. Soc.* **111**, 7155 (1989).
- [45] B. L. V. Parsad, S. L. Stoeva, C. M. Sorensen, and K. J. Klabunde, *Chem. Mater* **15**, 935 (2003).
- [46] R. K. Pathria, *Statistical Mechanics*, Elsevier, 2005.
- [47] L. Verlet, *Phys. Rev.* **159**, 98 (1967).
- [48] R. Kubo, *Rep. Prog. Phys. Suppl* **29**, 255 (1966).
- [49] W. F. Van Gunsteren and H. J. C. Berendsen, *Mol. Phys.* **45**, 637 (1982).
- [50] M. Griebel, S. Knapek, and G. Zumbusch, *Numerical Simulation in Molecular Dynamics*, Springer, 2007.
- [51] R. Sedgewick and P. Flajolet, *An introduction to the analysis of algorithms*, Addison-Wesley, 1996.
- [52] K. J. Klabunde, *Nanoscale Materials in Chemistry*, Wiley Interscience, New York, 2001.
- [53] B. L. V. Parsad, C. M. Sorensen, and K. J. Klabunde, *Chem. Soc. Rev.* **37**, 1871 (2008).
- [54] B. L. V. Parsad, S. I. Stoeva, C. M. Sorensen, and K. J. Klabunde, *Langmuir* **18**, 7515 (2002).
- [55] A. Centrone et al., *Proc. Nat. Acad. Sci.* **105**, 9886 (2008).
- [56] O. Uzun et al., **2**, 196 (2008).
- [57] H. Yan, S. Cingarapu, K. J. Klabunde, A. Chakrabarti, and C. M. Sorensen, *Phys. Rev. Lett.* **102**, 095501 (2009).

- [58] B. Abecassis, F. Testard, and O. Spalla, Phys. Rev. Lett. **100**, 115504 (2008).
- [59] M. D. Bentzon, J. V. Wonterghem, S. Morup, and A. Tholen, Philosophical Magazine **60**, 169 (1989).
- [60] C. B. Murray, C. R. Kagan, and M. G. Bawendi, Science **270**, 1335 (1995).
- [61] S. J. Khan, F. Pierce, C. M. Sorensen, and A. Chakrabarti, Langmuir **25(24)**, 13861 (2009).
- [62] P. R. Wolde et al., Phys. Rev. Lett. **75**, 2714 (1995).
- [63] S. Alexander and J. P. McTague, Phys. Rev. Lett. **41**, 702 (1978).
- [64] J. Lothe and G. M. Pound, J. Chem. Phys. **36**, 2080 (1962).
- [65] A. Egginton, K. C. S., D. Stauffer, and G. H. Walker, Phys. Rev. Lett. **26**, 820 (1971).
- [66] Racz and T. Vicsek, Phys. Rev. Lett. **51**, 2382 (1983).
- [67] A. Perini, G. Jacucci, and G. Martin, Phys. Rev. B **51**, 2382 (1983).
- [68] M. J. Lowe and D. J. Wallace, J. Phys. A **13**, L381 (1980).
- [69] R. Jullien and R. Botet, *Aggregation and Fractal Aggregates*, World Scientific, 1986.
- [70] K. Binder and D. Stauffer, Phys. Rev. Lett. **33**, 1006 (1976).
- [71] H. Furukawa, Adv. Phys. **34**, 703 (1985).
- [72] J. D. Gunton, san Miguel M., and P. S. Sahni, *Phase Transition and Critical Phenomenon*, Academic Press: London, 1983.
- [73] A. J. Bray, Adv. Phys. **43**, 357 (1994).
- [74] A. Chakrabarti, D. Fry, and C. M. Sorensen, Phys. Rev. E **69**, 031408 (2004).

- [75] E. B. Zuckerman, B. J. Oliver, C. M. Sorensen, and K. J. Klabunde, **1**, 12 (1989).
- [76] A. T. Skjeltrop, Phys. Rev. Lett. **58**, 1444 (1987).
- [77] P. Meakin, **15**, 97 (1999).
- [78] S. K. Friedlander, *Smoke, Dust and Haze: Fundamentals of Aerosol Dynamics*, Oxford University Press: New York, 2000.
- [79] D. A. McQuarrie, *Statistical Mechanics*, HARPER and ROW, 1976.
- [80] J. xing Yang et al., J. Chem. Phys. **93**, 711 (1990).
- [81] P. J. Steinhardt, D. R. Nelson, and M. Ronchetti, Phys. Rev. B **28**, 784 (1983).
- [82] F. C. Frank, **215**, 43 (1952).
- [83] P. R. ten Wolde, M. J. Ruiz-Montero, and D. Frenkel, J. Chem. Phys. **104**, 9932 (1996).
- [84] A. L. Mackay, Acta Crysta. **15**, 916 (1962).
- [85] W. Lechner and C. Dellago, J. Chem. Phys. **129**, 114707 (2008).
- [86] C. Desgranges and J. Delhommelle, Phys. Rev. B **77**, 054201 (2008).
- [87] P. R. ten Wolde, M. J. Ruiz-Montero, and D. Frenkel, Phys. Rev. B **104**, 93 (1996).
- [88] E. Mendez-Villuendas and R. K. Bowles, Phys. Rev. Lett. **98**, 185503 (2007).
- [89] S. Yanting Wang S. Teitel and C. Dellago, J. Chem. Phys. **122**, 214277 (2005).
- [90] J. A. van Meel et al., J. Chem. Phys. **129**, 204505 (2008).
- [91] W. C. K. Poon and M. D. Haw, Avd. Colloid Interface Sci. **73**, 71 (1997).
- [92] P. Charbonneau, Phys. Rev. E **75**, 011507 (2007).

- [93] A. G. Walton, *The Formation and Properties of Precipitates*, Interscience: New York, 1967.
- [94] F. Family and D. Landau, *Kinetics of Aggregation and Gelation*, North-Holland: Amsterdam, 1984.
- [95] E. Zaccarelli, *J. Phys.: Condens. Matter* **19**, 323101 (2007).
- [96] A. J. Liu and S. R. Nagel, *Nature(London)* **396**, 21 (1998).
- [97] V. Trappe, V. Prasad, L. Cipelletti, P. N. Segre, and D. A. Weitz, *Nature(London)* **411**, 772 (2001).
- [98] E. K. Hobbie, *Phys. Rev. Lett.* **81**, 3996 (1998).
- [99] C. M. Sorensen, H. X. Zhang, and T. W. Taylor, *Phys. Rev. Lett.* **59**, 363 (1987).
- [100] E. H. A. de Hoog, W. K. Kegel, A. van Blaaderen, and H. N. W. Lekkerkerker, *Phys. Rev. E* **64**, 021407 (2001).
- [101] J. R. Savage, D. W. Blair, A. J. Levine, R. A. Guyer, and A. D. Dinsmore, *Science* **314**, 795 (2006).
- [102] P. J. Lu et al., *Nature(London)* **453**, 499 (2008).
- [103] F. Cardinaux, T. Gibaud, A. Stradner, and P. Schurtenberger, *Phys. Rev. Lett.* **99**, 118301 (2007).
- [104] K. Kroy, M. E. Cates, and W. C. K. Poon, *Phys. Rev. Lett.* **92**, 148302 (2004).
- [105] K. G. Soga, J. R. Melrose, and R. C. Ball, *J. Chem. Phys.* **108**, 6026 (1998).
- [106] G. Foffi, C. Michele, F. Sciortino, and Tartagila, *Phys. Rev. Lett.* **94**, 078301 (2005).
- [107] M. G. Noro and D. Frenkel, *J. Chem. Phys.* **113**, 2941 (2000).

- [108] K. Binder and M. H. Kalos, *J. Stat. Phys.* **22**, 363 (1980).
- [109] R. Jullien and R. Botet, *Aggregation and Fractal Aggregates*, World Scientific, Singapore, 1987.
- [110] J. R. Melrose, *Europhys. Lett.* **19**, 51 (1992).
- [111] N. Arakus, *Theoretical Approaches to Self-Assembly and Biology*, PhD thesis, Applied Mathematics, Harvard University, Cambridge, Massachusetts, 2009.
- [112] N. Arkus, V. N. Manoharam, and M. P. Brenner, *Phys. Rev. Lett.* **103**, 118303 (2009).
- [113] G. Meng, N. Arkus, M. P. Brenner, and V. N. Manoharam, *Science* **327**, 560 (2010).
- [114] L. M. Felicov, *Group Theory and Its Physical Applications*, The University of Chicago Press, 1966.
- [115] J. C. Cole, *Acta Crysta.* **B57**, 88 (2001).
- [116] V. Manoharan, M. T. Elsesser, and D. J. Pine, *Science* **301**, 483 (2003).
- [117] M. R. Haore, *Adv. Chem. Phys* **40**, 49 (2007).
- [118] O. Glatter and O. Kratky, *Small Angle X-ray Scattering*, Academic, London, 1982.
- [119] S. K. Friedlander, *Smoke, Dust and Haze: Fundamentals of Aerosol Behavior*, Wiley, New York, 1977.
- [120] D. Fry, T. Sintes, A. Chakrabarti, and C. M. Sorensen, *Phys. Rev. Lett.* **89**, 148301 (2002).
- [121] F. Pierce, C. M. Sorensen, and A. Chakrabarti, *Phys. Rev. E* **74**, 021411 (2006).
- [122] P. J. Flory, *Principles of Polymer Chemistry*, Cornell University Press, 1953.

Appendix A

Free Energy of Mixing in the Interpenetration Regime

The total free energy, mentioned in chapter 2, can be written as

$$\Delta G^T = \Delta G^M + \Delta G^{el} \quad (\text{A.1})$$

where ΔG^M is the free energy of mixing of the polymer segments and ΔG^{el} represents the elastic contribution to the free energy. We will now focus on the derivation of the ΔG^M .

Using the Flory-Huggins Theory, the change in free energy of mixing by bringing two polymer segments a and b , a distance d apart, is given by (see ch.12 of [122] for details):

$$\delta(\Delta G^M) = \frac{kT dV}{V_l} [\ln(1 - (\rho_a + \rho_b)V_s) + \chi V_s (\rho_a + \rho_b)] (1 - (\rho_a + \rho_b)V_s) \quad (\text{A.2})$$

By expanding the logarithmic term in above eqn. A.2 and simplifying, one can obtain the following expression

$$\delta(\Delta G^M) = 2kT(1/2 - \chi)\rho_a\rho_b(V_s^2/V_l)\delta v \quad (\text{A.3})$$

where χ is the flory chi parameter for the solvent-polymer interaction, ρ_a and ρ_b are the density distribution functions of the polymer segments in the respective elements when the polymers are far apart from each other, V_s is the volume of the segment and V_l is the solvent molecular volume. The total free energy change can be obtained by integrating above equation A.3 over the whole volume as:

$$\Delta G^M = 2kT(1/2 - \chi)(V_s^2/V_l) \int \rho_a\rho_b\delta V \quad (\text{A.4})$$

To estimate the free energy of mixing between the ligands on the surface of two spheres, we first derive the expression for the case of two parallel plates and then, by using the Deryagin Approximation (*seeIsraelvilliebook*), we can extend our results for case of two identical spheres. For the case of parallel plates, considering that the total number of polymer segments normal to the surface are n , separated by a distance d , the free energy of mixing is given by

$$\Delta G^M = 2kT(1/2 - \chi)n^2(V_s^2/V_l) \int_{d-L}^L \rho_a \rho_b dx \quad (\text{A.5})$$

where L is the length of the ligands, d is the separation between the plates and n is the total number of ligand segments in the volume normal (in the x-direction) to the unit surface. Assuming the constant density distribution of the ligand segments (*i.e.* $\rho_a = \rho_b = 1/L$), the above expression is given by

$$\Delta G^M = 2kT(1/2 - \chi)n^2(V_s^2/V_l) \frac{2}{L}(1 - d/2L) \quad (\text{A.6})$$

This assumption of constant density of the ligands is valid for the regime where the ligands are not significantly compressed. In literature (*give references of the papers*), this regime is termed as the interpenetration regime. Now, using the Deryaguin Approximation $\Delta G^M \sim \pi d \int_{d_0}^{\infty} (\Delta G^M) dd$, we can write the free energy of mixing for the case of two identical spheres as

$$V_2(r) = \pi kT(1/2 - \chi)N_A \omega^2 (v_2^2/V_l) 2d(1 - d_0/2L)^2 \quad (\text{A.7})$$

where ω is the weight of the ligands per unit surface area and v_2 is the partial specific volume of the ligands. We have also used $V_2(r)$ as the potential energy to keep our notation consistent with the equations in chapter 2. In our case, we can write $\frac{N_A}{V_l} = \frac{1}{v_m}$ where v_m is the volume of one solvent molecule (Toluene in our case). For Toluene, $v_m = \frac{107 \text{ cm}^3}{N_A} = 1.78 \times 10^{-28}$. Also, we can replace ωv_2 by $\phi_{av} L$ where $\phi_{av} = \frac{N V_{ligand}}{V_{shell}}$ is the average volume fraction of the ligands in the tethered layers. In our rescaled units, $\tilde{L} = L/d$, $x = r/d$ and $\tilde{h} = h/d$ where L is the ligand contour length, h is the surface-surface distance of

the nanoparticles and r is the center-center distance of the nanoparticles. Hence, for the interpenetration regime (*i.e.* $1 + \tilde{L} < x < 1 + 2\tilde{L}$), above eqn. [A.7](#) is given by

$$V_2(r) = \frac{\pi d}{v_m} \phi_{av}^2 \left(\frac{1}{2} - \chi\right) L^2 2 \left(1 - \frac{h}{2L}\right)^2$$

or

$$V_2(r) = \frac{\pi d}{v_m} \phi_{av}^2 \left(\frac{1}{2} - \chi\right) \frac{1}{2} (2L - h)^2 \quad (\text{A.8})$$

or in rescaled lengths,

$$V_2(x) = \frac{\pi d^3}{2v_m} \phi_{av}^2 \left(\frac{1}{2} - \chi\right) [x - (1 + 2\tilde{L})]^2 \quad (\text{A.9})$$

The above derivation in equation [A.9](#) is done for the interpenetration regime.

Appendix B

Free Energy of Mixing in Interpenetration and Compression Regime

For the case where ligands from opposite surfaces are compressed against each other (i.e. when $d \leq L$), the regime is known as *interpenetration and compression* regime in literature give reference. The main assumption, in this regime, is the fact that the segment density function is related to the separation between the ligands as compared to the ligand length i.e. $\rho_a = \rho_b = 1/d$. Interpenetration effects are the same in this regime as mentioned in [A](#) whereas the compression term is due to the fact that in this regime, ligands not only self-interpenetrate but there is also an elastic compression between the ligands. Thus, for the case of parallel plates, the mixing term in this regime is given by,

$$\Delta G^M = 2kT(1/2 - \chi)(V_s^2/V_l) \left[\int_0^d \rho_a \rho_b dx + \int_0^d \rho_a^2 dx - \int_0^\infty \rho_a^2 dx \right] \quad (\text{B.1})$$

For the case of spherical particles, we apply Deryaguin Approximation to the above equation. By solving above equation for the case of spherical particles, in the rescaled lengths, the resultant equation is given as

$$V_3(r) = \frac{\pi d}{v_m} \phi_{av}^2 \left(\frac{1}{2} - \chi \right) L^2 3 \ln \left(\frac{L}{h} \right) + 2 \frac{h}{L} - \frac{3}{2} \quad (\text{B.2})$$

or in the rescaled form,

$$V_3(x) = \frac{\pi d^3}{v_m} \phi_{av}^2 \left(\frac{1}{2} - \chi \right) \tilde{L}^2 3 \ln \left(\frac{\tilde{L}}{x-1} \right) + 2 \frac{x-1}{\tilde{L}} - \frac{3}{2} \quad (\text{B.3})$$

The formalism for the elastic contributions is based on the description by *Flory* (see reference [122] for details). According to Flory, the elastic contributions arise due to the change in the configurational microstates of the ligands as they transform from an uncompressed state to a compressed state. The change can be represented by the following relation;

$$\Delta G = -2kT \sum_j \nu_j \ln \delta \rho(a_j) / \rho(a_j / \delta) \quad (\text{B.4})$$

where $\rho(x)$ is the segment density distribution, ν is the total number of chains per unit area and δ is the ratio of the ligands length before and after compression. Considering the constant segment model, we can set $\rho = 1/L$ such that for the case of flat plate

$$\Delta G = -2kT\nu \ln \delta \quad (\text{B.5})$$

For the case of spherical particles, using Deryaguin Approximation,

$$V_4(r) = \pi \frac{d}{2} \int_{\delta_0}^{\delta_\infty} \Delta G \quad (\text{B.6})$$

where $\delta_0 = \frac{h}{L}$. Solving above equation, we get

$$V_4(r) = d\pi\nu h \left(\ln\left(\frac{h}{L}\right) - 1 \right) + L \quad (\text{B.7})$$

$$= d\pi\nu h \left(\ln(\delta_0) - 1 \right) + L \quad (\text{B.8})$$

or in the rescaled form

$$\begin{aligned} V_4(x) &= \frac{1}{2} d^2 \pi \nu \tilde{L} \left(\frac{h}{L} - 1 \right)^2 \\ &= \frac{1}{2} d^2 \pi \nu \tilde{L} \left(\frac{r-d}{L} - 1 \right)^2 \\ &= \frac{1}{2} d^2 \pi \nu \tilde{L} \left(\frac{x-1}{\tilde{L}} - 1 \right)^2 \\ &= \frac{1}{2} \frac{d^2}{\tilde{L}} \pi \nu (x-1-\tilde{L})^2 \\ &= \frac{1}{2} \frac{d^2 \pi \nu}{\tilde{L}} (x - (1 + \tilde{L}))^2 \end{aligned} \quad (\text{B.9})$$

Appendix C

Parameters of Brownian Dynamics Algorithm

The parameters in the equation 3.23 are given by

$$\sigma_1^2 \equiv \langle \mathcal{X}^2(\Delta t) \rangle = \frac{k_B T_{ref}}{m} A(\gamma \Delta t) \quad (\text{C.1})$$

$$\sigma_2^2 \equiv \langle \mathcal{Y}^2(\Delta t) \rangle = \frac{k_B T_{ref}}{m} (\Delta t)^2 B(\gamma \Delta t) \quad (\text{C.2})$$

and

$$r_{12} \sigma_1 \sigma_2 \equiv \langle \mathcal{X}(\Delta t) \mathcal{Y}(\Delta t) \rangle = \frac{k_B T_{ref}}{m} (\Delta t) C(\gamma \Delta t) \quad (\text{C.3})$$

where

$$A(y) \equiv 1 - \exp[-2y] \quad (\text{C.4})$$

$$B(y) \equiv y^{-2}(2y - 3 + 4 \exp[-y] - \exp[-2y]) \quad (\text{C.5})$$

$$C(y) \equiv y^{-1}(1 - \exp[-y])^2 \quad (\text{C.6})$$

In eqns. 3.19 and 3.20, we also defined some useful functions

$$c_0(y) \equiv \exp[-y] \quad (\text{C.7})$$

$$c_1(y) \equiv y^{-1}(1 - \exp[-y]) \quad (\text{C.8})$$

$$c_2(y) \equiv y^{-1}(y^{-1}(1 - \exp[-y])) \quad (\text{C.9})$$

$$c_3(y) \equiv y^{-1}\left(\frac{1}{2} - y^{-1}(1 - y^{-1}(1 - \exp[-y]))\right) \quad (\text{C.10})$$

where we have used $y \equiv \gamma\Delta t$. For small values of y , we can use the power series expansion given by

$$\begin{aligned} c_0(y) = & 1 - y + \frac{1}{2}y^2 - \frac{1}{6}y^3 + \frac{1}{24}y^4 - \frac{1}{120}y^5 + \frac{1}{720}y^6 \\ & - \frac{1}{5040}y^7 + \frac{1}{40320}y^8 \end{aligned} \quad (\text{C.11})$$

$$\begin{aligned} c_1(y) = & 1 - \frac{1}{2}y + \frac{1}{6}y^2 - \frac{1}{24}y^3 + \frac{1}{120}y^4 - \frac{1}{720}y^5 + \frac{1}{5040}y^6 \\ & - \frac{1}{40320}y^7 + \frac{1}{362880}y^8 \end{aligned} \quad (\text{C.12})$$

$$\begin{aligned} c_2(y) = & \frac{1}{2} - \frac{1}{6}y + \frac{1}{24}y^2 - \frac{1}{120}y^3 + \frac{1}{720}y^4 - \frac{1}{5040}y^5 + \frac{1}{40320}y^6 \\ & - \frac{1}{362880}y^7 + \frac{1}{3628800}y^8 \end{aligned} \quad (\text{C.13})$$

$$\begin{aligned} c_3(y) = & \frac{1}{6} - \frac{1}{24}y + \frac{1}{120}y^2 - \frac{1}{720}y^3 + \frac{1}{5040}y^4 - \frac{1}{40320}y^5 + \frac{1}{362880}y^6 \\ & - \frac{1}{3628800}y^7 + \frac{1}{39916800}y^8 \end{aligned} \quad (\text{C.14})$$

and

$$\begin{aligned} \sigma_1 = & \left[\frac{k_B T_{ref}}{m} (2y - 2y^2 + \frac{8}{6}y^3 - \frac{16}{24}y^4 + \frac{32}{120}y^5 - \frac{64}{720}y^6 + \frac{128}{5040}y^7 \right. \\ & \left. - \frac{256}{40320}y^8) \right]^{1/2} \end{aligned} \quad (\text{C.15})$$

$$\begin{aligned} \sigma_2 = & \left[\frac{k_B T_{ref}}{m} (\Delta t)^2 \left(\frac{4}{6}y - \frac{1}{2}y^2 + \frac{28}{120}y^3 - \frac{60}{720}y^4 + \frac{124}{5040}y^5 - \frac{252}{404320}y^6 \right. \right. \\ & \left. \left. + \frac{508}{362880}y^7 - \frac{1020}{362880}y^8 \right) \right]^{1/2} \end{aligned} \quad (\text{C.16})$$

and r_{12} can be obtained by using eqs. C.15, C.16 and C.6 into eq. C.3. Using above

mentioned function values, we can rewrite eqs. 3.19 and 3.20 as

$$\begin{aligned} v(t_n + \Delta t) &= v(t_n)c_0(\gamma\Delta t) + (m)^{-1}F(t_n)c_1(\gamma\Delta t) \\ &\quad + (m)^{-1}\dot{F}(t_n)(\Delta t)^2c_2(\gamma\Delta t) + \mathcal{X}(\Delta t) + O[(\Delta t)^3] \end{aligned} \quad (\text{C.17})$$

$$\begin{aligned} x(t_n + \Delta t) &= x(t_n) + v(t_n)(\Delta t)c_1(\gamma\Delta t) + (m)^{-1}F(t_n)(\Delta t)^2c_2(\gamma\Delta t) \\ &\quad + (m)^{-1}\dot{F}(t_n)(\Delta t)^3c_3(\gamma\Delta t) + \mathcal{Y}(\Delta t) + O[(\Delta t)^4] \end{aligned} \quad (\text{C.18})$$

Also, we can see that when $\gamma \rightarrow 0$ then $\gamma\Delta t \rightarrow 0$ which means that $c_0(0) = 1, c_1(0) = 1, c_2(0) = 1/2, c_3(0) = 1/6, \sigma_1 = 0, \sigma_2 = 0$ and $r_{12} = \sqrt{(3/4)}$ and above eqs. C.17 and C.18 can be reduced to

$$v(t_n + \Delta t) = v(t_n) + (m)^{-1}F(t_n)(\Delta t) + (2m)^{-1}\dot{F}(t_n)(\Delta t)^2 + O[(\Delta t)^3] \quad (\text{C.19})$$

$$\begin{aligned} x(t_n + \Delta t) &= x(t_n) + v(t_n)(\Delta t) + (2m)^{-1}F(t_n)(\Delta t)^2 + (6m)^{-1}\dot{F}(t_n)(\Delta t)^3 \\ &\quad + O[(\Delta t)^4] \end{aligned} \quad (\text{C.20})$$

which are the *Verlet algorithm*.